

Electronic Thesis and Dissertation Repository

12-11-2012 12:00 AM

Development of a Compact Piezoworm Actuator For Mr Guided Medical Procedures

Khaled El Bannan
The University of Western Ontario

Supervisor
Shaun Salisbury
The University of Western Ontario

Graduate Program in Mechanical and Materials Engineering
A thesis submitted in partial fulfillment of the requirements for the degree in Doctor of Philosophy
© Khaled El Bannan 2012

Follow this and additional works at: <https://ir.lib.uwo.ca/etd>



Part of the [Electro-Mechanical Systems Commons](#)

Recommended Citation

El Bannan, Khaled, "Development of a Compact Piezoworm Actuator For Mr Guided Medical Procedures" (2012). *Electronic Thesis and Dissertation Repository*. 974.
<https://ir.lib.uwo.ca/etd/974>

This Dissertation/Thesis is brought to you for free and open access by Scholarship@Western. It has been accepted for inclusion in Electronic Thesis and Dissertation Repository by an authorized administrator of Scholarship@Western. For more information, please contact wlsadmin@uwo.ca.

**DEVELOPMENT OF A COMPACT PIEZOWORM ACTUATOR FOR MR
GUIDED MEDICAL PROCEDURES**

(Spine title: A compact MRI compatible Piezoworm Actuator)
(Thesis format: Monograph)

By

Khaled Mohamed El Bannan

Graduate Program in Mechanical Engineering

A thesis submitted in partial fulfillment
of the requirements for the degree of
Doctor of Philosophy

The School of Graduate and Postdoctoral Studies
The University of Western Ontario
London, Ontario, Canada

© Khaled Mohamed El Bannan 2012

THE UNIVERSITY OF WESTERN ONTARIO
School of Graduate and Postdoctoral Studies
CERTIFICATE OF EXAMINATION

Supervisor

Examiners

Dr. Shaun P. Salisbury

Dr. Sam F. Asokanthan

Supervisory Committee

Dr. Ralph O. Buchal

Dr. George K. Knopf

Dr. Ken McIsaac

Dr. Michael D. Naish

Dr. Goldie Nejat

The thesis by

Khaled Mohamed El Bannan

entitled:

Development of a Compact Piezoworm Actuator for MR-Guided Medical Procedures

is accepted in partial fulfillment of the
requirements for the degree of
Doctor of Philosophy

Date

Chair of the Thesis Examination Board

Abstract

In this research, a novel piezoelectric actuator was developed to operate safely deep inside the magnetic resonance imaging (MRI) machine bore. It is based on novel design that generates linear and rotary motion simultaneously for higher needle insertion accuracy in medical procedures. This degree of freedom (DOF) flexibility for needle insertion results in decreasing the recovery time and improves the overall health of the patient. The piezoelectric actuation method was proposed for the developed actuator based on the piezoworm concept which minimizes the actuator size, maximizes the output force, and enhances micrometer scale positioning accuracy. MRI guidance can be used to guide this actuator as MRI machines are used widely in hospitals and produces high quality images for soft tissue. Moreover, MRI-guided intervention is one of the emerging biomedical engineering areas of development, so this research was developed to aid in the selection of suitable materials to construct actuators that can be used in this challenging environment. Usually only nonmagnetic materials are used in this extremely high magnetic environment. These materials are classified as MRI compatible materials and are selected to avoid hazardous conditions and image quality degradation. But unfortunately many inert materials to the magnetic field do not possess desirable mechanical properties in terms of hardness, stiffness and strength and much of the available data for MRI compatible materials are scattered throughout the literature and often too device specific. Furthermore, the fact that significant heating is experienced by some of these devices due to the scanner's variable magnetic fields makes it difficult to draw general conclusions to support the choice of suitable material and typically these choices are based on a trial-and-error with extensive time required for prototype development and MRI testing of such devices.

This research provides a quantitative comparison of several engineering materials in the MRI environment and comparison to theoretical behavior which should aid designers/engineers to estimate the MRI compatible material performance before the expensive step of construction and testing. This work focuses specifically on the effects in

the MRI due to the material susceptibility, namely forces, torques, image artifacts and induced heating.

Keywords

MR-compatible actuator, Piezoworm Motor, Complementary Clamps, Compact Design, needle insertion, MR safety, gradient switching, piezoelectric.

Co-Authorship Statement

Chapter 2: Mr. Khaled El Bannan was the principal author of this chapter. A version of this chapter has been accepted for publication in IEEE/ASME Transactions on Mechatronics. Dr. Blaine Chronik, Dr. William Handler, and Chris Wyenberg offered the facilities and participated in the image distortion testing.

Chapter 3: Mr. Khaled El Bannan was the principal author of this chapter. A version of this chapter has been accepted for publication in Journal of Magnetic Resonance (JMR). Dr. Blaine Chronik and Dr. William Handler offered the facilities and participated in the gradient heating testing. Matlab programming was done by Dr. William Handler.

Acknowledgements

First, I praise God the almighty for bestowing his mercy on me and giving me the ability to proceed successfully with this endeavor. This thesis as it stands today is a result of collective collaboration, assistance and guidance from several people that owed an acknowledgment.

My first debt of gratitude must go to my advisor, Prof. Shaun Salisbury. He always provided encouragement and effective technical guidance. I could turn to him for sound advice and discussions at any time; he was never lethargic, or unprepared, but mostly enthusiastic, and willing to help which made the research environment highly fruitful and enjoyable. He was a strong and supportive adviser to me throughout my graduate school career, but always given me great freedom to pursue my work independently.

I am indebted to Prof. Blaine Chronik, Dr. William Handler, and Chris Wyenberg for their collaboration in the MR-compatibility tests, their vision, their support, guidance and helpful suggestions especially Dr. William help with Matlab. I am also grateful to Clayton Cook, Dan Sweiger, and UMS members for their good work in building the prototype.

MME Engineering Laboratory colleagues also deserve my sincere thanks and respect for providing a stimulating and fun studying environment. I would like to acknowledge the assistance and help of the Mechanical Engineering department administrative staff through the academic years.

Ultimately, I would like to thank my Family Rasha, Nadia, Ahmed and Mostafa for their endless patience, great support, unmatched understanding and encouragement through the whole processes especially during the thesis writing.

Table of Contents

| | |
|--|-----|
| CERTIFICATE OF EXAMINATION | ii |
| Abstract | iii |
| Co-Authorship Statement..... | v |
| Acknowledgements..... | vi |
| Table of Contents | vii |
| List of Tables | xi |
| List of Figures | xii |
| List of Symbols, Abbreviations and Nomenclature..... | xv |
| Chapter 1 Introduction..... | 1 |
| 1.1 Background | 1 |
| 1.2 MR-compatibility..... | 2 |
| 1.3 Review of the literature..... | 4 |
| 1.3.1 Hydraulic actuation method..... | 5 |
| 1.3.2 Pneumatic actuation method..... | 6 |
| 1.3.3 Ultrasonic piezoelectric actuation method..... | 9 |
| 1.3.4 Manual actuation method..... | 11 |
| 1.3.5 Other actuation methods | 12 |
| 1.3.6 Summary | 12 |
| 1.4 Piezoelectric Actuation method | 13 |
| 1.4.1 Introduction..... | 13 |
| 1.4.2 Piezoelectric actuator | 14 |
| 1.4.3 Piezoworm motors | 15 |
| 1.4.4 Summary | 17 |
| 1.5 Piezoworm Motor Design | 18 |
| 1.5.1 Linear motion Piezoworm Motor Design | 18 |

| | |
|--|-----------|
| 1.5.2 Rotary motion Piezoworm Motor Design..... | 23 |
| 1.5.3 Combined motion Piezoworm Motor Design..... | 26 |
| 1.6 Thesis Outline | 30 |
| 1.7 Thesis Objectives | 31 |
| 1.8 List of Contributions | 31 |
| Chapter 2 Prediction of Force and Image Artifacts in MR environment | 32 |
| 2.1 Introduction..... | 32 |
| 2.2 Background and theory | 34 |
| 2.3 Materials | 39 |
| 2.3.1 Sample characterizations and properties..... | 39 |
| 2.4 Methods..... | 41 |
| 2.4.1 Setup of the experiment | 41 |
| 2.4.2 Samples orientations | 41 |
| 2.4.3 Phantom design..... | 42 |
| 2.4.4 Assessment of magnetic field interaction | 42 |
| 2.4.4.1 Translation forces induced in the samples..... | 42 |
| 2.4.4.2 Torque induced in the samples | 43 |
| 2.4.5 Assessment of the image artifacts..... | 43 |
| 2.4.5.1 Imaging protocols parameters..... | 44 |
| 2.4.5.1 Assessment of signal dropout | 44 |
| 2.4.5.2 Assessment of image distortion | 45 |
| 2.4.6 Assessment of susceptibility related to force..... | 45 |
| 2.5 Results..... | 46 |
| 2.5.1 Translation force and torque in magnetic field..... | 46 |
| 2.5.2 Image Distortion | 47 |
| 2.5.2.1 Signal dropout from the GE sequence | 47 |
| 2.5.2.2 Image distortion from the TSE sequence..... | 50 |
| 2.6 Discussion | 53 |
| 2.7 Conclusions..... | 58 |

| | | |
|------------------|--|----|
| Chapter 3 | Induced heat in MR environment Concepts | 59 |
| 3.1 | Introduction..... | 59 |
| 3.2 | Background and theory | 60 |
| 3.2.1 | Radio frequency heating | 60 |
| 3.2.2 | Gradient heating..... | 60 |
| 3.3 | Materials and methods | 64 |
| 3.3.1 | Phantom design..... | 64 |
| 3.3.2 | Radio frequency heating | 64 |
| 3.3.2.1 | Setup of the experiment | 64 |
| 3.3.2.2 | Samples orientations | 65 |
| 3.3.2.3 | RF heating sample positioning and orientation | 65 |
| 3.3.2.4 | Thermometry system for RF heating experiments..... | 66 |
| 3.3.2.5 | RF heating protocol and sequences..... | 67 |
| 3.3.3 | Gradient heating..... | 68 |
| 3.3.3.1 | Experimental setup and test materials..... | 68 |
| 3.3.3.2 | Gradient heating protocol parameters | 69 |
| 3.3.3.3 | Thermometry system and probes placement..... | 69 |
| 3.4 | Results..... | 70 |
| 3.4.1 | Radio frequency heating | 70 |
| 3.4.2 | Gradient heating..... | 74 |
| 3.5 | Discussion | 72 |
| 3.6 | Summary | 77 |
| Chapter 4 | Design of two degree of freedom MR-compatible actuator | 79 |
| 4.1 | Introduction..... | 79 |
| 4.2 | Principle of motion | 80 |
| 4.2.1 | Principle of Linear motion..... | 80 |
| 4.2.2 | Principle of rotary motion..... | 82 |
| 4.3 | Actuator design | 85 |

| | |
|--|-----|
| 4.3.1 Extension frame design..... | 86 |
| 4.3.2 Rotation frame design..... | 88 |
| 4.3.3 Clamp Design..... | 88 |
| 4.4 Theoretical torque and force | 90 |
| 4.5 Summary and conclusions | 92 |
| Chapter 5 MR-Compatibility and Performance tests | 93 |
| 5.1 Introduction..... | 93 |
| 5.2 Manufacturing of Prototype..... | 94 |
| 5.3 Assessment of Flexures Components | 96 |
| 5.4 Linear and Rotary Performance Tests & Results..... | 99 |
| 5.4.1 Experimental Setup..... | 100 |
| 5.4.2 Static Performance | 102 |
| 5.4.3 Dynamic Performance | 103 |
| 5.4.3.1 Linear Dynamic Performance | 103 |
| 5.4.3.2 Rotary Dynamic Performance..... | 104 |
| 5.4.3.3 Combined Linear & Rotary Dynamic Performance | 104 |
| 5.5 MR-Compatibility Tests & Results | 110 |
| 5.5.1 Experimental Setup..... | 110 |
| 5.6 Results and Discussion | 110 |
| 5.7 Summary & Conclusion..... | 111 |
| Chapter 6 Summary and Future Work | 114 |
| 6.1 Summary | 114 |
| 6.2 Future Work..... | 117 |
| References | 119 |
| Appendix A: Drawings of Piezoworm MR-Compatible Actuator | 128 |
| Curriculum Vitae | 140 |

List of Tables

| | |
|---|-----|
| Table 2.1 Unified Numbering System for Metals designation | 40 |
| Table 2.2 Properties of interest for the test samples | 41 |
| Table 2.3 Pulse sequence parameters for image distortion used in the experiment | 44 |
| Table 2.4 Values of measured deflection angle and respective calculated force..... | 47 |
| Table 2.5 Signal dropout of different materials for different GRE sequence | 49 |
| Table 2.6 Image distortion values of different materials for different TSE sequence | 51 |
| Table 2.7 Experimental and calculated sample forces..... | 52 |
| Table 2.8 Experimental image artifacts in view plane..... | 53 |
| Table 2.9 Calculated image artifacts in view plane | 54 |
| Table 3.1 Material Properties..... | 71 |
| Table 3.2 Measured Temperature Rise | 78 |
| Table 5.1 Mechanical, Electrical and Magnetic properties of C17510 [TH04]..... | 96 |
| Table 5.2 Mechanical, Electrical and Magnetic properties of Brass C3600..... | 97 |
| Table 5.3 Experimental theoretical force and torque values..... | 102 |
| Table 5.4 Scan Sequences..... | 111 |
| Table 5.5 Tests with G1 Sequence..... | 112 |
| Table 5.6 Tests with T1 and T2 Sequences | 113 |

List of Figures

| | |
|--|----|
| Fig.1.1 Dimension of the Scanner [7, 14]..... | 3 |
| Fig.1.2 MR-compatible surgical robot [16] | 5 |
| Fig.1.3 MR-compatible actuator concept with hydrostatic transmission [18]..... | 6 |
| Fig.1.4 The pneumatic system (PneuStep) [19, 21]..... | 7 |
| Fig.1.5 Pneumatic positioner with turbine, rotor and gear box [22]..... | 8 |
| Fig.1.6 MR-compatible pneumatic limb positioner [23] | 8 |
| Fig.1.7 Ultrasonic motor and principle of the propagating wave [27, 28]..... | 9 |
| Fig.1.8 MR-compatible prostate biopsy manipulator [29]..... | 10 |
| Fig.1.9 Three DOF MR-compatible prostate biopsy manipulator [30] | 10 |
| Fig.1.10 MR-compatible manual actuation mechanism [31]..... | 11 |
| Fig.1.11 Structure of a piezoelectric stack[42] | 15 |
| Fig.1.12 Piezoelectric stacks from Physik Instrumente [43] | 16 |
| Fig.1.13 Operation principal of piezoworm and sequential stepping | 17 |
| Fig.1.14 Hsu “Hybrid” piezoworm design [49]..... | 19 |
| Fig.1.15 Locher “Hybrid” piezoworm mechanism [50] | 19 |
| Fig.1.16 Brisbane “Walker” piezoworm design [51]..... | 20 |
| Fig.1.17 Burleigh Inchworm® design [53]..... | 21 |
| Fig.1.18 Zhang & Zhu piezoworm design [44] | 21 |
| Fig.1.19 Piezoworm disc motors [61, 62]..... | 24 |
| Fig.1.20 Piezoworm drum motor [63, 64] | 24 |
| Fig.1.21 Piezoworm shaft motors [65, 66] | 25 |
| Fig.1.22 Piezoworm shaft motors actuated by belts [67] | 25 |
| Fig.1.23 Staufenberg design of linear and rotary piezoworm [68]..... | 27 |
| Fig.1.24 RLPA linear and rotary actuator [70]..... | 28 |
| Fig.1.25 MR-compatible 2 DOF actuator [72] | 28 |
| Fig.2.1 Theoretical distortion region | 40 |
| Fig.2.2 Image distortion experiment setup | 42 |

| | |
|--|----|
| Fig.2.3 Experiment sample and fixture used | 43 |
| Fig.2.4 Deflection angle for magnetic induced force experiments | 46 |
| Fig.2.5 Signal dropout for Stainless Steel 20 in a GRE sequence | 48 |
| Fig.2.6 Signal dropout for Titanium in a GRE sequence..... | 48 |
| Fig.2.7 Perimeter extraction for the signal dropout area of stainless steel 20 | 49 |
| Fig.2.8 Signal dropout for Stainless Steel 20 in a TSE sequence | 50 |
| Fig.2.9 Signal dropout for Titanium in a TSE sequence..... | 50 |
| Fig.2.10 Distortion for Inconel and the line tracing algorithm | 51 |
| Fig.2.11 Experimental and calculated force versus susceptibility | 55 |
| Fig.2.12 Experimental artifact radius versus susceptibility | 56 |
| Fig.2.13 Calculated artifact radius versus susceptibility | 57 |
| Fig.3.1 Scaling factor for a rectangle slab of finite width | 63 |
| Fig.3.2 Scaling factor for cylinder of infinite length | 65 |
| Fig.3.3 Setup configuration for the RF heating experiment and samples used | 66 |
| Fig.3.4 Positioning of the temperature sensing probes for RF experiment | 67 |
| Fig.3.5 Gradient heating experiment setup..... | 69 |
| Fig.3.6 2D FEA model with parallel magnetic field..... | 73 |
| Fig.3.7 2D finite FEA model with parallel magnetic field | 73 |
| Fig.3.8 2D FEA model with perpendicular magnetic field..... | 74 |
| Fig.3.9 3D finite FEA model with perpendicular magnetic field | 74 |
| Fig.3.10 Scale factor for parallel and perpendicular field orientation | 75 |
| Fig.3.11 Experimental heating profile for Aluminum and Inconel | 76 |
| Fig.3.12 Experimental, FEA and theoretical temperature changes comparison..... | 77 |
| Fig.4.1 CAD model and photo of the prototype | 81 |
| Fig.4.2 Linear and rotary stepping sequences..... | 83 |
| Fig.4.3 Exploded view and components of the actuator | 84 |
| Fig.4.4 NC clamps positions..... | 85 |
| Fig.4.5 NU clamps positions..... | 85 |
| Fig.4.6 Extension frame | 87 |

| | |
|--|-----|
| Fig.4.7 Rotational frame | 89 |
| Fig.5.1 Fine adjustment of misalignment using set screw & flexure..... | 95 |
| Fig.5.2 Clearance between the actuator components..... | 95 |
| Fig.5.3 Fine adjustment of the component misalignment using set screw | 96 |
| Fig.5.4 Picture of the fabricated prototype | 98 |
| Fig.5.5a Step response of the prototype at 1 Hz | 99 |
| Fig.5.5b Step response of the prototype at 800 Hz | 100 |
| Fig.5.6 Experimental Setup for testing the force and torque capacity..... | 101 |
| Fig.5.7 Experimental setup for testing linear or rotary motion..... | 105 |
| Fig.5.8 Forward no load speed vs. Frequency graph (theoretical vs. exp.) | 106 |
| Fig.5.9 Forward no load speed vs. Frequency graph (avg.)..... | 106 |
| Fig.5.10 Reverse no load speed vs. Frequency graph (theoretical vs. exp.)..... | 107 |
| Fig.5.11 Reverse no load speed vs. Frequency graph (avg.) | 107 |
| Fig.5.12 Speed vs. load at frequency 600 Hz | 108 |
| Fig.5.13 No load rotary speed vs. frequency (theoretical vs. exp.) | 108 |
| Fig.5.14 No load rotary speed vs. frequency (theoretical vs. avg.) | 109 |
| Fig.5.15 Speed vs. torque at frequency 600 Hz. (theoretical vs. avg.) | 109 |

List of Symbols, Abbreviations and Nomenclature

| Symbol | Definition |
|---------------------------|---|
| μ | magnetic permeability |
| χ | magnetic susceptibility |
| F | magnetic induced force |
| B_o | magnetic field |
| $\partial B_o/\partial z$ | magnetic field gradient |
| V | volume |
| μ_o | magnetic permeability in free space |
| B_z | disturbance in the static magnetic field |
| a | radius of the sample |
| Δ_z | distortion |
| γ | gyro-magnetic ratio |
| FOV | field of view |
| BW | band width of the receiver |
| \mathbf{m} | dipole moment |
| M | magnetization |
| U | magnetic potential energy |
| θ | angle between dipole moment and magnetic field |
| T | magnetical induced torque |
| D_a | demagnetizing factor along the axis of symmetry |
| D_r | demagnetizing factor along the equivalent radial axis |
| m | mass of the sample |
| α | angular deflection of string |
| g | acceleration due to gravity |
| δ | skin depth |
| ρ | resistivity |
| f | frequency |

| Symbol | Definition |
|---------------|--|
| P | power deposited per square meter |
| H_0 | field strength |
| p | scaling factor |
| \dot{T} | rate of the temperature change |
| ρ_d | mass density |
| c | specific heat capacity |
| Δ | constrained expansion of the piezostack |
| k_p | piezostack stiffness |
| k_f | flexure stiffness |
| Δ_o | free expansion of the piezostack |
| T_a | torque produced by the actuator |
| r | radius of the shaft |
| μ_f | friction coefficient |
| N | normal load between the stator and the shaft |
| F_a | torque produced by the actuator |
| E | Young's modulus of elasticity |
| w | width of the flexure |
| t | thickness of the flexure |
| L | length of the flexure |
| ν | Poisson's ratio |
| C | shear stress correction factor |
| $v_{L_{av}}$ | average linear speed |
| ω_{av} | average angular speed |

Chapter 1

Introduction

1.1 Background

Biopsy and therapy needles need accurate navigation to reach their intended target especially when the target is in the order of 5mm or less. Interactive needle path planning and real time image guidance can be used to improve the precision. Magnetic Resonance imaging (MRI) is known for high contrast of soft tissues which makes it an excellent choice to guide a needle [1]. A two degree of freedom actuator MR-compatible was developed as an objective for the research to aid precise targeted needle placement. The proposed actuator is capable of micrometer resolution and can perform under MRI guidance.

MRI has become a standard diagnostic tool in hospitals around the world and is increasingly used in performing image-guided intervention (IGI) procedures. The trend of using remotely actuated and controlled devices to assist in the performance of MRI-guided interventions are increasing as the image quality is superior to other modalities [2]. Brachytherapy and biopsy medical procedures can be conducted using MRI-guided interventional technology for accurate navigation of the needle. The main goal for these procedures is to insert the needle with high accuracy resulting in a more effective treatment [3]. The key point of accurate placement is rotating the needle around its own

axis by means of either continuous spinning or pulsation methods [3-6]. This emphasizes the need for a two degree-of-freedom actuator for this type of MRI-guided medical procedures.

Despite all the advantages of MRI, the extreme magnetic fields (up to 7 Tesla), rapidly changing magnetic field gradients (GR), and radiofrequency (RF) pulses used in operating the scanner make it a difficult environment in which to operate conventional actuators [7]. One must consider the induced forces, torques and image distortion caused by the introduction of the device into the MR scanner. Heating of the device may also be a concern. Heating results from the interaction of the device with the RF magnetic field and/or the switching gradient fields which can create eddy currents, induction loops, or resonating RF waves along conductors as discussed in [8-10]. Additionally, the limited space inside MRI machine as shown in Fig.1.1, the scanner bore necessitates a compact actuator and hence the materials employed must be strong and rigid as well being MR-compatible [2, 7, 11, and 12].

Safe design and proper functionality are the ultimate goal for any manufactured device. This is even more challenging when MR-compatible devices are being developed to perform in such harsh environment. Therefore, novel actuation techniques and innovative design strategies should be utilized to overcome the multiple restrictions imposed by the MRI environment in terms of space restrictions and image distortion.

Finally, piezoworm principle was employed in the actuator as it offers micrometer accuracy positioning with centimeter range, in addition to compactness of the configuration which make it ideal for the restricted space inside the bore.

1.2 MR-compatibility

First, MR environment was described in [7, 13] as the area in the vicinity of the scanner which includes the static magnetic field, the rapidly changing gradient fields, and finally the radiofrequency magnetic fields. Furthermore in [7] a clear distinction between MR-safety and MR compatibility was set. It was pointed out that MR-safe device does not add any risk to patient in the MR environment but the image quality cannot be assured.

MR-compatibility was explained in [7, 12]. MR-compatible device has to be first MR-safe, also does not affect the image quality of the MR imaging environment, and in turn the MR environment does not degrade the device performance or cause it to malfunction.

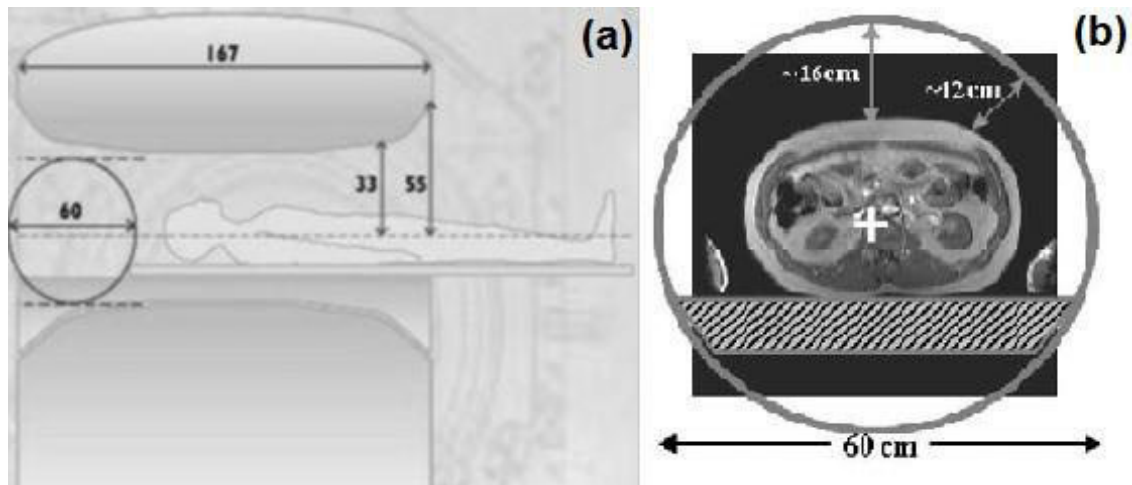


Fig.1.1: (a) Dimensions of a horizontal scanner bore (in centimeters) [7], (b) MR images of a person inside the restricted bore space of an MRI scanner [14]

MR-compatible devices usually consist of several components some of which will be close to the imaging area and others may be completely outside the imaging room. For this reason further classification of compatibility zones has to be defined.

In [7, 12] MR-compatibility zones were divided into 4 zones depending on how close the component (device) to the imaging area during the scanning process. It is stated that if the device is in contact with the imaged part and stays in contact through the whole scan process device is called “Zone 1 compatible device”.

If the component (device) is used inside the bore but not close to the imaged part and if it remains inside or used during the scanning process causing some images distortion the device is called “Zone 2 compatible device”.

If the component (device) is used inside the bore but not close to the imaged part and has to be removed or not used during scanning the device is called “Zone 3 compatible device”.

Finally, if the component (device) is used outside the bore but within the procedure room the device is called “Zone 4 compatible device”.

The proposed device in this research will operate inside the scanner bore and close to the patient imaged part which dictates the highest level of compatibility (Zone 1). The supporting structure connecting the actuator to the scanner can be manufactured from Zone 1 or Zone 2 compatible material with Low magnetic susceptibility [15] as it is away from the imaging area. The amplifier and the control module of the actuator will be placed outside of the procedure room so the issue of zone compatibility does not apply. In the case of control and drive wires between the actuator and the amplifier shielded copper wires are used but it is essential to use filtering techniques to eliminate any radio frequency signals might enter the scanner enclosure through the cables from outside and at least Zone 2 compatibility devices should be used.

In summary, MR-compatibility zone level of components employed in the MR environment depends on how far or close it is from the imaging area. When outside the scanner vicinity commercially available components can be utilized, but when it is in or around the scanner components has to be chosen according to a minimum image distortion criterion. The aim of his research is to realize a (Zone 1) MR-compatible actuator to work deep inside the scanner bore. This can be achieved through selection suitable MR-compatible materials that does not degrade the image quality or endanger patient safety.

1.3 Review of the Literature

The strong magnetic fields existing in the MR environment prevents electromagnetic actuators from being used due to their concept of operation [2]. Other types of actuators were introduced in the literature as alternative methods such as hydraulic, pneumatic, piezoelectric and manual actuation methods. MRI compatible actuation methods like electrostatic actuators, electrostrictive polymer and electrically actuated elastomers were also introduced.

MRI compatible devices are classified in the literature according to their method of actuation or sensor technology as presented in [7], others classified according the medical

procedures they are used in [2]. The focus in this work is to compare between the existing actuation methods based on their advantages and drawbacks to select the optimal method of actuation in the MR environment. The following categorization was considered:

- Hydraulic actuation method
- Pneumatic actuation method
- Ultrasonic piezoelectric actuation method
- Manual actuation method
- Others

1.3.1 Hydraulic Actuation Method

A possible MR-compatible method in the literature is hydraulic actuation method that is magnetically neutral. Hydraulic systems are stiff and can supply high forces and motion needed over relatively long distances. In [16] a six degree of freedom (DOF) manipulator is presented (see Fig.1.2). It performs minimally invasive liver surgery inside open MR scanners as a hybrid system using piezo ultrasonic motors and hydraulic methods combined.

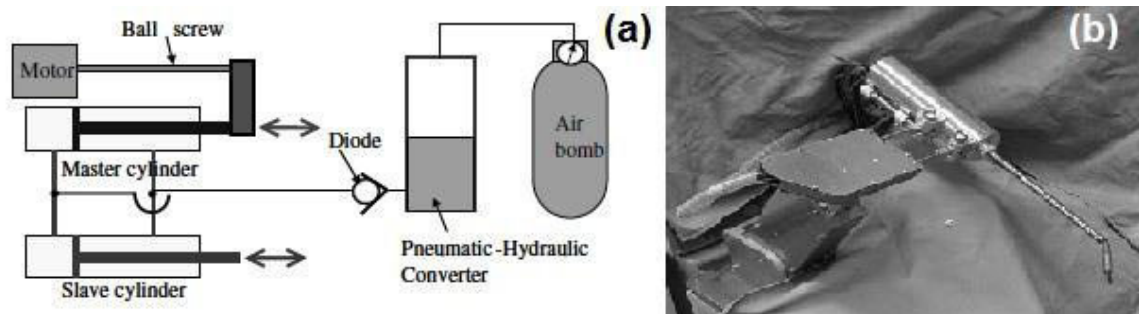


Fig.1.2: (a) Motor-hydraulic system (b) MR-compatible Surgical Robot [16]

The transmission media used in the system is sterilized saline. Fluid leakage was reported as the main problem, but adding leakage compensation mechanism improved controllability and stability for the system. A pure hydraulic configuration using plastic

cylinders on the MRI side is discussed in [17, 18]. The system is a haptic interface with a rotary DOF (degree of freedom) using a master and slave configuration. The master system is a regular hydraulic cylinder driven by an electromagnetic motor. The master system is placed outside the MRI room. The slave is the polymer hydraulic piston coupled with the master by means of hoses (see Fig.1.3). The performance tests showed accuracy of a few micrometers over a range of several centimeters (± 5 cm), with linear speeds up to 30 cm/s and max continuous force of 500 N. The rotary performance shows resolution of 0.14 deg. over operating range of (± 80 deg), maximum continuous torque of 15 N.m, and maximum speed of 200 rpm. The 10 MPa pressure range of the hydraulic circuit was the only performance limiter for the system.

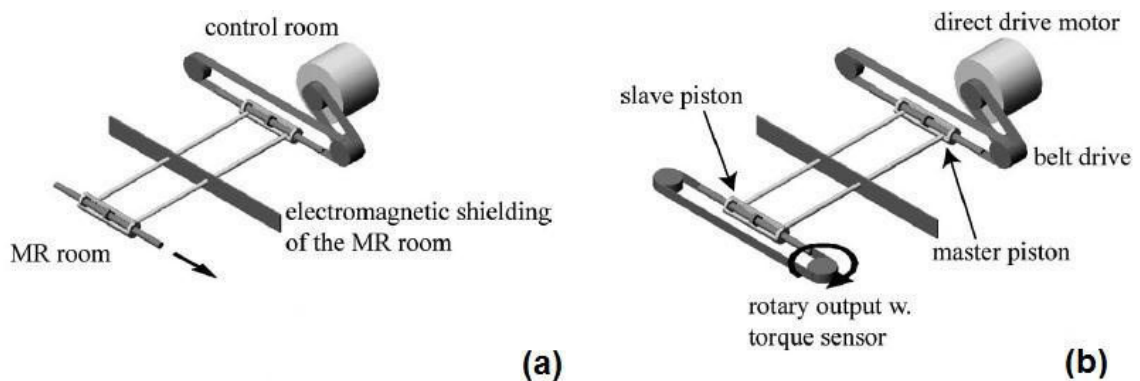


Fig.1.3: MR-compatible (a) linear and (b) rotary actuator concept with hydrostatic transmission [18]

The main concern in this actuation method besides the size is safety issues due to high pressures involved. Furthermore leakage, heavy infrastructure, complexity of control, and performance degradation are other drawbacks of this method.

1.3.2 Pneumatic actuation method

Pneumatic systems are much cleaner hydraulic systems and can produce high speeds. Pneumatic actuation is considered for MR-compatible actuation as presented in [19, 20] for its low cost, low maintenance, compact size and high power to weight ratio. But a

drawback in the pneumatically controlled systems is the reduced precision due to air compressibility. This problem was addressed in [19, 20] by developing the "PneuStep" motor which is based on the idea of a step motor. The device was tested in MR environment up to 7 Tesla without image distortion and achieved motion precision accuracy up to 0.05 mm per step. The device was developed into a fully pneumatic actuated robot. Fig. 1.4a shows MRI-compatible robot configured with six "PneuStep" motors and Fig. 1.4b shows the "PneuStep" motor.



Fig.1.4: (a) The robot with six motors [21] (b) "PneuStep" the air motor [19]

An example is six DOF base on pneumatic actuation is the commercially available MR-compatible InnoMotion™ (Innomedic GmbH, Herxheim, Germany). InnoMotion™ is a robotic arm that assists in interventions inside the MRI scanner and can be used in spinal procedures for pain therapy, tumor therapy, and biopsies [2].

Another device presented in [22] is a novel pneumatic air motor system for limb positioning. It consists of a pneumatic turbine with the output coupled to a gear train. This configuration produces enough power for lifting the targeted body part. The gearbox is constructed from plastic gears, aluminum shafts, and plastic bearings with glass balls. The system is capable of 6 rpm of maximum speed and maximum torque of 0.35 N.m. Fig.1.5 shows the positioning system including the turbine. This device was modified in [23] from 1 DOF to 3 DOF (see Fig.1.6).

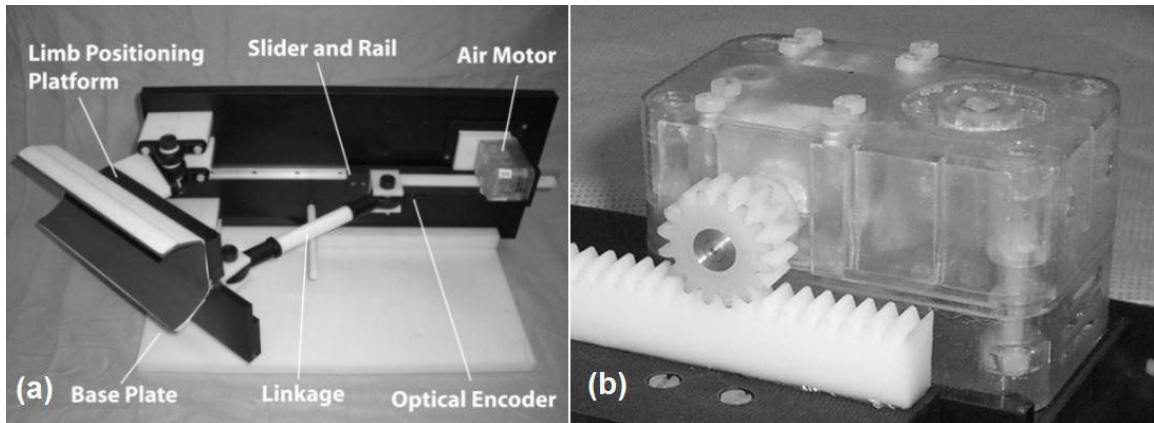


Fig.1.5: (a) Pneumatic positioner (b) turbine, rotor and gear box of the device [22]

The disadvantages of the pneumatic actuation method is the limited stiffness of the system, reduced precision in the controlled motion, compressibility and friction in valves and actuators make the system highly nonlinear, and complicated pneumatic-servo controls. Furthermore, in the literature this type of actuation was mainly used prostate brachytherapy [20] and positioning limbs inside the MRI machine [22, 23].

Space restriction was not an issue for these devices, but the air hoses used for control and actuation of the device could add another burden on smooth maneuverability if the device is used in the restricted space of the scanner bore.

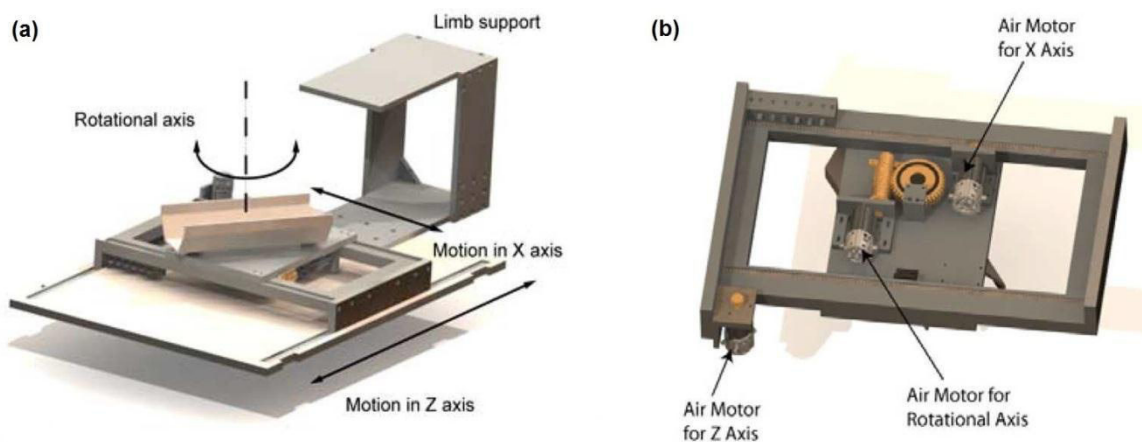


Fig. 1.6: (a) CAD model of system with a limb support. (b) Bottom view of the platform showing the air motors coupled to each axis [23]

1.3.3 Ultrasonic piezoelectric actuation method

Ultrasonic piezoelectric motors technologies are commonly utilized for MR-compatible actuator as presented in [24-26]. Fig.1.7a show the basic components of ultrasonic piezoelectric motor, which consist of a vibrator that is in contact with a rotor and driven by high-frequency power supply. The vibrator is driven by two sinusoidal waves 90 degree out of phase at ultrasonic frequency causing propagation and elliptical motion (Fig. 1.7b) on the surface of the rotor creating the rotary motion. The ultrasonic piezoelectric motors does not generate magnetic fields, but conductive components encasing the motor and driving voltage can create image distortions if operated closer than 0.5 m from the image isocenter [26]. Ultrasonic motors are compact in size and light in weight with high power/weight ratio, and high efficiency but if directly coupled they provide low speed and high holding torque [27].

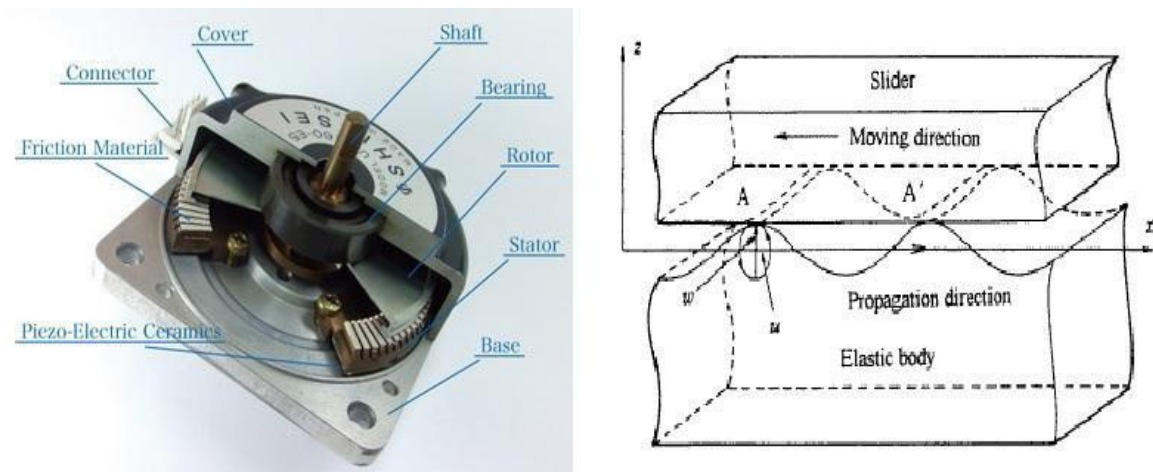


Fig.1.7: (a) Photograph of Shinsei corp. ultrasonic motor [28] (b) Principle of the propagating-wave type motor [27]

This high holding torque maintains the motor current position when the motor loses power. In case of malfunction this feature is considered as a drawback by some as an advantage by others. Disengaging of the motor from the system can be achieved by using mechanical clutches as implemented by Chinzei & Miller [24] and Koseki et al. [25].

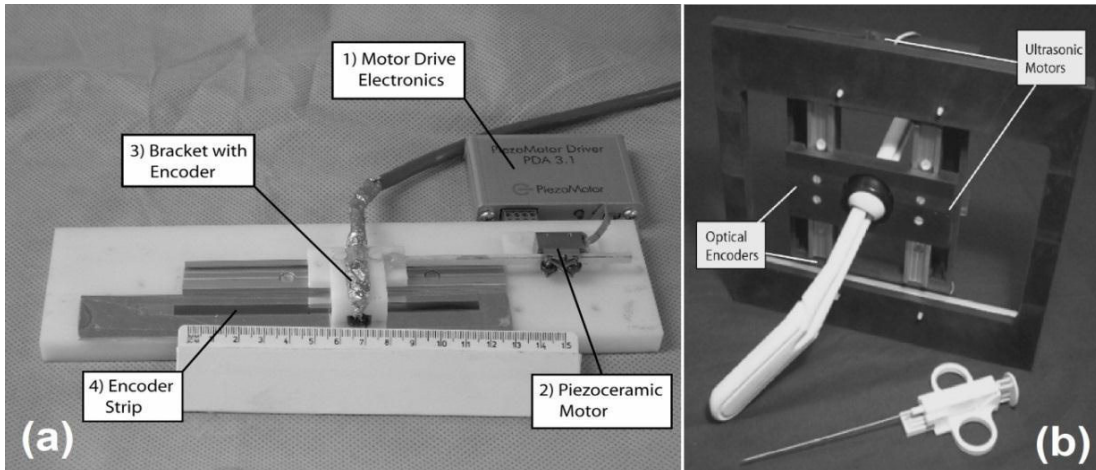


Fig.1.8: (a) 1 DOF stage with ultrasonic piezomotor. (b) The 5 DOF manipulator [29]

In [29] a five DOF MR-compatible prostate biopsy manipulator has a master-slave configuration work with linear ultrasonic piezomotors (see Fig.1.8), supporting structure from Delrin and aluminum. The motor has maximum force of 7N and maximum speed of 12.5 mm/s. Fig.1.9 shows another MR-compatible prostate biopsy manipulator consisting of three stages and possesses 3 DOF. It employs linear ultrasonic piezomotors for each stage and the structure is constructed from Delrin. Its performance is 17N of force and a speed of 2.7 mm/s [30]. In spite of the good performance the two previous examples, they are large in size and complex to control. The mentioned reasons are the main factors for not considering this method as a favourable actuation method for the developed actuator.

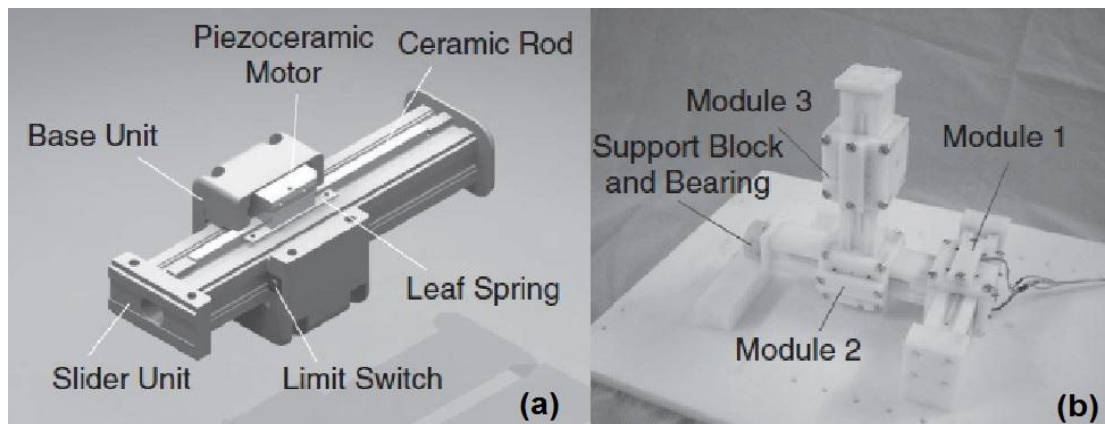


Fig.1.9: (a) CAD model of one stage (b) Three stages interconnected [30]

1.3.4 Manual actuation method

Example of a manual 3 DOF actuated manipulator for prostate interventional procedure under magnetic resonance imaging guidance was presented in [31]. The device is actuated remotely by means of flexible shafts and capable millimeter accuracy for the needle placement. The device consists of a positioning stage that acts on a lead screw through a threaded nut for linear motion. Rotation is provided through the motion of the whole assembly inside a fixed internal gear in a planetary gear configuration. Fig. 1.10a shows components of the mechanism including the enclosing housing [7, 31].

To avoid image distortion the main components of the device are constructed from plastics with minimum amount metallic small parts. Gears were made from brass and ball joint from aluminum. The motion controlling shafts were constructed from phosphor bronze allowing remote actuation under control of the practitioner. The device was tested in a 1.5 Tesla scanner with a precise image guided targeting of the needle [31]. The design of the device is simple but was developed for prostate intervention and operates outside of the scanner bore so size was no issue for this purpose. This method of actuation is not appropriate for our proposal as size and maneuverability is a concern (Fig. 1.10b).

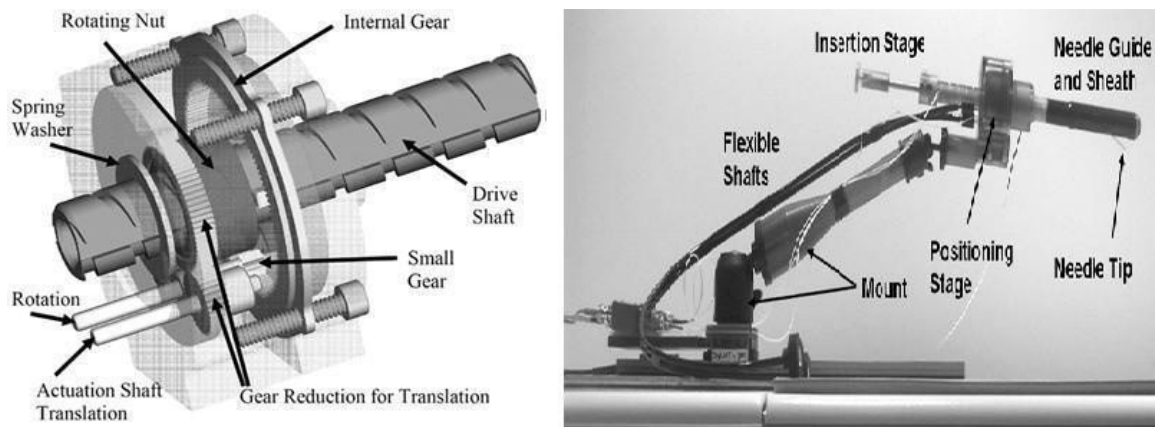


Fig.1.10: (a) Planetary gear mechanism. (b) Picture of the manual actuator showing different components [31]

1.3.5 Other actuation methods

Other nonconventional types of MR-compatible actuation are as follows [2, 32]:

1. Electrostatic Actuation method is MR-compatible materials as it does not contain any ferromagnetic materials. A linear electrostatic motor was evaluated in [33]. The high power electrostatic linear motor proved to be MR-compatible and does not affect MRI imaging. The maximum thrust force was around 10 N at driving voltage of 1.6 kV. Another film-based actuator was presented in [34]. This strong motor was not tested in the MRI scanner. The maximum thrust force was 310 N at 1.4kV. However, the power electronics of the electrostatic actuators still require development before becoming an alternative [32], and also the high voltage can be a safety concern.
2. Electrostrictive polymer actuators (EPAM) were investigated by Vogan et al. [35]. The compatibility of EPAM actuators and in MRI was demonstrated without degrading image quality. Silicone-made contractile dielectric elastomer actuators were tested in [36] and there was no degradation of both the actuator performance in the MRI environment either when powered by AC or DC voltage. This method needs high voltage for actuation which can be a safety hazard.

1.3.6 Summary

Some actuators cause image distortion when they are too close to the imaging area. Transmission systems such as shafts, belt or chain drive systems must be used when the motors is placed remotely from the scanner leading to performance limitations such as joint flexibility, backlash, and friction. Other actuators are complex to control, have safety issues, and lack compactness in size, these issues can be addressed by proposing a new method of actuation for MR-compatible actuation that is stiff, compact, and create enough force to perform successfully inside the magnetic environment without degrading the imaging performance of the scanner. The actuation method proposed in this work is piezoelectric actuation method as it is MR-compatible, compact in size, generates high force and easy to control, details of this method will be discussed in the next section.

1.4 Piezoelectric Actuation method

Several types of piezomotors have been developed by researchers over the years and they can be grouped into two major groups; the first group is ultrasonic motors and the other is discontinuous motion motors. In the first group (ultrasonic motors) the output member is constantly in contact driving member and the piezoceramic is driven at an ultrasonic frequency range which is the ceramic resonant frequency. To control the speed of this motor the drive signal amplitude is varied while the drive signal frequency is kept constant. Examples for this group of motors are Travelling Wave [37], Elliptical Push [38], and π -shaped motor [27]. In the second group (discontinuous motion) moving to the desired position involves a sequence of clamping and extending operations. The speed can be controlled by varying both the amplitude and the frequency of the drive signal. Examples for this group are piezoworm [37], caterpillar motor [39], and walking motor [40]. In the thesis we are interested in the second group (discontinuous motors) as it generates high force and easy to control and specifically the piezoworm because it is the simplest and most cost effective in this group.

1.4.1 Introduction

In [41] a brief history of piezoelectricity was presented. It was stated that the name ‘piezoelectricity’ is the direct translation of the Greek word piezein which means “pressure electricity”. It was continued that the phenomenon was discovered by the Curie brothers Jacques and Pierre in the 1880, the observation they made was noticing the electrification of certain natural crystals under mechanical pressure.

The piezoelectric phenomenon was explained in [41] as the development of electric charge inside the piezoelectric material in response to the mechanical stress applied. It is continued that the direction of the stress affects the polarity of the charge meaning that tensile stress will produce a reverse charge of the tensile one. Piezoelectric material is capable of the inverse piezoelectric effect, when an electrical field is applied the material deforms in the direction of the strain inversely proportional to the direction of electric

field. Also shear piezoelectric effect is possible [41]. One of the common piezoceramics is the lead zirconate titanate ($\text{PbZrO}_3\text{-PbTiO}_3$) or (PZT) [43]. In this research PZT is used in the piezoworm actuation method used in form piezoelectric stacks (Fig. 1.11) which generates high force in a small package and are MR-compatible.

1.4.2 Piezoelectric stack actuator

Motors are developed using piezoelectric actuators concepts as they can endure very high compressive forces, generate high load capacity, possess high stiffness, short response time, high acceleration and offer theoretically unlimited resolution [42]. Piezoelectric actuators consumes very small amount of power as it behaves like a pure capacitive load [42]. On the other hand, piezoelectric actuators operate with potential differences between 100-1000V, have very small strains rates, exhibit hysteresis, creep (drift), and aging. The most commonly used piezoelectric actuator is the stack actuator as can generate the highest forces and long travel ranges [42].

Piezoelectric stacks are constructed from multilayers and each stack is composed of several piezoelectric layers as shown in Fig.1.11. Linear displacement is produced due the piezoelectric effect when the voltage is applied. Since the ionic shift and orientation of the PZT unit cells is the base for displacement of a piezo actuator, the resolution depends on the electrical field applied [42]. As there are no threshold voltages for displacement the resolution is theoretically unlimited. This make the voltage source stability very critical and position changes can be caused by noise even in the μV range [42].

The application in question dictates the size of the required dimensions of the stack. The displacement is usually a percentage of the height (up to 0.2%) and the cross sectional approximately proportional to the produced force [42]. Fig.1.12 shows two stack actuators from Physik Instrumente (PI) GmbH & Co. The two types of stacks used in the actuator are from the same company, one having dimensions of 5x5x18 mm provides a displacement of 15 μm and a blocked force of 900 N and the other having dimensions of 5x5x9 mm provides a displacement of 6.5 μm and a blocked force of 800 N.

1.4.3 Piezoworm motors

Typically a piezoworm linear or rotary motor has three piezoelectric components: two clamping actuators and one extending actuator.

The motor moves to its commanded position by using sequential clamping and extending action to realize a step either forward or backward [44]. Fig.1.13 presents the principle of the piezoworm sequential linear stepping. Size and rate of the step can be controlled to achieve the desired performance. This range of motion can be in centimeters range and realizes nanometer scale accuracy.

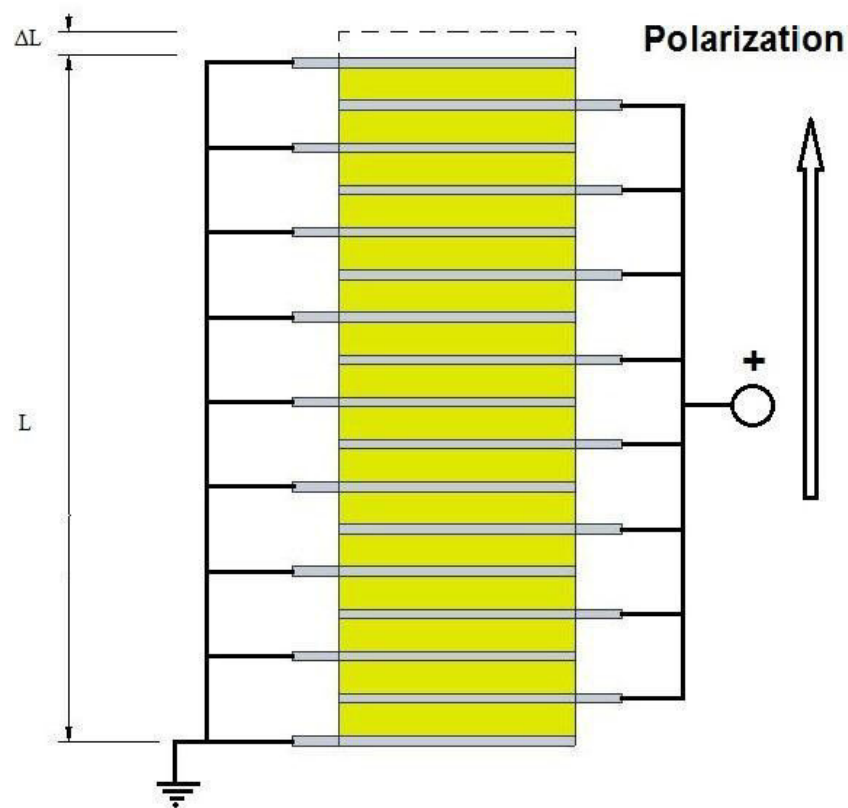


Fig.1.11: Structure of a piezoelectric stack [42]



Fig.1.12: Piezoelectric stacks from Physik Instrumente (PI) GmbH & Co. [43]

As mentioned earlier the material of the stack actuators used is usually PZT (Lead Zirconate Titanate). The stacks consists of many thin PZT wafers glued together and are utilized in the direction of motion that produces large force (1000 – 30,000 N) but small displacements (strain < 0.02%) [45].

Piezoworm actuators utilize the normal forces and friction coefficient between moving and the stationary parts to transmit loads through frictional clamp producing output forces in the range between 3 N to 200 N [45]. The output forces can be increased by properly developing an efficient clamping mechanisms to transfer most of the PZT produced force as demonstrated in [46, 47].

With proper design of clamps the piezoworm configurations can potentially have a high force/size ratio and still possess moderate speed making this configuration ideal for high force and restricted space applications.

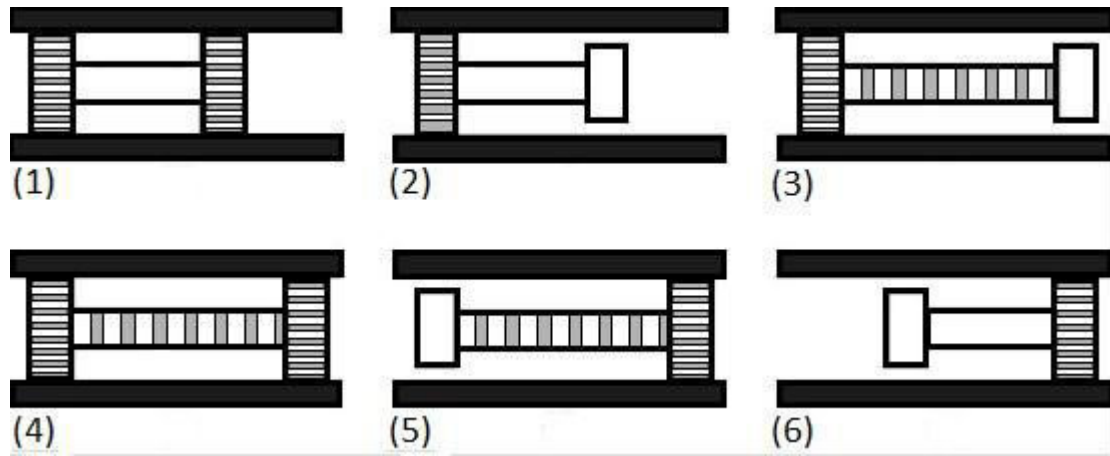


Fig.1.13: Operation principle of piezoworm and sequential stepping

1.4.4 Summary

The proposed device design will be based on the piezoworm principle of actuation. The device will be compact and powerful enough to function inside the scanner bore. Furthermore, constructing the enclosing and supporting structure from nonmagnetic materials, and using piezoelectric materials for actuation will make the device design MR-compatible. The component constructing material mechanical properties should be evaluated for strength and stiffness for the device to function properly which will enhance the overall system performance. Another advantage for the proposed concept is the vibrational nature of the piezoworm setup will help in the safe piercing of the tissues makes it the ideal method of actuation for our purpose.

Finally, to achieve combined linear and rotary motion in a compact size configuration, innovative design methods have to be used. Literature survey of piezoworm designs will be presented in the next section.

1.5 Piezoworm Motor Designs

In literature the piezoworm is categorized based on the design configuration, but to distinguish between the different types of motion the following categorization of designs will be used to differentiate between each type:

- Linear motion designs
- Rotary motion designs
- Combined linear and rotary motion designs

1.5.1 Linear Motion Piezoworm Motor Design

Linear piezoworms fall in one of three fundamental groups [48], in the first group the actuation mechanism moves with the connected shaft along the actuation path. This configuration is known as a “walker”. The “pusher” is the second configuration. Here, the actuation mechanism is fixed and not connected to the shaft. The extender incrementally pushes the clamped shaft along the actuation path using piezoworm technique. The final configuration is the “Hybrid” which is a mix between the two previous groups [48].

Hsu [49] introduced the first piezoworm actuator that was patented in 1966. The design was a “Hybrid” actuator that used a single hollow cylindrical element to extend. As shown in Fig.1.14. The clamping device consists of balls wedged in an annular circular slot holding on the shaft. A ball is held by means of a spring from one side and by a two layer piezo disc from the other side. When the disc is energized the ball moves towards the bigger area of the wedge releasing the shaft which is now free to move in one direction. By alternating between the two clamps reverse direction can be achieved [48].

A more precise "Hybrid" piezoworm actuator was developed by Locher 1967 [50]. The device was able to achieve individual steps of 13 μm . The concept behind this idea was the use of clamping elements to engage one of the shaft ends when it is extending while the other element is free, this mechanism is known as "clam-claw" mechanism and is shown in Fig. 1.15 [48].

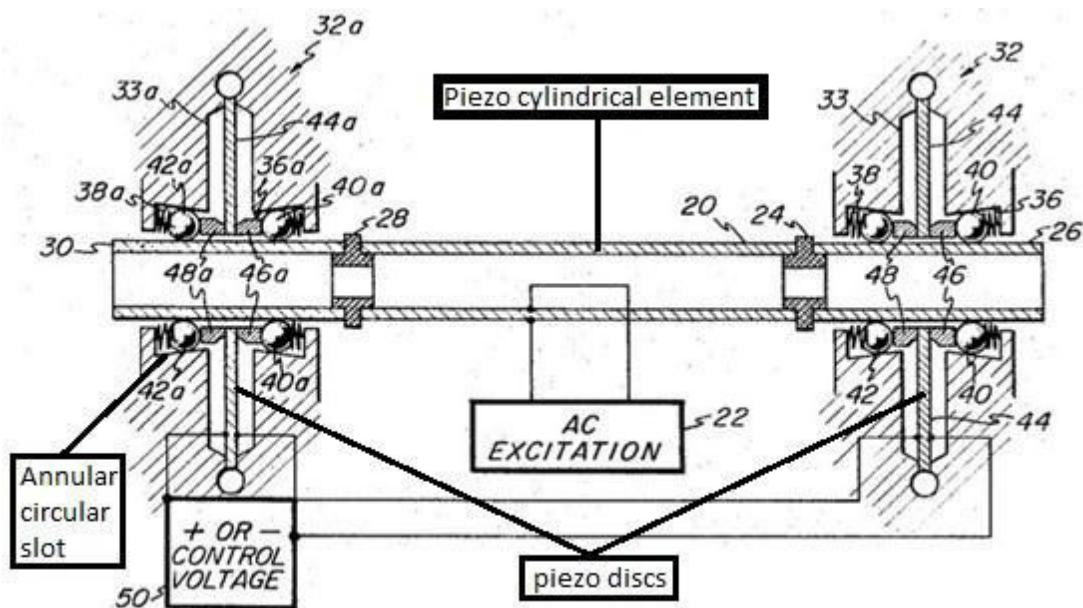


Fig.1.14: Hsu “Hybrid” piezoworm design [49].

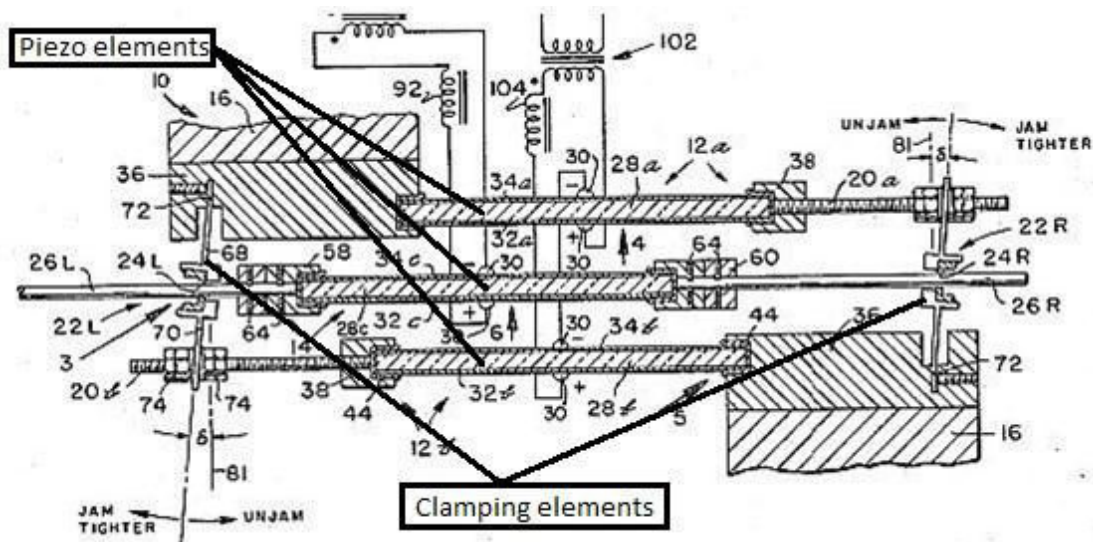


Fig.1.15: Locher “Hybrid” piezoworm mechanism without all electrical circuitry [50].

In 1968 the first “walker” was developed by Brisbane [51] the design was very simple as shown in Fig.1.16 with an increment step size of $5\ \mu\text{m}$ [45, 48]. Cylindrical piezoceramic elements were used with the intention to achieve micron range positioning for tooling with speed of 50 mm/sec [48].

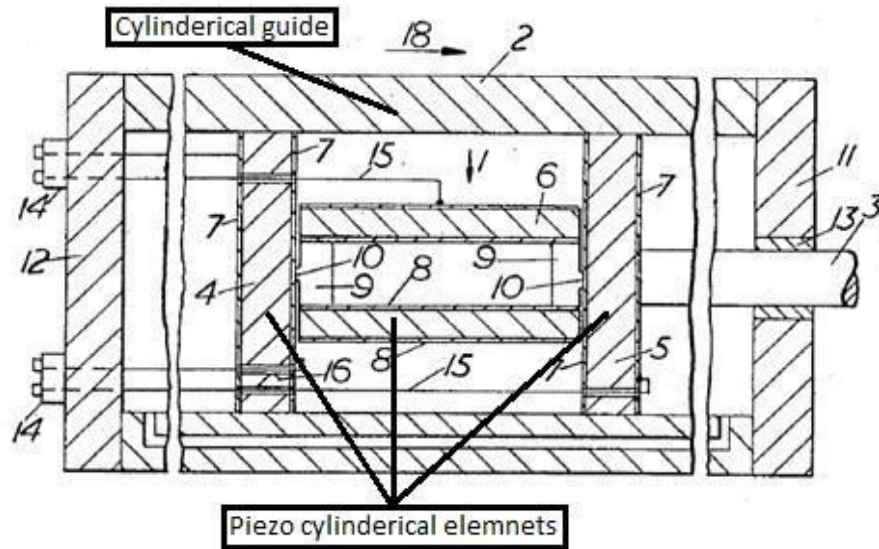


Fig.1.16: Brisbane “Walker” piezoworm design [51]

Galutva et al. in 1972 [52] is the first example to use piezoelectric stacked actuators to create a piezoworm motor of the “Walker” type. The piezoelectric stacked actuators were used both to create the forward motion and to directly clamp the walls of the guideway. The motor moves through a guideway by utilizing its clamps and extension parts [45]. One of the most important piezoworm motors of type “Pusher” was introduced by Bizzigotti and May [48]. The design was produced by Burleigh Instruments Inc. [53] and was used as a basis for their production Inchworm motors in 1975 for 30 years under the commercial name Inchworm® [45]. In this case, like the “walker” type piezoworm, the clamps and the extension actuator are stationary and responsible for generating movements. However, a shaft is moved instead of the motor body (see Fig.1.17).

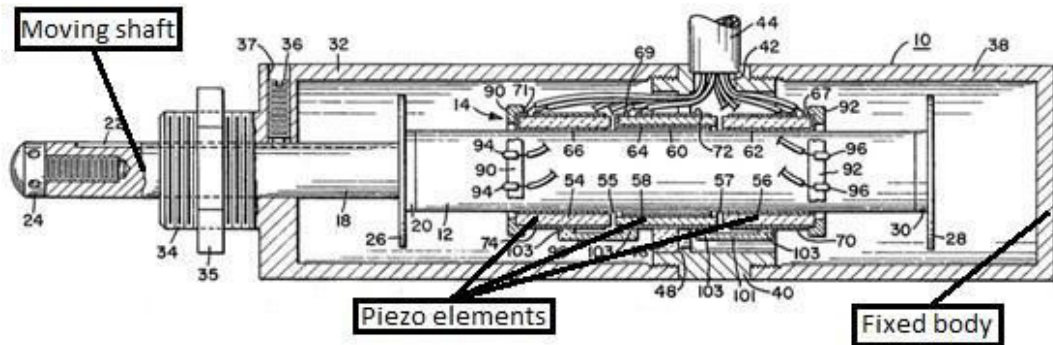


Fig. 1.17: Burleigh Inchworm® design [53]

Since the 1960s, there is an immense interest in researching piezoworm motors research. There have been two main trends for this interest the first was large scale applications such as space structures and precision machine tools and the main objective here is long stroke and large output force for the device [45]. The other branch is focusing precise positioning for applications such as MEMS applications.

One of the first designs for precision tools is the work done by Zhang and Zhu [44]. The actuator uses monolithic flexure structures and preloaded devices to protect piezoelectric stacks from bending or shearing stress during operation and increase the device stiffness (see Fig.1.18). The device produces very large output force 200 N with range of 300 mm and speed of 6 mm/s.

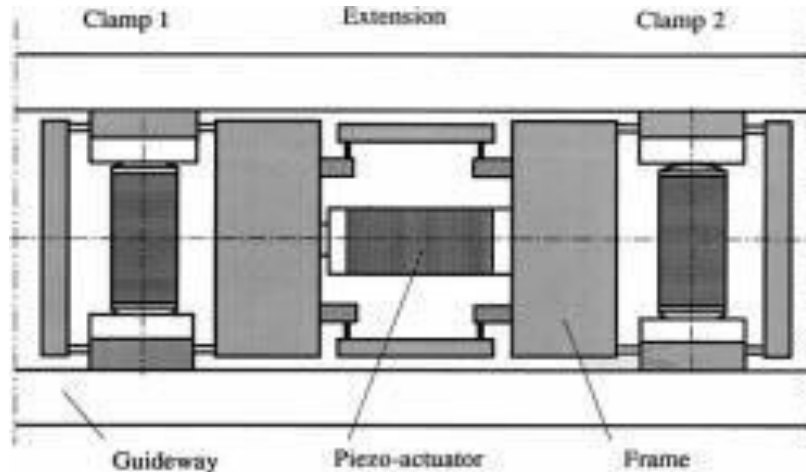


Fig. 1.18: Zhang & Zhu piezoworm design [44]

Another device was developed by Tenzer and Ben Mrad [54]. A piezoworm positioner developed was shown to have stiffness in the direction of motion of $88 \text{ N}/\mu\text{m}$, a maximum thrust of 150 N and a traversing speed of up to 20 mm/s .

In [55] a novel proof of concept prototype Mesoscale Actuator Device (MAD) has been developed. The MAD is similar to piezoelectric driven inchworm motors with the exception that mechanically interlocking micro-ridges replace the traditional frictional clamping mechanisms to increase the output force and the device had a maximum speed of 5 mm/s and a thrust of 245 N . Also [56] worked on the same idea of micro-ridges but with a different profile for the teeth, the performance of the actuator was speed of 11 mm/s load capacity of 450 N .

Increasing the stroke of the extension by using amplification mechanism was investigated by Tenzer et. al [57] the results showed that the amplification is inversely proportional to the square of the lever ratio which decreases the stiffness of the flexure dramatically.

The second trend group for precise positioning was the work done by [58] a piezoworm linear motor was developed with a reduction lever mechanism providing ultra-high positioning accuracy. It consists of a push pull mechanism and the step movement of $1 \mu\text{m}$ to $82.5 \mu\text{m}$.

Summary

The “Hybrid” and the “Pusher” type are simpler than the “Walker” type in terms of operation and manufacturing. In the “Hybrid” and the “Pusher” piezoworm, the fixed clamps reduce the complexity during large step positioning. Nonetheless, the “Walker” type has advantage of providing higher load capacity for the same size motor because there is more surface area for the clamps to contact which means higher friction forces.

The pusher configuration is more favorable for the proposed actuator as the shaft weight is less than the other elements hence will be more responsive and image distortion will be minimal.

1.5.2 Rotary Motion Piezoworm Motor Design

Rotary inchworms are not commonly used as ultrasonic motors and are not well researched as their piezoworm linear counterpart. But on the other hand they have an advantage over designs involving the use of torsional or obliquely polarized piezoelectric elements that produce angular motion. The output and static torque of these torsional elements is limited to the direct carrying capacity of the element [59, 60]. Furthermore, the difficulty of obtaining continuous rotary motion from torsional piezoelectric elements without complex designs did not make this actuation method a good alternative for the proposed actuator and was not surveyed in this work.

The rotary inchworm has the same principle of motion as linear inchworms. There is a rotational mechanism instead of the extension one in the linear motion. Two sets of clamps exist for holding and releasing the rotary mechanism. Rotary inchworm motors can be grouped into three types:

- I. Disc motors – clamp on face of the disc (Fig.1.19) [61, 62],
- II. Drum motors – clamp on inside diameter of drum (Fig.1.20) [63, 64],
- III. Shaft motors – clamp on outside diameter of shaft (Fig.1.21, 1.22) [65, 66, and 67].

Since the amount of torque is proportional to the clamping radius, the distance from the axis of rotation to the clamp point, the shaft motor will have much less torque than the disc or drum motors. However, it also has less inertia so it will be more responsive. The amount of rotation per step is inversely proportional to the clamp radius so the shaft motor will have a large step size. This means it can attain higher speeds but the resolution will be negatively affected.

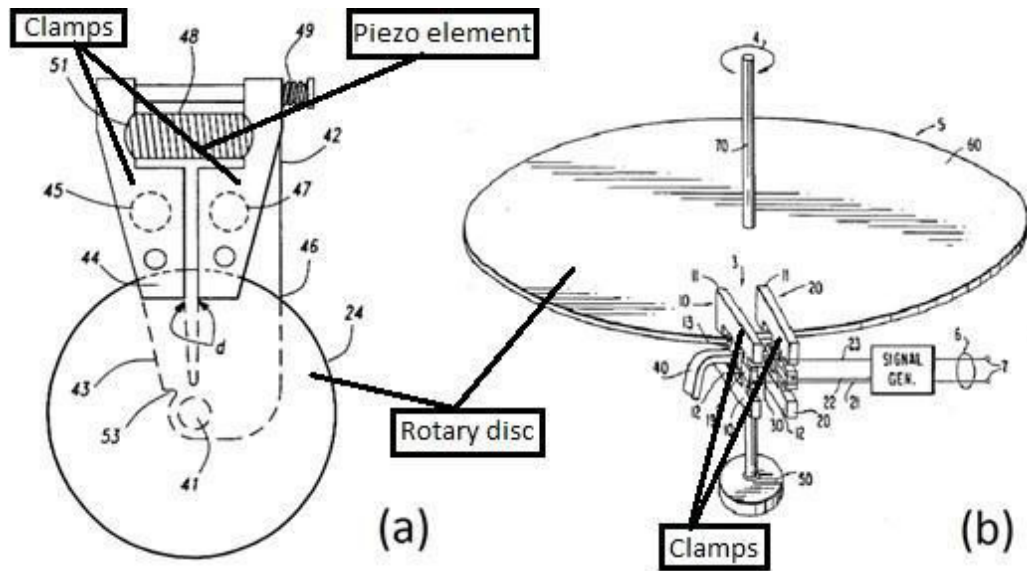


Fig. 1.19: Piezoworm disc motors (a) Oliver et al. (b) Fujimto [61, 62]

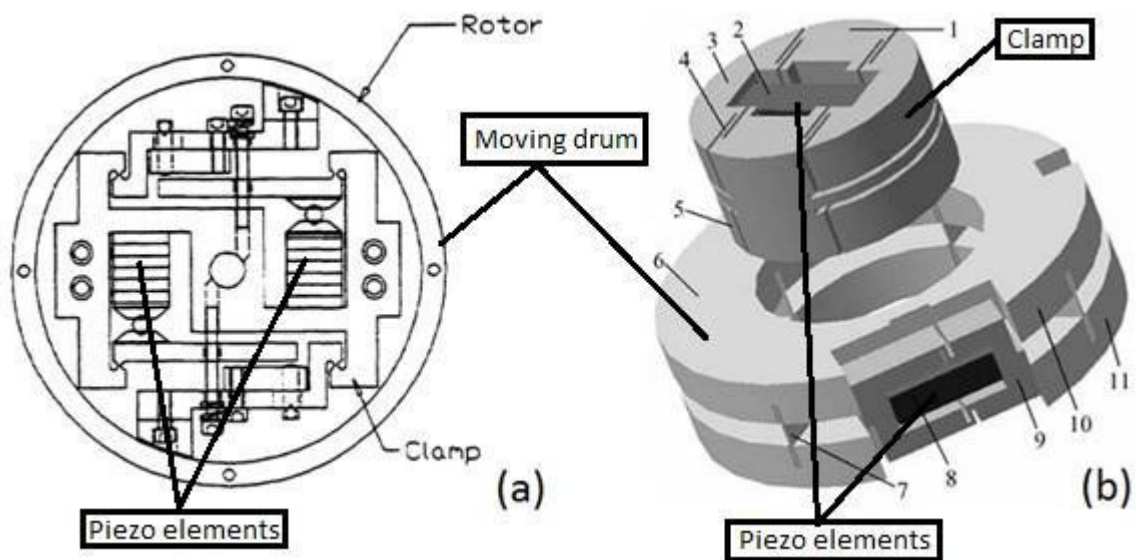


Fig. 1.20: Piezoworm drum motor (a) Duong et al. (b) Jianfang et al. [63, 64]

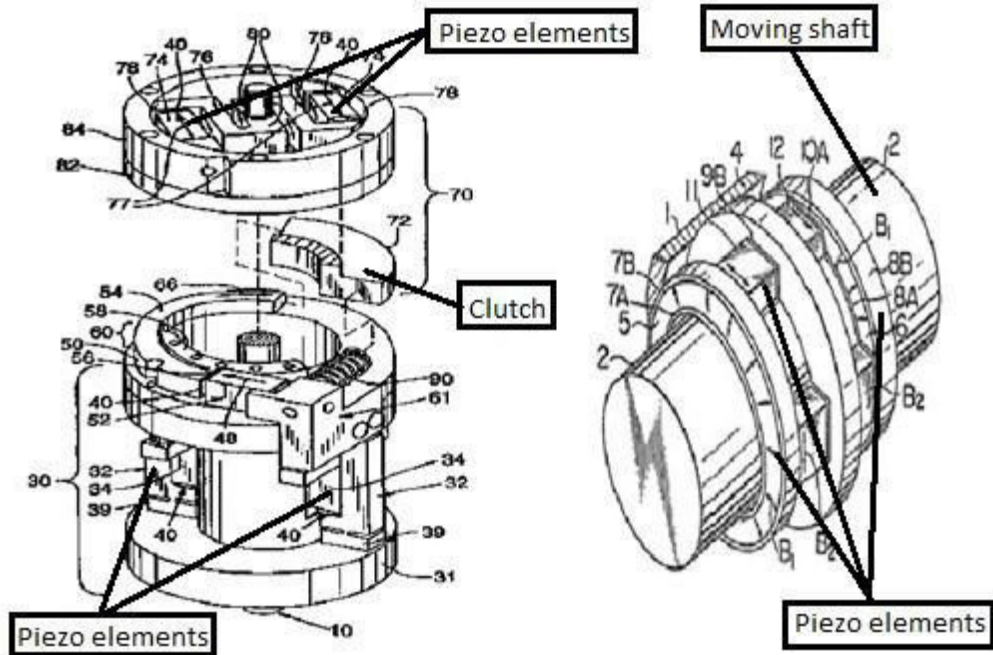


Fig. 1.21: Piezoworm shaft motors (a) Gursan (b) Mori [65, 66]

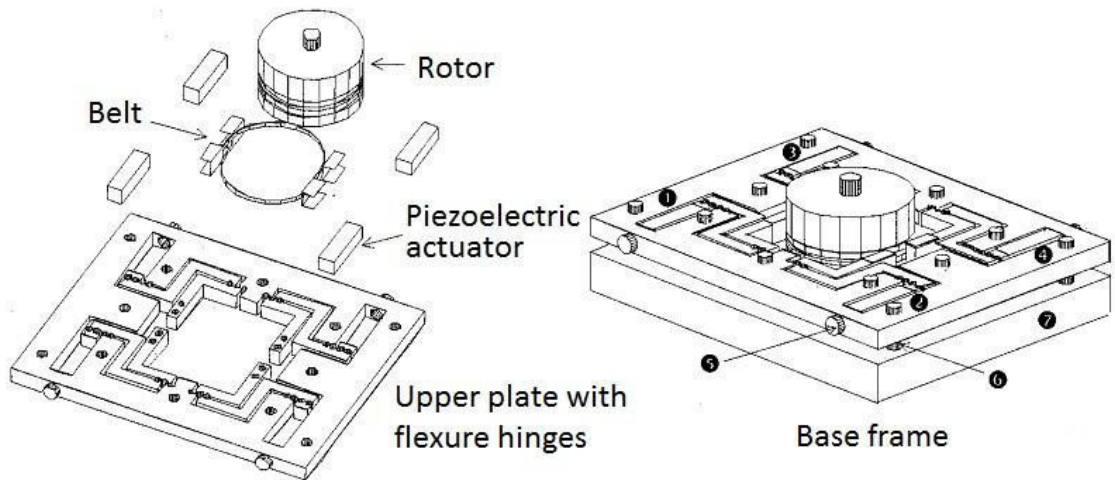


Fig. 1.22: Assembly diagram of shaft piezoworm motor actuated by belts [67]

Summary

For the types of the rotary motors surveyed, the disc type has most output torque, low speed, and is the least responsive. On the contrary, the shaft has the least output torque, highest speed, and is the most responsive. As for the drum type its parameters is intermediate between the two previous types. Since, the space is limited inside the MRI scanner and the compactness in size is crucial therefore the piezoworm shaft motor principle is ideal for the proposed actuator. It is more compact than the disc or the drum type and more responsive. Furthermore the torque needed to rotate in soft skin tissue is low but response time is a key in the motor performance.

1.5.3 Hybrid Motion Piezoworm Motor Design

To the authors' knowledge combined linear and rotary piezoworm actuation for MR environment was not used in the literature except for [69] as it is challenging to create the combined motion using off shelf components. Hence, innovative design methods have to be utilized to achieve this task. In this section some of the state of art combined actuation is presented which mainly is piezoelectric ultrasonic motor based.

The design by Staufenberg et al [68] was patented in 1986 (see Fig.1.23). The pusher type actuator was capable of translational or rotational motion. Clamping/tangential extension was applied by various actuators to produce the rotational motion. Similarly the translational method was realized but was using a rocking method to propel the shaft forward [48].

In [69] a rotary-linear piezoelectric actuator (RLPA) was presented. It is based on the principle of the ultrasonic motors. The stator of this motor is manufactured from a phosphorus bronze material for MR-compatibility. The stator is a rectangular solid with a through-hole where the shaft fits in with a non-clearance fit capable of sliding along rotating around the holes' axis (see Fig.1.24a). On the surfaces, four piezoelectric elements are bonded to the stator (see Fig.1.24b).

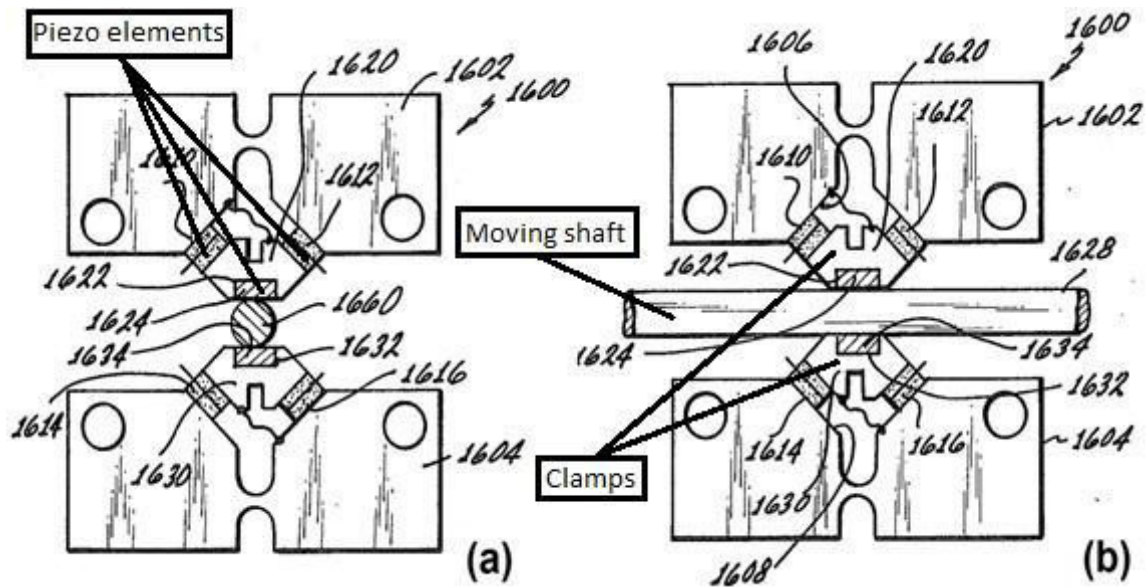


Fig. 1.23: Staufenberg clamping/tangential extension (a) rotation (b) translation [68]

The stator gets excited at its natural frequency by applying driving voltages to the piezoelectric elements and the inner surface of the stator generates elliptical motion. This elliptical motion can generate either linear or rotary motion at a given time. The generated linear/rotary motion is based on the friction between the stator and the shaft surfaces. The cubic stator dimension in this experiment was 14 mm with a hole of diameter equal to 10 mm, the reported maximum torque and rotary speed were 2.5 N. mm and 120 rpm and the maximum thrust and linear speed were 0.33 N and 85 mm/s. The device was tested in 0.3T MRI machine and was proven to be MR-compatible.

Another experiment was conducted on the actuator outside the MRI machine using a steel shaft with values of 160 rpm and 63 mm/s at voltage of 42 V were reported in [70]. The device was miniaturized to a cube size of 3.5 mm and hole size of diameter of 2.5 mm and the results for the experiment were rotary motion of 229 rpm and 2.5 N.μm and linear motion of 80 mm/s and 2.6 mN was observed at voltage of 42 V [71].

In [72] an MR-compatible actuator 2 DOF actuator design for needle insertion actuator with a fiber optics force sensor feedback was introduced (see Fig. 1.25a).

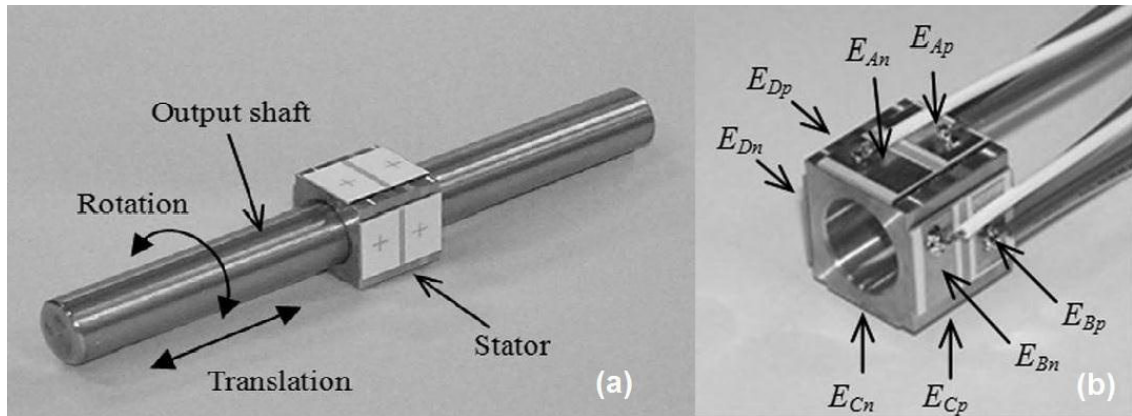


Fig. 1.24: (a) Schematic of the RLPA (b) Stator and the applied voltages [70].

The actuator is capable of simultaneous rotation and translation of the needle and is mounted on 3-axis linear stage for positioning the needle insertion point (see Fig.1.25b). The device is remotely operated and based on master-slave configuration. Ultrasonic motors capable of creating 10 N of force, and up to 16 N holding forces were used for linear actuation. The system material includes high strength plastics (Ultem and PEEK), DRYLIN and aluminum for MR-compatibility.

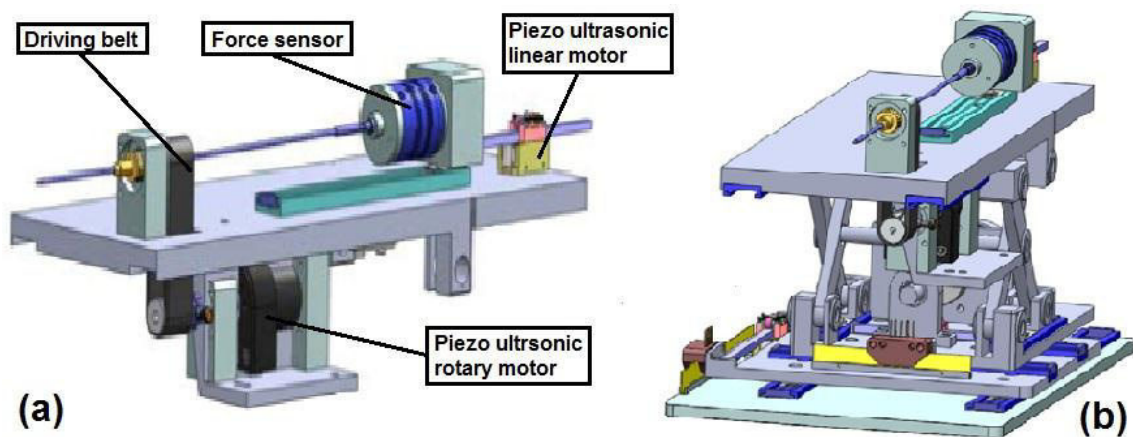


Fig. 1.25: (a) CAD model of the needle drive (b) mounting of the actuator on the stage for needle rotation and transition motion [72].

The envelope dimension of the positioning stages is 25 cm by 15 cm by 18 cm with a horizontal translation of 5 cm, vertical translation of 5 cm, and insertion translation of 10 cm which is sufficient when working out side of the confined MRI bore space. Furthermore no performance data was reported and the use of the driving belt concept to transfer rotary motion decreases the compactness of the device to be an attractive alternative for the proposed device.

Summary

The design by Staufenberg [68] is the simplest in concept as it does not need complicated driving signal as the other two ultrasonic motors design but no combined motion was reported. The exceptional idea of using the same element for rotation and translation (shaft) is also used in [69] which ensure the size compactness but the output force and torque is very low. Using a separate actuator for each type of motion as in [72] makes the actuator bulky for use inside the scanner. The idea of the shaft rotation and translation is well suited for the proposed device to keep the image distortion to a minimum level when present in the FOV of the MRI scanner.

1.6 Thesis Outline

The thesis outline is as follows:

Chapter 2: discusses the concept of MR- safety and MR-compatible materials through the testing of twelve engineering materials. The work in this chapter focuses on the effects in the MRI due to the material susceptibility, induced forces, torques, and image artifacts.

These materials were selected based on their hardness, stiffness and strength. Theoretical estimation and experimental validation was carried out and trends were presented. This chapter serves to aid designers/engineers to estimate the MRI compatible material performance before the expensive step of construction and testing.

Chapter 3: presents the experimental work done in testing the twelve engineering materials in term of induced heating inside the MRI environment. It discusses in detail induced heating due to gradient and RF fields. Theoretical models augmented using finite element analysis is used to consider several geometrical shapes under gradient heating. The results are validated through bench-top experiments.

Chapter 4: is an overview of the design process the piezoworm motor based on the flexure mechanism and complementary clamp configuration. This chapter discusses the design configuration used in the development of novel actuator from the choice of the moving shaft concept to produce the minimum image distortion possible without affecting other parameters.

Chapter 5: presents the static and dynamic performance of the manufactured prototype. An experimental assessment of the effects of the frequency and applied force on the piezoworm performance is demonstrated. The comparisons between the analytical and experimental results were discussed.

Chapter 6: summarizes the entire project, and proposes future work.

1.7 Thesis Objectives

The main objective is to develop a 2 DOF piezoelectric actuator to perform inside the MR environment with micrometer range accuracy, and targeted design parameters presented in chapter four as follows:

- Analyzing the performance of candidate engineering materials in the MRI environment and comparing them in terms of expected forces, torques, and image artifacts.
- Analyzing the performance of candidate engineering materials in the MRI environment in terms of induced gradient and RF heating for safety considerations.
- Developing a novel MR-compatible 2 DOF compact actuator design with complementary clamps mechanism.

1.8 List of Contributions

The list of research contributions presented in this thesis is as follows:

- A quantitative comparison tool for aiding designers/engineers to have an estimate of the MRI compatible material performance before the expensive step of construction and testing.
 - Modeling and experimental validation of 12 engineering materials used in MRI environment in terms of induced forces, torques, and image artifacts.
 - Modeling and experimental validation of 12 engineering materials used in MRI environment in terms of induced heat in sample material.
- Development and modeling of a novel concept for combined linear and rotary motion for piezoworm actuator employing complementary clamps.
- Implementation of the novel design in a compact prototype for an MR-compatible actuator with a large load capacity and moderate linear and rotary speed to work deep inside the MRI machine for accurate needle insertion procedures. The prototype was subjected to several tests to assess its performance.

Chapter 2

Predictions of Force and Image Artifacts in MR-Environment

2.1 Introduction

Magnetic resonance imaging (MRI) has become a standard diagnostic tool in hospitals around the world. MRI is famous for being incompatible with inclusion of foreign materials or objects. Despite this reputation, MRI is increasingly being considered for use in performing image-guided interventional procedures.

When developing tools and devices to support procedures conducted within the MR, the first question is inevitably which material should be selected. The first and most obvious exclusion criterion for a device material is that the material must not experience magnetic force that is very large compared to the weight of the object. This means that the choice is restricted to nonmagnetic or slightly magnetic materials. Susceptibility, χ , is used to characterize how easily a material becomes magnetized in a magnetic field and is related to its magnetic permeability by $\mu = (1+\chi)$ [15]. Although it is often assumed that only plastics are compatible for use within an MRI system, this is not the case, with many metals proving themselves compatible under many circumstances. Even many commonly available grades of stainless steel can and are used routinely within MR systems.

Unfortunately many of the least magnetic materials such as plastics do not have desirable mechanical properties in terms of hardness, stiffness and strength.

An overview of design considerations for devices in MRI is given in [73]. A detailed approach is described in [74] where a set of equations are used to establish upper bounds on the susceptibility of the material based on thresholds on induced force and image distortion. However, the paper does not include experimental validation or consideration of different scan sequences. Many devices have been developed and tested for MRI-compatibility [75-80], but the results are too specific to the devices to be able to generalize or relate to a new device in development. Some studies have focused on more generalized testing [81, 12]. In [12], beryllium-copper and four types of steel cylinders were studied but the results were compared qualitatively and only one scan sequence was used. The results in [81] are far more extensive with 22 engineering materials (seven metals) studied using two scan sequences. The materials were compared quantitatively using the extents of the image artifact. However, the study did not relate the size of the artifact to the material susceptibility or to the scan sequence parameters. Both [81, 12] do not attempt to predict the size of the artifact which is useful to the engineer in the design phase. The static field perturbations can be estimated numerically based on the effect on susceptibility of the materials [82-85]. The focus of these studies was on improving the image quality and not estimating the size of the artifacts and the algorithms are not easily utilized for design.

Additionally, they did not compare the results for different scan parameters and materials. In [86], a number of stainless steel and titanium needles were examined with 8 different scan sequences but the work is not easily extended to other objects as no analytical estimates were made. A set of papers [87-89] investigated the use of numerical simulations to predict the region of distortion for needles for various scan sequences.

The focus of these studies was the artifact around the needle tip and the predicted artifact and experimental artifact were not directly compared quantitatively.

In this research, a quantitative comparison of engineering materials in the MRI is presented. A comparison to theoretical behavior is also made in order to provide a designer/engineer a rough estimate of the expected MRI performance before the expensive

and time-consuming steps of construction and testing. The specific focus of this chapter is on the effects in the MRI due to the material susceptibility alone, namely the force and the image artifacts. Experiments were performed on slender cylinders of twelve common metals. A cylinder is a common shape in devices in terms of fasteners and shafts and it is easily modeled in the theoretical analysis. The goal is to provide rough answers to basic questions, such as the following: “Is it possible to obtain essentially normal MR images in the vicinity of a stainless steel rod? How far from the imaging region would such a rod need to be? “Does it need to be 1 m away? 10 cm away? 1 cm away?”. These are important and apparently simple questions, yet it is very hard to answer them based simply on a first-principles analysis. The results of this research will provide answers to these basic questions for commonly used engineering materials.

2.2 Background and theory

The challenge in understanding how different materials will behave when exposed to the practical MR scanner environment is easy to appreciate once one realizes the complexity of the electromagnetic environment within the scanner. A very strong, static magnetic field is always present within the bore of the MR system. This field is typically between 1 and 3 T (with 1.5 T and 3.0 T systems by far the most common field strengths in clinical use), and is uniform to several parts-per-million over the 40 to 50 cm diameter imaging volume. Outside this imaging volume, which is located at the center of the system, this static field varies spatially, falling to a fraction of the main field value once outside the bore. Fields in excess of 5 mT extend out to distances of several meters from the magnet. Superimposed on this static field is a time varying, spatially varying magnetic field which is modulated with a complicated and application-specific waveform in the low audio-frequency band (typically most power is near 1 kHz). This audio frequency time varying magnetic field is called the gradient field. Typical peak amplitudes of magnetic field produced by the gradient system can be as high as a few tens of μT .

The dB/dt associated with the rapidly switched gradient fields can exceed 100 T/s within the scanner bore, although values between 20 and 50 T/s are more typical. In addition, a

time varying and spatially-varying radio-frequency (RF) magnetic field is present, again in a manner which depends greatly on the specific MR-protocol being applied. The RF field has a frequency which is chosen based on the field strength of the scanner. The most common magnet field strengths of 1.5T and 3.0T have RF frequencies of approximately 63 MHz and 128 MHz respectively. The RMS amplitude of the RF magnetic field is typically between 3 and 5 μT for the most demanding MRI pulse sequences. The strength of both the gradient and RF fields fall very quickly beyond the imaging region of the system and are generally considered to be negligible outside the bore of the MR system.

It is difficult to fully model the behavior and effect that a sample of a given material will exhibit within the MR system. The different components of the electromagnetic environment mentioned above all have different effects on materials. Furthermore, the effect that a material will have on the otherwise normal operation of the scanner will depend on how that material interacts with the different fields. The parameters that can affect how a material behaves within the MR system include but are not limited to: magnetic permeability, electric permittivity, electrical conductivity, thermal conductivity, specific heat capacity and density. Further complicating this is the fact that many of these parameters, for example electrical conductivity, are strongly frequency dependent. Finally, the specimen geometry including the shape and surface area can be an important factor in the interactions with the MR system.

Sufficient data on the behavior of engineering materials is also not readily available and many reports in the literature are specific to a device and so general conclusions cannot be drawn. There are many interactions that can occur between a device component and the MR scanner. There are generally forces and torques experienced by the device when brought into the region of significant static field. Mechanical vibration can occur in the device due to time-varying eddy currents induced by the gradient fields. Heating of the device will occur both due to gradient-induced eddy currents, as well as RF eddy currents within the device. The presence of the device component will generally result in a distortion of the field uniformity of the scanner, with this effect increasing with the magnetic permeability of the object, as well as its size.

Image artifacts will result from magnetic field distortions due to the object. These artifacts can take the form of signal voids within the MR image, or spatial distortions of the object being studied. The force and torque effects, as well as the image artifacts, will be described in greater detail in the paragraphs below.

In order to make material selections at the design stage, one needs to estimate the effects of the material in the MRI. The calculations would be based on the specifications provided by the manufacturer of the MRI system. The accuracy of performing such calculations will be presented in the discussion section. The initial consideration would be the induced force caused by the spacial gradient of the static magnetic field. The materials considered in this chapter have sufficiently low susceptibilities that the concern is not structural failure but significant deflection could cause inaccuracies, impeded motion inside the device or become missiles if they were to come loose. From [90], an estimate of the force on a slender rod due to the static magnetic field, B_o , is given by equation (2.1) where F is force, χ is volume susceptibility, $\partial B_o/\partial z$ is the field gradient, μ_o is permeability in free space and V is volume of the rod. The force is highest where the product in the brackets is a maximum which is usually at the entrance of the MRI bore.

$$F = \frac{\chi V}{\mu_o} (B_o \partial B_o/\partial z) \quad (2.1)$$

The second major effect that the presence of a magnetic material has within the MR is to cause spatial distortions within images. MR ultimately achieves spatial encoding of the object via a phase-encoding of position, and this phase encoding is achieved by making the magnetic field across the object a known and controlled function of position and time. Anything that affects the magnetic field uniformity beyond what is applied during the imaging process confounds this encoding and results in an image distortion. Even the air-tissue interfaces within the human body result in image distortions; however, these tend to be small and well-understood. The presence of a foreign material sample generally presents a much larger distortion. The degree and nature of this distortion depends on both

the field distortion produced in the vicinity of the foreign device (which itself depends on the material, orientation and size of that device) and the exact MR pulse sequence which is applied. Different MR pulse sequences result in very different forms of image distortion for the same field distortion. The details of these effects are complicated but well understood within the MR community. We will outline the two basic classes of commonly used pulse sequences and the nature of the distortions produced by an object when exposed to each. Probably the most commonly used class of MR pulse sequences is the gradient echo (GE) sequence. In a gradient echo pulse sequence, a single RF pulse is applied at the beginning of the encoding process, which is then followed by a series of gradient field pulses. The gradient pulses can be positive or negative amplitude. Spatial encoding of the object is accomplished entirely by the timing and polarity of these gradient pulses. Each RF pulse is followed by a train of gradient pulses (sometimes called “lobes”), which continues for a time typically less (sometimes much less) than 100 ms.

The signal is read at the time TE (echo time) after the RF pulse. Another RF pulse is applied at a time TR (relaxation time) from the original RF pulse and the process is repeated. A full image is formed after several hundred RF pulses and corresponding gradient pulse trains. When there is field non uniformity present, GE images will in general exhibit image drop-outs or voids, and image spatial distortions or warping due to signal de-phasing [91]. If the field non uniformity is significant over the extent of a single pixel in the reconstructed image, the effect is a significant drop in the signal amplitude for that pixel. If the field non uniformity is not significant over a single pixel but still present, a spatial distortion is created, the exact nature of which depends on the precise nature of the field non uniformity and the specific gradient field directions applied during image acquisition. When a significantly magnetic material is within the imaging region, both effects will generally be present. A signal void will be seen in the immediate proximity of the material, and an image distortion will be seen in the area immediately surrounding the void.

The only means of reducing these effects is to increase the speed of the imaging sequence (which serves to reduce the amount of void) and to increase the strength of the gradient fields used during imaging (which results in reduction of the distortion area). The second major class of MR pulse sequences is the Spin Echo (SE) sequence. In SE sequences, multiple (typically two, but more are possible) RF pulses are applied, in addition to the gradient field pulse train. The second RF pulse is designed to influence signal phase within the object, which affects the spatial encoding. The important result in the present context is that the SE sequence causes a reversal and canceling of the de-phasing effects due to static field non-uniformities within the sample. This means that the signal voids which are typical of GE sequences are avoided when using SE sequences. The spatial distortions or warping still occurs however. In this study, both GE and SE sequences were used in order to characterize the material samples under both circumstances.

Estimation of the actual image artifacts outlined above is a complicated process which depends greatly on the specific details of the GE or SE sequences used. The analysis presented in [15] will be used, which simply considers the disturbances in the static magnetic field due to the sample. The analysis from [15] will be used to predict a radius around the rod which has significant distortion. The idea is that a designer would ensure that the component is sufficiently far away from the region of interest. For a slender rod of radius a perpendicular to the static magnetic field, the disturbance in the static field, B_z is given by equation (2.2) where x and z are perpendicular to the rod axis and z is parallel to the static field.

$$B_z = \begin{cases} \frac{\chi}{2} B_o & \text{inside the rod} \\ \frac{\chi}{2} B_o a^2 \frac{z^2 - x^2}{(z^2 + x^2)^2} & \text{outside the rod} \end{cases} \quad (2.2)$$

The position error, Δ_z (mm), is given by equation (2.3) where BW is the receiver bandwidth, FOV is the field of view and γ is the gyro-magnetic ratio.

$$\Delta_z = \frac{FOV(\gamma)}{BW} \Delta B_z \quad (2.3)$$

If equation (2.2) and (2.3) are combined, the resulting distortion pattern is cloverleaf shaped as shown in Fig. 2.1. To estimate the size of the distortion, a limit on Δ_z needs to be set Δz_L and then equation (2.2) and (2.3) can be solved to get the distance along the z-axis corresponding to this level as shown in (2.4). Both (2.1) and (2.4) will be compared to the experimental results.

$$z = a \left(\frac{FOV(\gamma)}{2\Delta z_L BW} \chi B_o \right)^{0.5} \quad (2.4)$$

2.3 Materials

2.3.1 Samples characterizations and properties

Twelve engineering material samples were evaluated during the experiment. These MR-compatible materials range from the first kind compatibility to the second kind as explained in [15], material are listed as per commercial name and Society of Automotive Engineers (SAE) Unified Numbering System for Metals designation in the Table 2.1.

All samples are round cylinders with half an inch diameter and five inches of length as shown in Fig. 2.2 and 2.3 [Right]. This shape was selected to present the most commonly used component in mechanical devices (screws, shafts, etc...). Table 2.2 shows some of the main properties of interest for the sample materials namely susceptibility, modulus of elasticity, and yield strength. Samples were arranged in this table according to their susceptibility property values in an ascending order and not according to the testing order and this arrangement will be used for identification throughout the text. Sources for all properties in Table 2.2 are from [92-96]. Note that the value of the volume susceptibility for brass 360 specified in the literature seems to be off by two orders of magnitude as will be discussed later. The value listed in table is the corrected value.

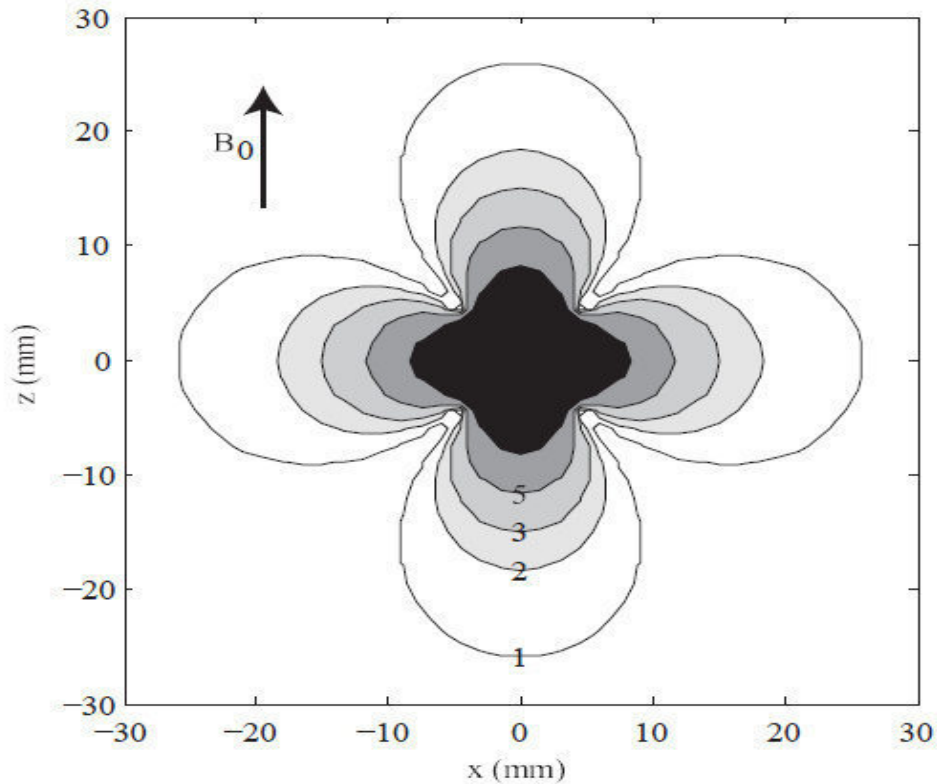


Fig. 2.1: The contours of constant ΔB_z (theoretical distortion region)

Table 2.1: Unified Numbering System for Metals designation

| | | Material Name | UNS |
|-----------------------|-------------|--|--------|
| MR compatibility kind | First kind | Ultra-Corrosion-Resistant Stainless Steel (Alloy 20) | N08020 |
| | | Stainless Steel (Type 304) | S30400 |
| | | MONEL® Alloy K-500 | N05500 |
| | | INCONEL® Alloy 625 | N06625 |
| | Second kind | Titanium (Grade 2) | R50400 |
| | | Free-Cutting Brass (Alloy 360) | C36000 |
| | | High strength Bronze (Alloy 642) | C64200 |
| | | Aluminum (AL 2024) | A92024 |
| | | Aluminum (AL 6061) | A96061 |
| | | Beryllium copper (C17510) | C17510 |
| | | Phosphor Bronze (Alloy 510) | C51000 |
| | | Tellurium Copper (Alloy 145) | C14500 |

Table 2.2: Some properties of interest for the test samples

| Sample Material | Susceptibility | Modulus of Elasticity | Yield Strength |
|------------------------|----------------|-----------------------|----------------|
| | [ppm] | [GPa] | [MPa] |
| Copper 145 | -9.63 | 119 | 205 |
| Phosphor Bronze 510 | -5.86 | 111 | 342 |
| Beryllium copper 17510 | 4 | 138 | 210 |
| Aluminum 6061 | 19 | 69 | 275 |
| Aluminum 2024 | 19 | 73 | 290 |
| Bronze 642 | 100 | 115 | 310 |
| Brass 360 | 112* | 106 | 172 |
| Titanium Grade2 | 182 | 114 | 275 |
| Inconel 625 | 600 | 207 | 517 |
| Monel K-500 | 1100 | 180 | 790 |
| Stainless steel 304 | 3520 | 193 | 310 |
| Stainless steel 20 | 3520 | 190 | 241 |

* value suggested in this thesis and number sources [92-96]

2.4 Methods

2.4.1 Setup of the experiment

Fig. 2.2 show the experimental setup using the phantom for the image artifacts experiment which was performed in 3T MRI system (Siemens Tim Trio, software version VB17A). In image artifacts experiments were conducted using the whole-body RF transmit/receive coil only.

2.4.2 Samples orientations

To achieve consistent positioning and repeatability of results a plastic frame was fabricated and fitted on top of the phantom used in the experiment. The plastic frame consisted of adjustable clamps that have several degrees of freedom to position the samples accurately and consistently during the experiment as shown in Fig. 2.2.

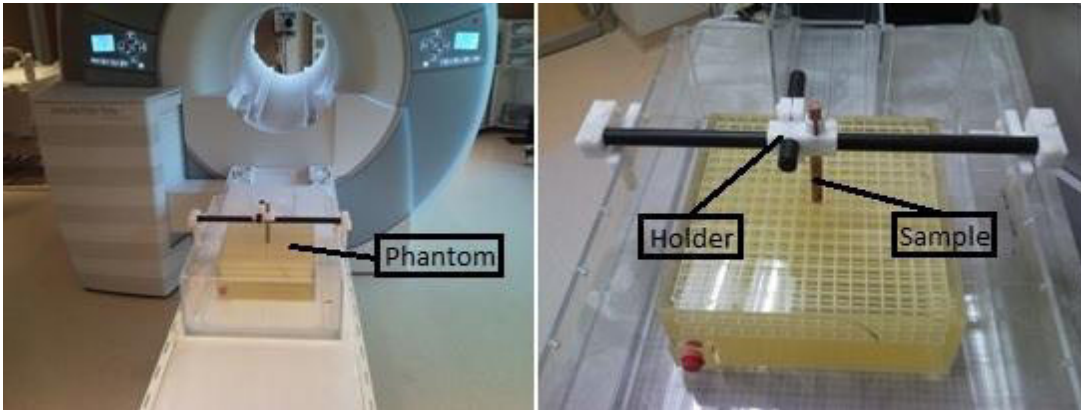


Fig 2.2: shows the setup configuration for the image distortion experiment and the small phantom.

2.4.3 Phantom design

For evaluation of image artifacts an enclosed phantom was fabricated with rectangular dimension (300 x 300 x 100 mm) to decrease the field of view (FOV) for better imaging results. The phantom was filled with canola oil to ensure the homogeneity of the magnetic field is not compromised and was fitted with equally spaced grids (10 x 10 mm grid size and spacing of 17.38 mm between grids) for positional references. Air bubbles were extracted manually from the enclosed volume to ensure that it will not add to the image distortion from these residual, refer to Fig. 2.2.

2.4.4 Assessment of magnetic field interaction

The samples were evaluated for induced transitional force, and torque was calculated using the 3T MRI system parameters and susceptibility

2.4.4.1 Translation forces induced in the sample

For translational attraction, the deflection angle was measured following the standard ASTM F 2052 – 06 [97] by using the fixture shown in Fig. 2.3 [Left]. Measurements of deflection angles for each device were obtained at the position in the scanner that produced the greatest magnetically induced deflection. For this particular 3T MR system, the highest spatial gradient occurs at a position that is 874mm \pm 0.5mm from isocenter

and the sample at 100 mm height from the base (magnetic spatial gradient 38 mT/m per axis and 200 μ s rise time).



Fig. 2.3: [Left] shows the test fixture used in performing the force measurement, [Right] the shape of the test samples used in the experiment.

2.4.4.2 Torque forces induced in the sample

Torque was qualitatively estimated for each device and for evaluation each device was placed in the scanner to be observed for alignment or rotation relative to the static magnetic field of the MR system while hand gripped and positioned inside the bore of the scanner. The following two state methods were applied:

- 1) No torque state: when the device showed no sensible change to align to the magnetic field.
- 2) Torque state: when the device slightly changed to align to the magnetic field.

These two states were only chosen as low torque value was anticipated due to susceptibility values of the tested samples.

2.4.5 Assessment of the image artifacts

Magnetic resonance imaging related artifacts for all samples tested in the 3T/128MHz MR System (Siemens Tim Trio, software version VB17A) using the whole-body RF transmit/receive coil only and using two pulse sequence and varying different parameters .

2.4.5.1 Imaging protocols parameters

Magnetic resonance imaging was performed using a transmit/receive RF whole-body coil for all samples to study different image distortion conditions. The position for landmark (i.e. the center position region for the MRI testing) was fixed for consistent repeatable results. The landmark positions were the center of the sample when placed in the middle of the phantom. Three different GE and TSE conditions were achieved by varying the TR, TE, and bandwidth parameters to investigate possible image artefacts in the test samples. Table 2.3 shows the pulse sequence parameters for image distortion used in the experiment.

Table 2.3: Pulse sequence parameters for image distortion used in the experiment

| Sequence ID | G270-4 | G810-4 | G810-8 | T40-30 | T250-9 | T751-8.8 |
|------------------------|-----------|-----------|-----------|-----------|-----------|-----------|
| Sequence Type | GE | GE | GE | TSE | TSE | TSE |
| TR (ms) | 200 | 200 | 200 | 4120 | 1270 | 1240 |
| TE (ms) | 4 | 4 | 8 | 30 | 9 | 8.8 |
| Flip angle (deg) | 60 | 60 | 60 | 180 | 180 | 180 |
| Field of view (mm) | 360 x360 | 360 x360 | 360 x360 | 360 x360 | 360 x360 | 360 x360 |
| Matrix size (px) | 512 x 512 | 512 x 512 | 512 x 512 | 512 x 512 | 512 x 512 | 512 x 512 |
| Section thickness (mm) | 4 | 4 | 4 | 4 | 4 | 4 |
| Bandwidth (Hz/Px) | 270 | 810 | 810 | 40 | 250 | 751 |
| Imaging plane | Coronal | Coronal | Coronal | Coronal | Coronal | Coronal |
| No. of slices | 16 | 16 | 16 | 16 | 16 | 16 |
| Imaging time (mm:ss) | 1:44 | 1:44 | 1:44 | 4:29 | 1:24 | 1:22 |

2.4.5.1 Assessment of signal dropout

Image signal drop out which is mainly evident in the low susceptibility samples when using the gradient echo (GE), pulse sequence was evaluated by subtracting the signal dropout in the image in question from the original distortion free image that was taken as a control at the beginning of the experiment. This image subtraction was carried out after the gray scale conversion of the image. The number of pixels affected was used as an

indication of the signal dropout area and the perimeter of this area was extracted to locate the position of the affected area.

2.4.5.2 Assessment of image distortion

Spatial distortion was the dominating effect in the spin echo (SE) pulse sequence in the low susceptibility sample. The distortions were evaluated by tracing the displaced lines of a grid and comparing it to the distortion free line grid before the sample is introduced. By accumulating the number of affected pixels along with the displacement value for each pixel of the affected displaced area was calculated and a number of the image distortion was extracted. For this case identifying the location for the distorted area was not as obvious as in the case of signal dropout due to the positional shift in the images.

2.4.6 Assessment of susceptibility related to force

There are forces and torques exerted on an object placed in a magnetic field, as a result it tends to move or rotate relative to this field. The value of induced forces and torques depends mainly on the strength of the magnetic field and the properties of the material of the object involved [11].

The dipole moment of an object can be represented as ($\mathbf{m} = M V$) if the magnetization (M) is uniformly distributed over the object of volume (V). Furthermore, when an object placed at a certain point in a magnetic field if the object with a permanent dipole moment (\mathbf{m}) it acquires an energy equal to $U = \mathbf{m} \cdot \mathbf{B}_0$, or if another object with magnetic dipole moment proportional to the strength of the applied field at the same point the acquired energy equal to $U = \frac{1}{2} \mathbf{m} \cdot \mathbf{B}_0$. It is clear from the previous equations that the strength of the dipole moment, the strength of the magnetic field (B_0) and the angle (θ) between these two vector quantities are the main factor for the acquired magnetic energy. This magnetic energy increases due to the exerted forces that attract the object towards the magnetic field and the torque that align (rotate) the \mathbf{m} with B_0 . The term for force was given in equation (2.1) and equation for the torque can be written as follows [11]:

$$T = \frac{\chi^2 V B_0^2}{\mu_0} (D_a - D_r) \cos\theta \sin\theta \quad (2.5)$$

Where T is the torque, D_a is the demagnetizing factor along the axis of symmetry and D_r is the demagnetizing factor along the equivalent radial axis.



Fig 2.4: [Left] shows the deflection of 0 deg. for copper, [Right] shows a deflection of 29 deg. for stainless steel.

2.5 Results

2.5.1 Translation force and torque in magnetic field

Maximum deflection angle was measured using the fixture shown in Fig. 2.4. The deflection was recorded for each sample and repeated 3 times as per the standard ASTM F 2052 – 06 [97] by using the setup shown in the picture. The sample was attached to the wire and the corresponding angle was obtained. The maximum deflection angle recorded was 28° for stainless steel (Alloy20) and the minimum was 0° for other samples with an error bar $\pm 1^\circ$ (refer to Table 2.4). The force was calculated using the following formula:

$$F = mg \tan \alpha \quad (2.6)$$

Where: m = mass of the sample

α = angular deflection of string measured with protractor

g = acceleration due to gravity

For the torque experiment, only a few samples showed a slightly tendency to align to the magnetic field, namely stainless steel (alloy 20) and stainless steel (Alloy 304). The rest of the samples showed no appreciable tendency to align to the magnetic field. The value of the calculated torque was approximately zero.

Table 2.4: The values of measured deflection angle and respective calculated force

| Sample Material | Deflection [deg.] | Density [kg/m ³] | Force [mN] | Susceptibility [ppm] |
|------------------------|----------------------|---------------------------------|---------------|-------------------------|
| Copper 145 | 0 | 8900 | 2 | 9.63 |
| Phosphor Bronze 510 | 0 | 8170 | 1 | -5.86 |
| Beryllium copper 17510 | 0 | 8200 | 1 | 4 |
| Aluminum 6061 | 0 | 2700 | 4 | 19 |
| Aluminum 2024 | 0 | 2700 | 4 | 19 |
| Bronze 642 | 0 | 8170 | 19 | 100 |
| Brass 360 | 1 | 8540 | 22 | 112 |
| Titanium Grade2 | 2 | 4420 | 35 | 182 |
| Inconel 625 | 4 | 8500 | 115 | 600 |
| Monel K-500 | 8 | 8830 | 211 | 1100 |
| Stainless steel 304 | 28 | 7750 | 676 | 3520 |
| Stainless steel 20 | 29 | 7750 | 676 | 3520 |

Numbers source [102].

2.5.2 Image Distortion

2.5.2.1 Signal dropout from the GE sequence

Signal dropout around the sample from the GE sequence is shown in Fig. 2.5 and 2.6, the maximum signal dropout was obtained from testing the stainless steel (Alloy20) sample and the minimum was obtained from different samples Brass 360, Aluminum, Bronze,

Titanium, and beryllium copper as they showed negligible signal dropout which was considered as zero signal dropouts. Table 2.5 presents dropout as a function of different parameters of the gradient echo pulse sequence (TE and bandwidth) and with an error bar of the distorted area as presented in the same table. The perimeter of the signal drop area was extracted for all samples that showed sufficient affected signal dropout area. This was performed to locate the position and extent of this defected area around the center of the field of view (FOV) for each material as shown in Fig. 2.7.

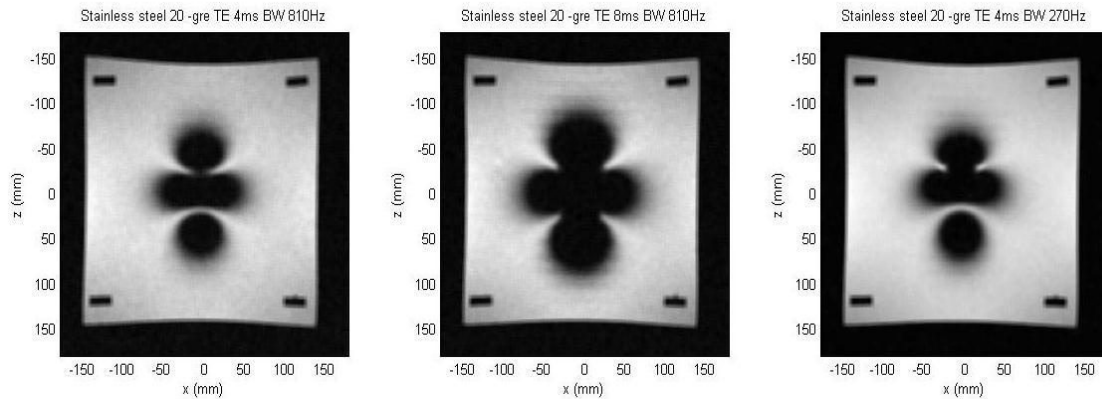


Fig. 2.5: shows max signal dropout for stainless steel 20 at different GRE sequence

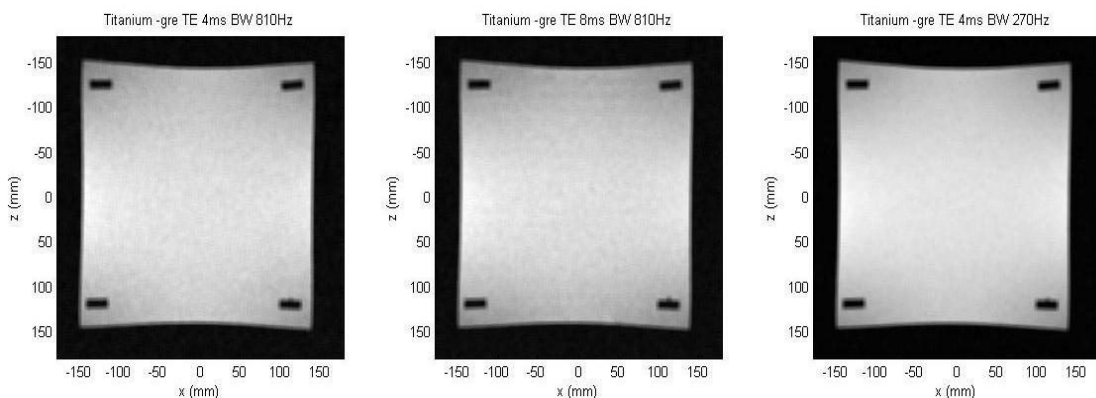


Fig. 2.6: shows min signal dropout for Titanium at different GRE sequence parameters.

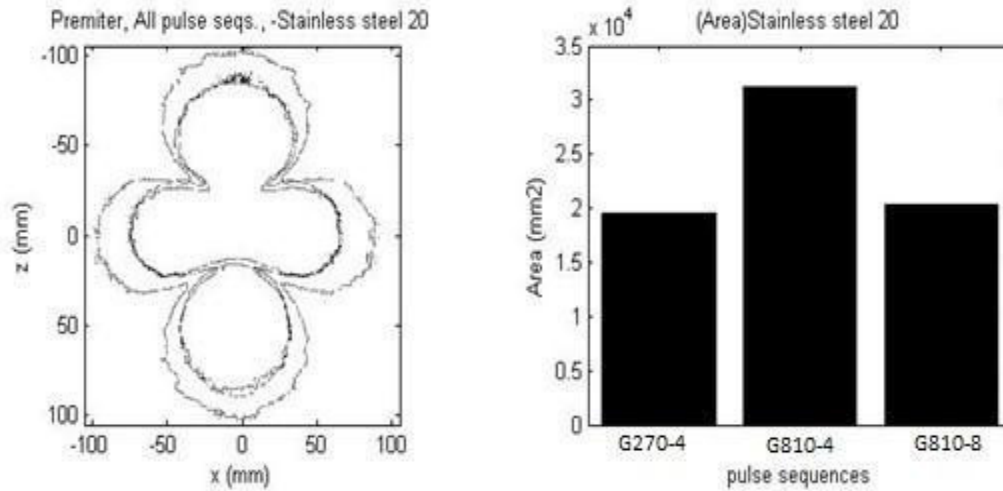


Fig. 2.7: shows the extracted perimeter for the signal dropout area of stainless steel 20 at the three different GRE sequence conditions (G270-4, G810-4 and G810-8 as presented in Table 2.3)

Table 2.5: Signal dropout of different materials for different GRE sequence

| Sample Material | GRE TE 4ms, BW 810 Hz | GRE TE 8ms, BW 810 Hz | GRE TE 4ms, BW 270 Hz |
|---|--------------------------|--------------------------|--------------------------|
| Signal dropout area (mm ²) | | | |
| | ±0.32% Error bar | ±0.93% Error bar | ±0.15% Error bar |
| Copper 145 | 158 | 144 | 9 |
| Beryllium copper 17510 | 162 | 143 | 11 |
| Phosphor Bronze 510 | 263 | 134 | 0 |
| Aluminum 6061 | 236 | 147 | 0 |
| Aluminum 2024 | 220 | 96 | 0 |
| Bronze 642 | 289 | 127 | 0 |
| Brass 360 | 633 | 1506 | 422 |
| Titanium Grade2 | 852 | 1887 | 628 |
| Inconel 625 | 2301 | 5282 | 1958 |
| Monel K-500 | 6872 | 12905 | 6753 |
| Stainless steel 304 | 17689 | 27871 | 18482 |
| Stainless steel 20 | 20938 | 30671 | 21200 |

2.5.2.2 Image distortion from the TSE sequence

Image distortion around the sample from the TSE sequence is shown in Fig. 2.8 and 2.9. The maximum distortion was obtained from the stainless steel (Alloy20) sample and the minimum was obtained from different samples brass 360, aluminum, bronze, titanium and beryllium copper as they showed negligible signal dropout. Table 2.6 presents image distortion values as a function of different parameters of the TSE pulse sequence (TE and bandwidth) and with an error bar of the distorted area in the same table.

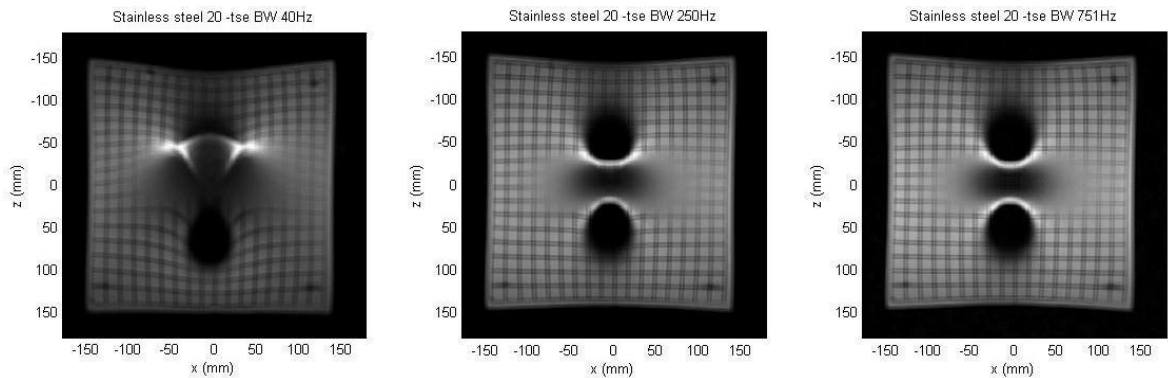


Fig 2.8: shows max image distortion for stainless steel 20 at different TSE sequence parameters.

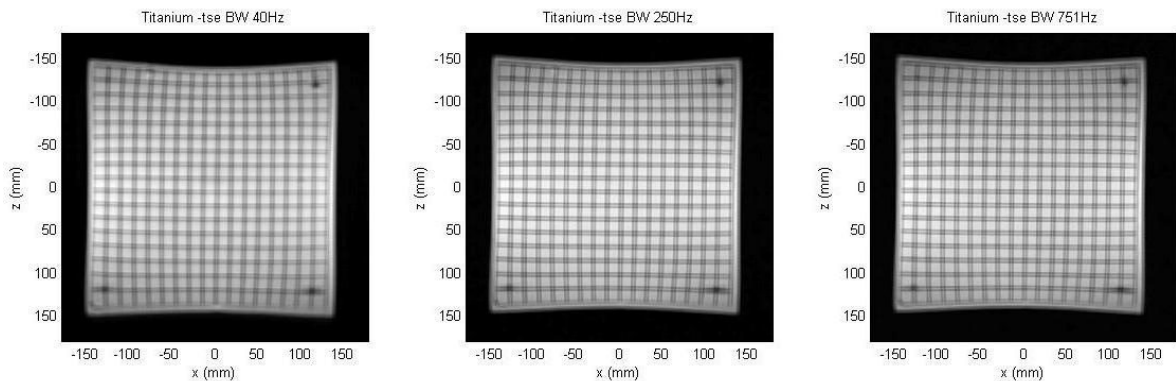


Fig 2.9: shows min image distortion for Titanium at different TSE sequence parameters.

Table 2.6: Image distortion values of different materials for different TSE sequence

| Sample Material | TSE BW 40 Hz | TSE BW 250 Hz | TSE BW751 Hz |
|------------------------|-------------------------------------|----------------|----------------|
| | Distortion Area (mm ²) | | |
| | ± 0.1 % Error | ± 0.09 % Error | ± 0.07 % Error |
| | bar | bar | bar |
| Copper 145 | 0 | 376 | 31 |
| Phosphor Bronze 510 | 0 | 323 | 64 |
| Beryllium copper 17510 | 0 | 170 | 31 |
| Aluminum 6061 | 0 | 368 | 62 |
| Aluminum 2024 | 0 | 178 | 38 |
| Bronze 642 | 1 | 441 | 39 |
| Brass 360 | 1355 | 402 | 34 |
| Titanium Grade2 | 2265 | 158 | 32 |
| Inconel 625 | 12541 | 750 | 50 |
| Monel K-500 | 29091 | 3259 | 1799 |
| Stainless steel 304 | 39544 | 14213 | 6275 |
| Stainless steel 20 | 40798 | 10073 | 9478 |

Perimeter of the image distorted area was not so obvious (as in signal dropout) to extract for samples but geometric shapes marking were used instead as shown in Fig. 2.10.

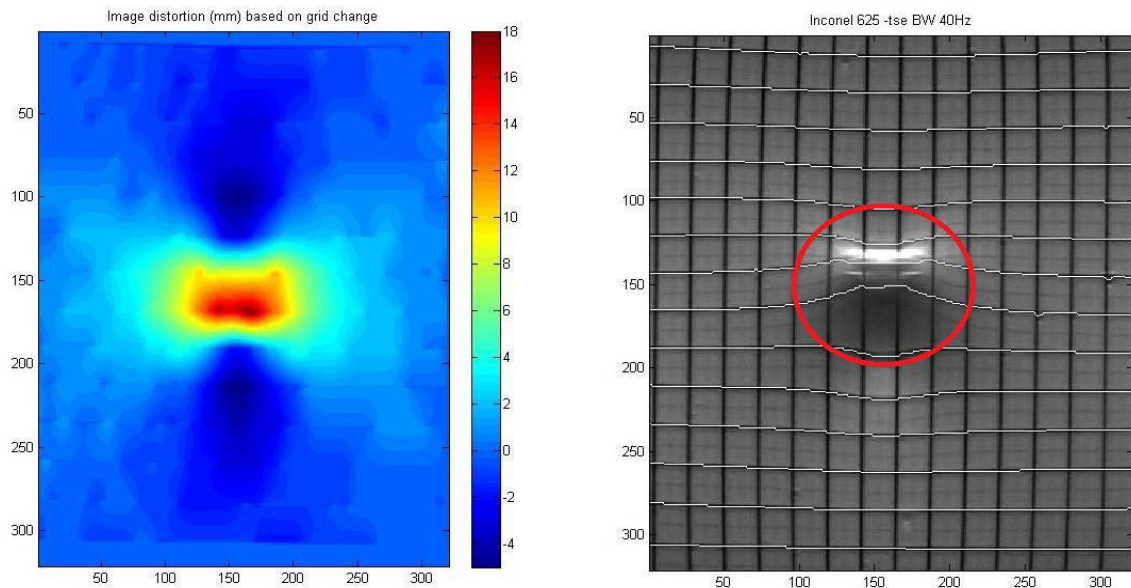
**Fig 2.10:** shows distortion area for Inconel and the line tracing algorithm used.

Table 2.7 lists the results for the force experiments along with the expected force based from equation (2.1). The scanner specification for the maximum B_0 , dBz/dz is 15 to 20 T²/m and the value of 15 T²/m was found to give the closest correlation to the experimental data.

In summary, image artifacts results can be divided into two types; signal dropout which is complete loss of signal resulting in a black area and spatial distortion where the image grid is still visible but the straight lines have been curved (in relation to low susceptibility samples). In GR the dominant artifact type is dropout (Fig. 2.4) where in TSE both types exist to varying degrees depending on the material and sequence parameters (Fig. 2.7). As described in the Methods section, image processing for dropout is straightforward but distortion requires the use of a custom line tracing program that calculates distance between the grid lines. An example of the program is shown in Fig. 2.9 is examples of materials showing no image artifacts. As a result of the complexity of automating image distortion area extraction manual methods were used to extract the data by means of geometric shape enclosing the affected area explained in the following section.

Table 2.7: Experimental and calculated sample forces

| Sample Material | Susceptibility | Deflection | Exp. Force | Calc. Force |
|-------------------------------|-----------------------|-------------------|-------------------|--------------------|
| | [ppm] | ±1° | [mN] | [mN] |
| Copper 145 | 9.63 | 0 | 0 | 2 |
| Phosphor Bronze 510 | -5.86 | 0 | 0 | 1 |
| Beryllium copper 17510 | 4 | 0 | 0 | 1 |
| Aluminum 6061 | 19 | 0 | 0 | 4 |
| Aluminum 2024 | 19 | 0 | 0 | 4 |
| Bronze 642 | 100 | 0 | 0 | 19 |
| Brass 360 | 112 | 1 | 24 | 22 |
| Titanium Grade2 | 182 | 2 | 24 | 35 |
| Inconel 625 | 600 | 4 | 94 | 115 |
| Monel K-500 | 1100 | 8 | 196 | 211 |
| Stainless steel 304 | 3520 | 28 | 650 | 676 |
| Stainless steel 20 | 3520 | 29 | 678 | 676 |

Table 2.8 lists the dimensions of a circle drawn around the image artifact as seen in the view plane. The calculated results using equation (2.4) are given in Table 2.9 which will be compared to the experimental results after extracting the circle radius manually. Note that the theory gives a symmetrical artifact region which can be described by a circle encompassing the artifact affected region whether it is signal dropout or image distortion. Also, the theory does not predict the penetration perpendicular to the view plane but this can be easily predicted knowing the slice thickness and distance between slices.

Table 2.8: Experimental image artifacts in view plane

| Sample Material | Experimental Region Circle Radius (mm) | | | | | |
|-------------------------------|--|--------|--------|--------|--------|----------|
| | G270-4 | G810-4 | G810-8 | T40-30 | T250-9 | T751-8.8 |
| Copper 145 | 0 | 0 | 0 | 0 | 0 | 0 |
| Phosphor Bronze 510 | 0 | 0 | 0 | 0 | 0 | 0 |
| Beryllium copper 17510 | 0 | 0 | 0 | 0 | 0 | 0 |
| Aluminum 6061 | 0 | 0 | 0 | 0 | 0 | 0 |
| Aluminum 2024 | 0 | 0 | 0 | 0 | 0 | 0 |
| Bronze 642 | 0 | 0 | 0 | 0 | 0 | 0 |
| Brass 360 | 15 | 15 | 25 | 25 | 12 | 12 |
| Titanium Grade2 | 15 | 15 | 25 | 40 | 10 | 10 |
| Inconel 625 | 40 | 40 | 50 | 60 | 25 | 20 |
| Monel K-500 | 65 | 65 | 75 | 110 | 47 | 43 |
| Stainless steel 304 | 77 | 75 | 94 | 125 | 80 | 75 |
| Stainless steel 20 | 80 | 80 | 100 | 150 | 90 | 80 |

2.6 Discussion

Deflection angles for the samples ranged from 0 to 29 degrees with an error bar of ± 1 . ASTM International recommends that if the device deflects less than 45° , then the magnetically induced deflection force is less than the force on the device due to gravity. This condition implies that the magnetically induced force is no greater than any risk

imposed by the Earth's gravitational field. All the tested samples pass the ASTM recommendations [97].

Forces from the measured deflection angle and also the forces calculated using equation (2.1) were plotted against the susceptibility as shown in Fig. 2.11. The experimental trend is linear as expected and the theory slightly over-predicts the force. It was mentioned previously that the value of susceptibility of brass 360 presented in Table 2.2 was modified from the value specified by [94].

Table 2.9: Calculated image artifacts in view plane

| Sample Material | Calculated Distortion Region Circle Radius (mm) | | | | | |
|-------------------------------|---|--------|--------|--------|--------|----------|
| | G270-4 | G810-4 | G810-8 | T40-30 | T250-9 | T751-8.8 |
| Copper 145 | 8 | 5 | 5 | 21 | 8 | 5 |
| Phosphor Bronze 510 | 6 | 4 | 4 | 16 | 7 | 4 |
| Beryllium copper 17510 | 5 | 3 | 3 | 13 | 5 | 3 |
| Aluminum 6061 | 11 | 7 | 7 | 29 | 12 | 7 |
| Aluminum 2024 | 11 | 7 | 7 | 30 | 12 | 7 |
| Bronze 642 | 26 | 15 | 15 | 67 | 27 | 16 |
| Brass 360 | 27 | 16 | 16 | 71 | 28 | 16 |
| Titanium Grade2 | 35 | 20 | 20 | 91 | 36 | 21 |
| Inconel 625 | 63 | 37 | 37 | 165 | 66 | 38 |
| Monel K-500 | 116 | 67 | 67 | 301 | 120 | 69 |
| Stainless steel 304 | 154 | 89 | 89 | 399 | 160 | 92 |
| Stainless steel 20 | 154 | 89 | 89 | 399 | 160 | 92 |

The stated value in [94] is 11200 ppm but when the value is changed to 112 ppm to be comparable to other copper alloys the data follows the linear trend. Note that the values for susceptibility and magnetic field gradient were not experimental measured but were taken from published data.

The experiments on image artifacts considered the effects of sequence type, bandwidth, TE and susceptibility. The data for all the sequences is plotted versus susceptibility in Fig. 2.12. The expected region radii from equation (2.4) are plotted also versus susceptibility in Fig. 2.13.

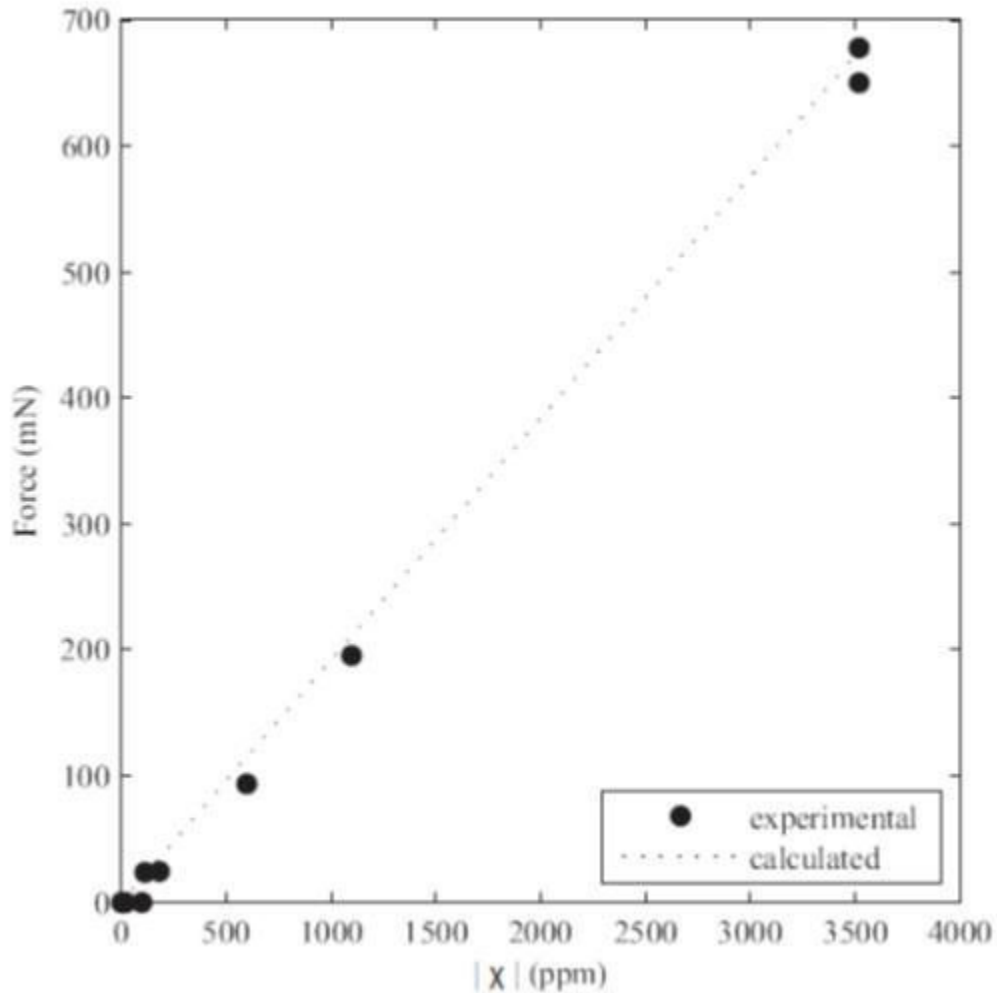


Fig.2.11: Experimental and calculated force versus susceptibility

Approximate dependence of distortion area on the various parameters was analyzed by considering sets of the data. All the data was used for the effect of susceptibility. Below 100 ppm there was no appreciable artifact. Above 100 ppm, the size of the artifact was

approximately proportional to $\chi^{0.5}$ as predicted by the theory. Analysis of the effect of bandwidth used G270-4 with G810-4 and T250-9 and T751-8.8. Both sets showed no apparent artifact size change over the range of susceptibility. This is counter to the theory which predicts $BW^{-0.5}$ dependence. Data from G810-4 and G810-8 showed the effect of TE on the artifact size.

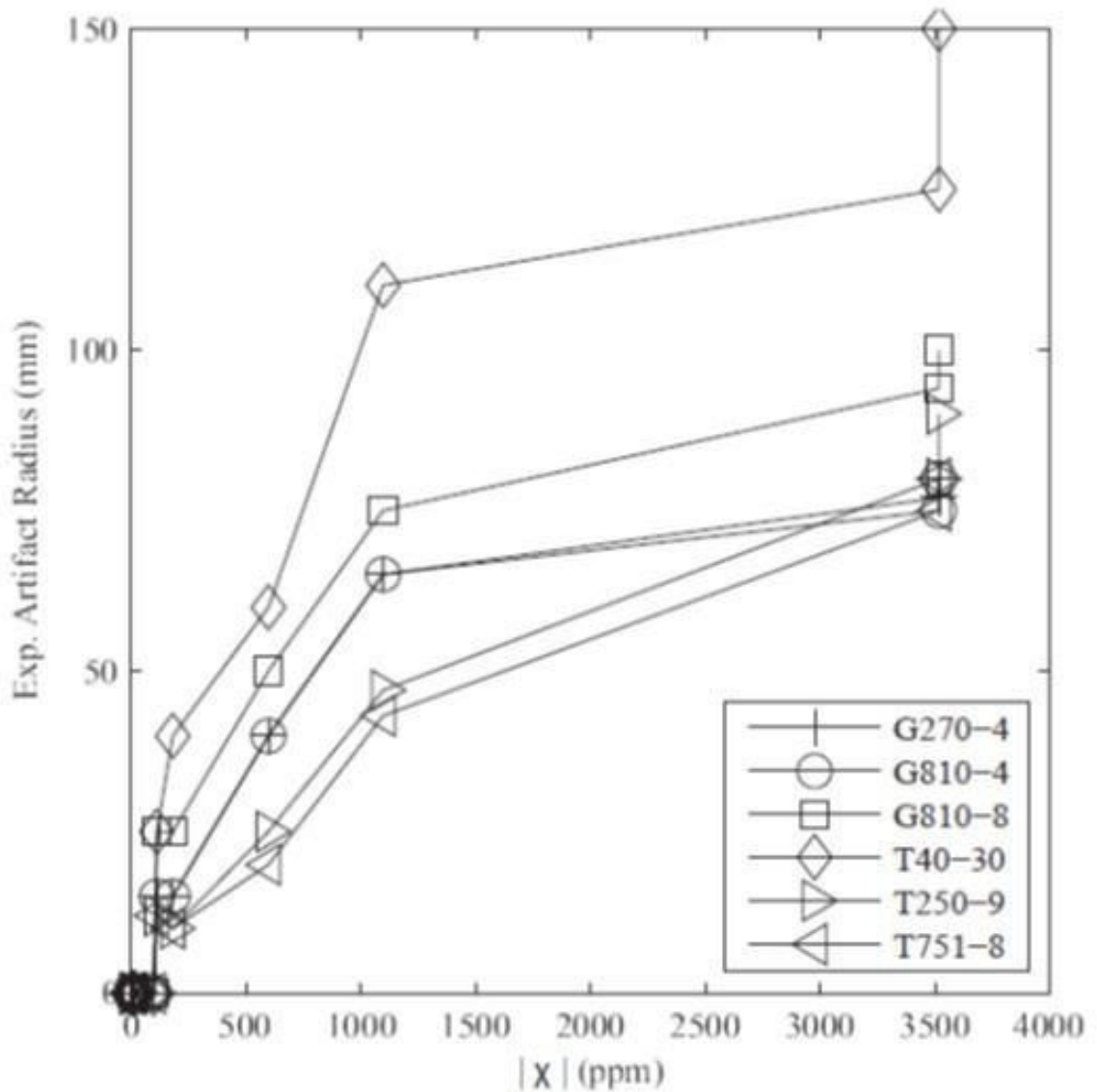


Fig. 2.12: Experimental artifact radius versus susceptibility

For the susceptibility values from 100-2000ppm, doubling the TE from 4 to 8 caused a constant delta of +10 mm for the radius. The delta for 3520 ppm was +19 mm. For the effect of scan type, G270-4 was compared to T250-9 and G810-8 was compared to T751-8.8. TSE shows an increase in artifact size compared to GE with the curves roughly parallel over the range of susceptibility.

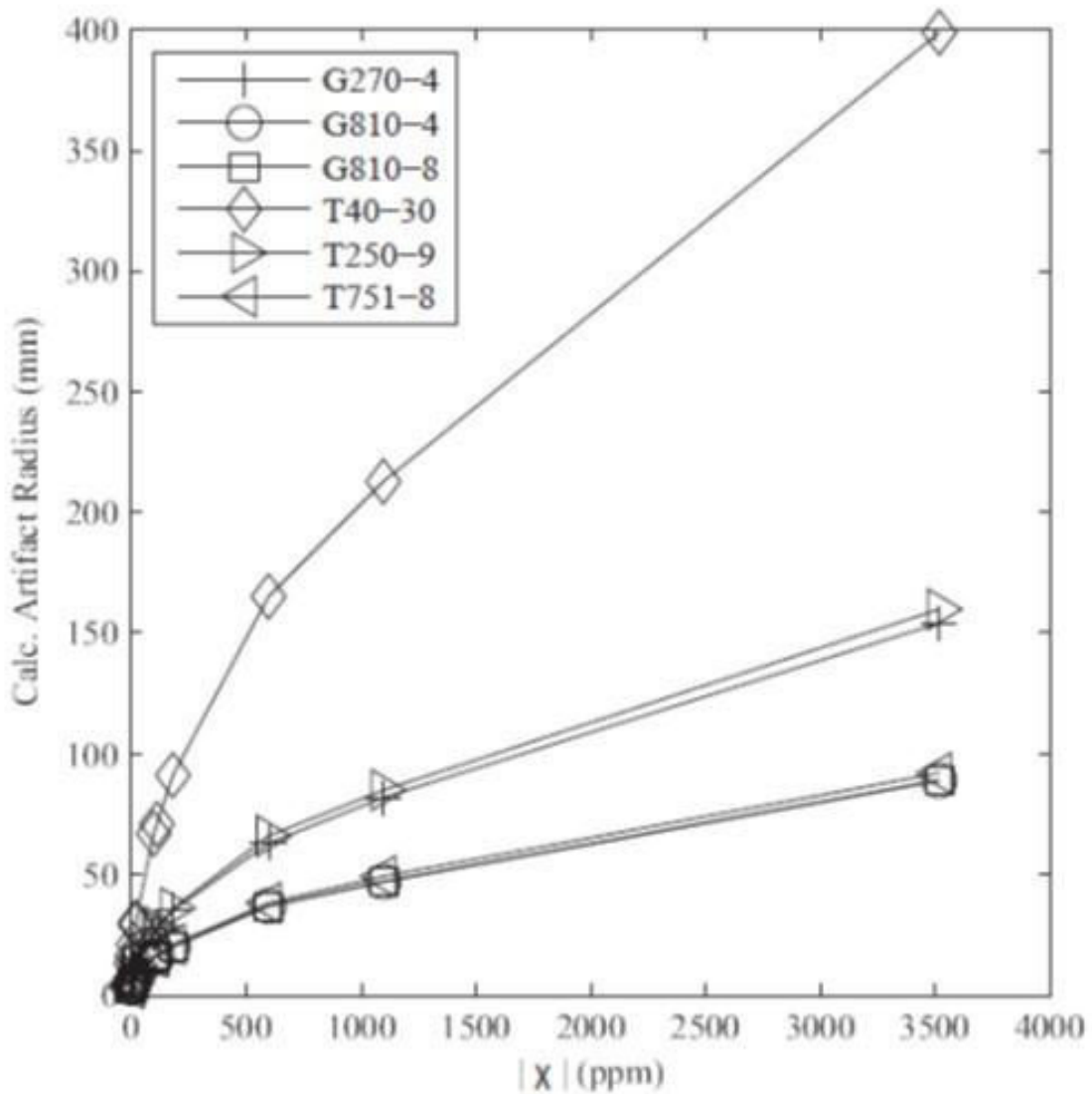


Fig. 2.13: Calculated artifact radius versus susceptibility

2.7 Conclusion

Data in the published literature is insufficient when choosing materials which possess sufficient strength and stiffness for MRI-compatible devices. Twelve candidate materials were selected and experimentally evaluated for induced force and image artifacts for a number of different scan profiles.

The results were compared to theoretical predictions based on equations available in the literature. As expected, the force varies linearly with susceptibility with good correlation with the theoretical predictions except for brass 360. It is believed the susceptibility for brass 360 in the referenced source [94] was mistakenly recorded and our results suggest a value of 112 ppm is more appropriate.

The susceptibility for the samples was not separately experimentally verified and is the most probable source of error. The image artifacts were compared based on the radius of the affected area in the image. It was observed that there is no one answers to the question of how far should the stainless steel rod be away from the imaging region. It depends on the scan sequence and the distance ranged from 8 cm to 15 cm.

The theory greatly over predicts the affected area however the trends in terms of susceptibility seem fairly accurate. The size of the artifact increases with susceptibility, TE and the use of TSE over GR. However the experimental data contradicted the theory by showing no appreciable effect due to bandwidth. In the future, work will be conducted to quantitatively examine the size and shape effect on image distortion as well as induced vibration. Data from testing was categorized according to the least obtained image distortion results and was related to the material's mechanical properties of the samples. This step was done to aid in choosing a suitable MR-compatible material to be used in fabricating the actuator. There was no appreciable heating was measured in the samples in this study but the next chapter will present the experiments carried out to identify the thermal effects induced in the samples when present in the MR environment.

Chapter 3

Induced Heat in MR-Environment Due to Time Varying Gradient Field

3.1 Introduction

Time-varying magnetic fields are also present in MRI, and are of two types. The radiofrequency system (primarily the transmit RF system) produces magnetic fields of several μT which oscillate at many MHz (the exact frequency being directly dependent on the main magnetic field). The gradient system produces magnetic fields that are typically several μT , and are switched at frequencies in the vicinity of 1 kHz. For a conducting material, the effect of both of these time varying magnetic fields will be heating of the object. Depending on the degree of heating, this can cause injury to the patient, degradation of the device's performance, or device failure. While there are many studies on estimating RF heating [98-104], there have been relatively few for predicting gradient [105-107] heating.

3.2 Background and theory

3.2.1 Radio frequency heating

Some of the RF heating reported in literature for surgical instruments [90], for metallic implants immersed in a gel solution simulating clinical methods [108], in guide wires used in medical procedures, or along long metallic wires in partially/completely dipped in gel solutions [9,103]. Maxwell's theory of electromagnetism differentiates between three mechanisms by which heating can be evoked by RF radiation as explained in [9].

1. Heating from eddy currents. These eddy currents are produced by RF radiation in each volume of conducting material, even small volumes.
2. Heating from induction loops. These situations may occur for example when using electrocardiographic/electroencephalographic leads.
3. Heating by resonating RF waves along conductors. If such a resonance occurs, the incident RF wave is bounced back at the endpoints of the wire-like structure, causing the reflected RF waves to travel back and forth along the longitudinal axis of this structure, in such a way that standing RF waves are formed.

In this work, the samples tested do not involve any looping, slender wires, and the lengths of the samples were intentionally to be out of the resonance frequency of the scanner RF field. This experiment for RF induced heating was conducted only for completeness of the overview for heat induction inside MRI environment.

3.2.2 Gradient heating

A detailed development of models for induction heating is given in [109] which are for the manufacturing process used in industry. It uses a coil driven by an AC signal to heat a component for heat treatment or brazing. The analysis of the induced heating of a component is a coupled problem of an AC field with a thermal field. While the signals in a gradient coils are not simply sinusoidal, for the purposes of heating analysis we will base

the analysis on the largest frequency component in the signal. This chapter focuses on the determination of the amount of power deposited by the coils into the component. This depends on the geometry and the material properties of the component. The analysis has been developed in [109] for the following geometries: thick (semi-infinite) slab, wide rectangular finite slab, solid cylinder, hollow cylinder, and thin hollow cylinder.

The analysis makes extensive reference to the skin depth, δ , which is the depth of penetration of the AC signal from the surface of the component. It is given by equation (3.1) where ρ is the resistivity μ_o is the permeability in free space, and f which is the frequency of the AC signal. Note that μ_o is employed instead of μ since only nonmagnetic materials were considered in this study.

$$\delta = \sqrt{\frac{\rho}{\mu_o \pi f}} \quad (3.1)$$

The first configuration is a thick, infinitely long rectangular slab with the field H_o parallel to its surface [10, 109]. The power deposited per square meter, P , is given by:

$$P = \frac{\rho}{\delta} H_o^2 = \sqrt{\rho \mu_o \pi f} H_o^2 \quad (3.2)$$

This is useful for components which are considerably thicker than the skin depth such that the electromagnetic fields on opposite surfaces of the component do not interact. In this configuration, the amount of power deposited increases monotonically with an increase in the material resistivity.

The next configuration considered in [10, 109] is a rectangular slab of finite width, b , such that the induced fields from both edges interacts. The power deposited is:

$$P = V\mu_0\pi f H_o^2 p \quad (3.3)$$

Where V is the total volume of the slab and p is a scaling factor dependent on the ratio of b/δ . The scale factor p is given by the following equation and shown in Fig. 3.1:

$$p = \frac{\delta}{b} \left[\frac{\sinh(b/\rho) - \sin(b/\rho)}{\cosh(b/\rho) - \cos(b/\rho)} \right] \quad (3.4)$$

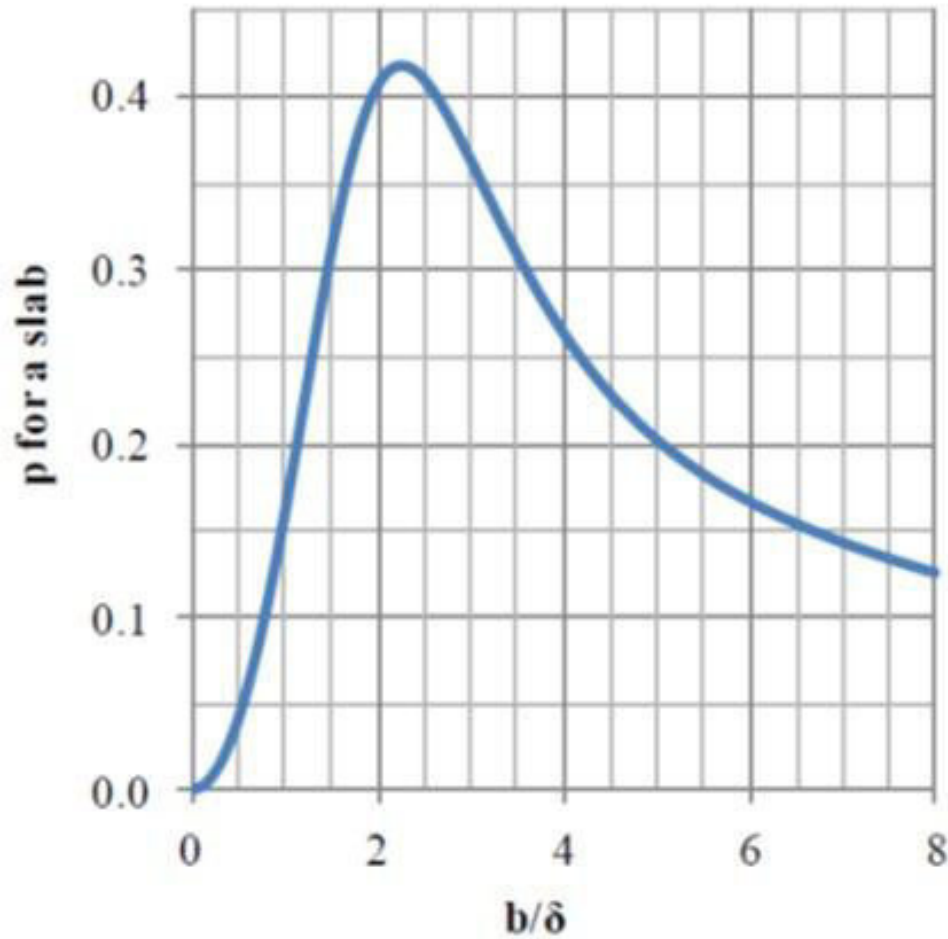


Fig.3.1: scaling factor for a rectangle slab of finite width

We see that there is a peak in the parameter p which means that materials with high resistivity (small b/δ ratio) can behave like materials with low resistivity. One should select a material such that its b/δ ratio is away from the 2.3 to limit the amount of heating. In [10], experiments were conducted to validate the equation.

A similar result is obtained for a cylindrical specimen of diameter d with its axis parallel to the magnetic field direction [8, 10, 109-110]. Equation (3.3) still holds however the values for p are based on complex Bessel functions (Kelvin functions) as shown below and graphed in Fig. 3.2.

$$p = 2\sqrt{2} \frac{\delta}{d} \frac{\text{ber}' \frac{d}{\sqrt{2}\delta} \text{ber} \frac{d}{\sqrt{2}\delta} - \text{ber} \frac{d}{\sqrt{2}\delta} \text{bei}' \frac{d}{\sqrt{2}\delta}}{\text{ber}^2 \frac{d}{\sqrt{2}\delta} \text{bei}^2 \frac{d}{\sqrt{2}\delta}} \quad (3.5)$$

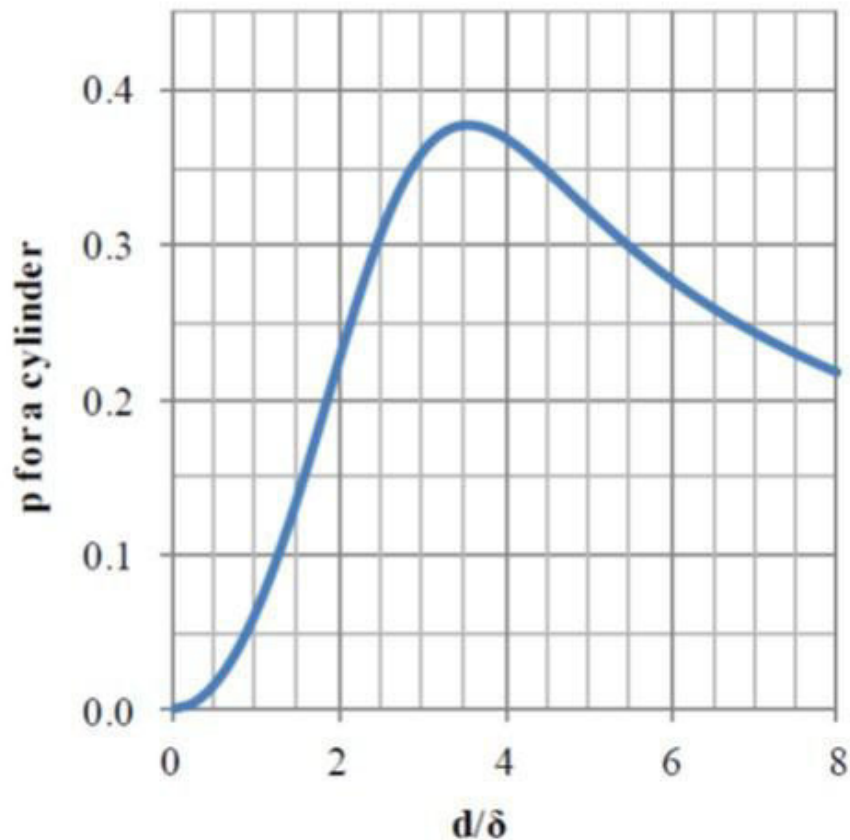


Fig. 3.2: scaling factor for cylinder of infinite length

The critical ratio of d/δ is at approximately 3.5 instead of 2.3 but the same conclusions are as before regarding the resistivity of the specimen material. In [110], a linear relationship for the scale factor was presented for ratios much larger or much smaller than the critical value. It was noted that in [109] for ratios greater than 8 that p could be determined by:

$$p = \frac{2}{1.23 + d/\delta} \quad (3.6)$$

In the models of [109] and [110], the cylinder is considered to be so long that the end effects are negligible. Simulation of eddy currents in finite length cylinders was undertaken in [111] but it used Fourier series equations coupled by an inductive network which must be solved numerically and so the technique is not useful for design and material selection.

3.3 Materials and methods

3.3.1 Phantom design

The evaluation of RF related heating for the tested samples involved the use of a plastic phantom designed to approximate the dimensions and proportions of the head and torso of a human body, as described in the standard ASTM F 2182 – 09 [112]. The dimension of the larger part was a rectangle of length 65 cm and width of 42 cm, the smaller rectangular part had a dimension of 27 cm for length and 15 cm for width. A plastic frame with adjustable posts was placed at the top of the phantom to permit consistent positioning of the samples. The phantom was filled with of gel solution to simulate the human body for SARs calculations. A grid of 10 x 10 mm was placed submerged in the gel solution to facilitate in positioning the temperature probes as shown in Fig. 3.3.

3.3.2 Radio frequency heating

Samples tested for RF heating were placed in orientation parallel and perpendicular to the Z axis to distinguish the orientation of the extreme induced heat. This test was done in a qualitative matter as most literature indicates only rise in temperature related to fluid immersed samples.

3.3.2.1 Setup of the experiment

Fig. 3.3 show the experimental for the MRI-related RF heating experiment performed in 3T MRI system (Siemens Tim Trio, software version VB17A). The setup includes a phantom simulating a human torso. The figure shows the sample mounting clamps setup and the experiment was conducted using the whole-body RF transmit/receive coil only.

3.3.2.2 Samples orientation

To achieve consistent positioning and repeatability of results a plastic frame was fabricated and fitted on top of the phantom used in the experiment. The plastic frame consisted of adjustable posts/ clamps to felicitate max degrees of freedom in positioning the samples accurately and consistently as shown in Fig. 3.3.

3.3.2.3 RF heating sample positioning and orientation

In RF heating experiment samples were positioned in the middle of the holder (isocenter of the magnet). The sample was placed perpendicular to the Z axis and one end was located an inches above the surface of the gel in order decouple the sample electrically. A more severe position for the samples was tested (only for copper sample, as it was anticipated to have the maximum temperature rise) where the sample was placed at one end of the phantom holder closer to the machine whole-body coil and was oriented parallel to the Z axis away from the gel to avoid any electrical coupling.

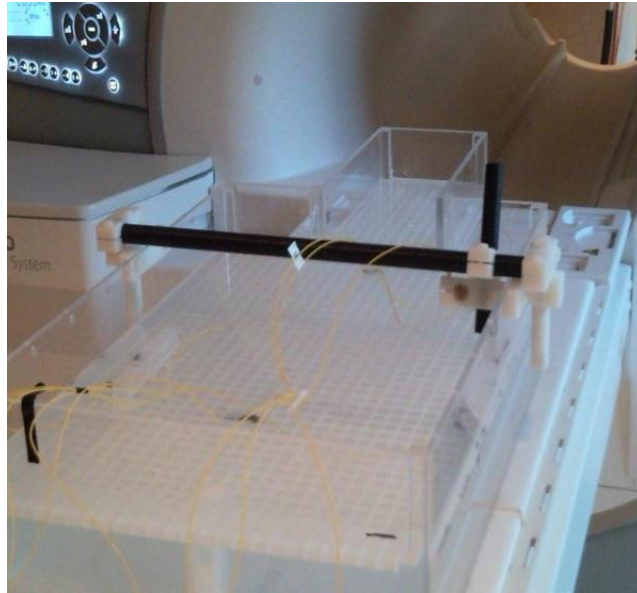


Fig. 3.3: shows the setup configuration for the RF heating experiment.

3.3.2.4 Thermometry system for RF heating experiments

Temperature recordings were obtained using an MR-compatible Neoptix fiber-optic temperature monitoring system. Probes were positioned to record the rise in temperature that would generate the greatest heating during the experiment. Seven probes were used and placed as follows:

- Probe 2, was placed immersed in the gel in the neck area of the phantom.
- Probe 1, 3, and 4 were placed immersed in the gel in the torso area of the phantom.
- Probe 5, was placed in direct contact with the top of the sample.
- Probe 8, was placed in direct contact with the middle of the sample.
- Probe 7, was placed in direct contact with the end of the sample.

All the probes connections directly contacting the sample were connected through conductive paste.

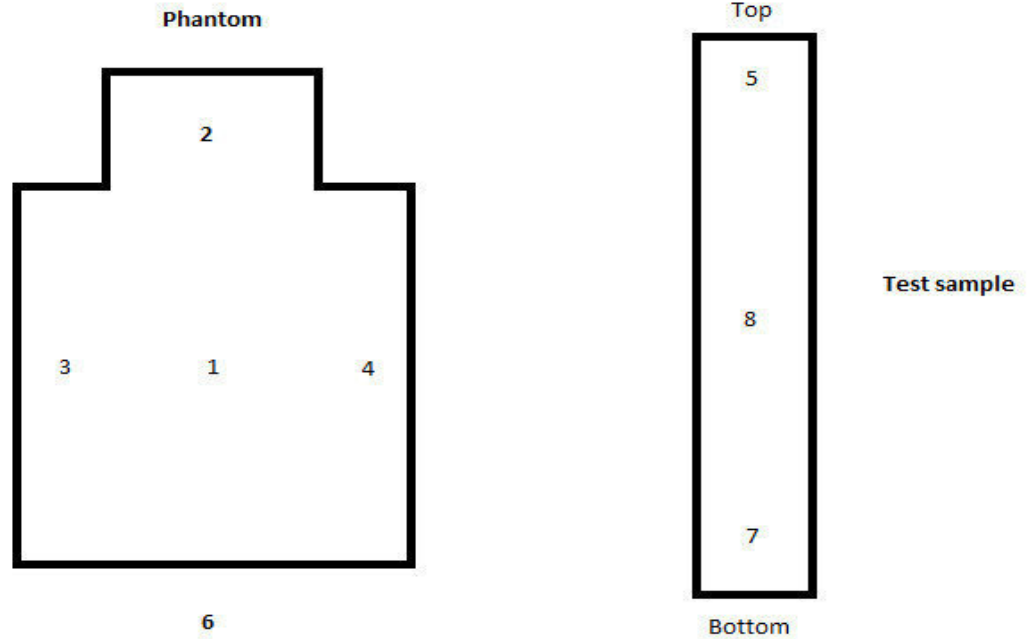


Fig.3.4: shows the positioning of the temperature sensing probes on the sample and the phantom for the RF exposure experiment.

In all cases, a probe (probe 6) was positioned within small distance from the back edge of the bottom torso portion of the phantom to record the ambient temperature. Fig. 3.3 shows the fiber optic sensors of the thermometry system used for the RF heating exposure experiments. Also refer to Fig. 3.4 for the placement of the temperature sensor in the phantom.

3.3.2.5 RF heating protocol and sequences

Induced heating experiment was performed using a transmit/receive whole-body RF coil in for each sample. To study different RF exposure conditions, the position for the samples were varied between parallel to the Z axis and perpendicular to it. Also the samples were positioned either with a small gap away from the gel solution or touching the gel. The only pulse sequence used for this experiment was TSE with TR 1400ms, TE 11ms, Slice thickness 10 mm, matrix size 256*256, FOV 480*480 mm, flip angle 180 deg., bandwidth 130 Hz/pixel, number of slices 12 slice and total scan time of 16 minutes.

3.3.3 Gradient heating

In the previous literature, the magnetic field was parallel to the axis of the cylinder. In this work perpendicularity of the cylinder to the magnetic field was considered. Rather than trying to solve for this condition analytically, finite element analysis (FEA) was used employing the software COMSOL [113]. For all the FEA studies, the conductivity of the rod was set at 5×10^7 S/m and the frequency of excitation was varied to achieve fourteen d/δ ratios in the range from 0.25 to 10. For each point, the software calculated the power deposited in the rod. Then the scaling factor, p , was determined [100]. Initially a two-dimensional (2D) analysis of 2976 triangular elements with the magnetic field parallel to the axis of the infinitely-long cylinder was conducted to validate the model. Then a 2D axisymmetric analysis of 32320 elements with the same field orientation but with a finite cylinder surrounded by an air box (radius 0.1 m and length 0.3m) was analyzed to quantify the effect of having a finite length. The cylinder's length to diameter ratio was 10. The next model with 24480 elements was again a 2D study but with the applied magnetic field perpendicular to the axis of an infinitely long cylinder inside an air box (0.2m by 0.2 m). Lastly, a 3D study with 42248 elements was undertaken to quantify the finite length effect on heating for this field orientation with a quarter model of the rod in an air box (radius 0.1m and length 0.2m).

3.3.3.1 Experimental setup and test materials

To investigate the validity of the FEA results, twelve rods of different materials were tested (see Table 3.1 for the materials and their properties). Measurement of the power deposited was not practical so instead the rate of the temperature change was used. If the heat loss can be considered negligible over the time frame considered, then the temperature will increase linearly as described by equation (3.7) where ρ_d is the mass density, V is the volume and c is the specific heat capacity of the material [109].

$$\dot{T} = \frac{P}{\rho_d c V} \quad (3.7)$$

The samples were each 12.7 mm in diameter and 127 mm long. The samples were positioned in the middle of the bore of the bench top electromagnet. The sample was placed perpendicular to the Z axis and insulated in polystyrene for accurate recording of temperature as was done in [10] and [8]. The experiment setup is shown in Fig. 3.5.



Fig. 3.5: shows the setup configuration for the gradient heating experiment with the lab magnet [left], the amplifier and acquisition system [right].

3.3.3.2 Gradient heating protocol parameters

A driving sinusoidal wave form of amplitude of 2 volts and switching frequency of 1 kHz was used as an input to drive a current amplifier to produce a gradient switching simulation of the MRI scanner in the lab magnet of around 22 T/s which was used in performing the gradient heat experiments

3.3.3.3 Thermometry system and probes placement

Temperature recordings were obtained using a nonmagnetic, MR-compatible thermocouple system (Sa1-E thermocouples from Omega) read out using a National Instruments SCXI 1303 device.

The probes were positioned to record the rise in temperature as follows:

- Probe 1, placed in direct contact with the end of the sample
- Probe 2, placed in the polystyrene insulation
- Probe 3, placed in direct contact with the middle of the sample

The magnetic field was provided using a water-cooled solenoid of 12 axial windings and 6 radial windings of 5 mm square hollow copper wire wound with an inner diameter of 15 cm. A National Instruments PXI 5401 was used to create a 1 kHz sinusoidal waveform as an input to a AE Techron 7796 linear amplifier to drive a peak current of 7.2 A through the coil producing an alternating magnetic field with peak amplitude of 2787 A/m, corresponding to a peak magnetic flux density of 3.50 mT. The maximum dB/dt value was 22 T/s. In comparison, the peak dB/dt values within the bore of a typical MRI system will be between 40 and 100 T/s (the higher value can occur outside the imaging region if multiple gradient axes are driven simultaneously at maximum strength). For reference, 22 T/s is approximately the dB/dt value one would estimate to be present near the edge of the imaging field of view when the gradient slew rate is 88 T/m/s (assuming a 50 cm field of view, peak gradient strength of 40 mT/m, a gradient rise time of 250 μ s, and considering only the z-component of magnetic field).

During the experiment, the sample was allowed sufficient time for stabilization to achieve equilibrium with the ambient temperature before the temperature was recorded. After a baseline temperature was logged for 5 minutes, the electromagnet was activated for 5 minutes with temperatures being recorded every 1 second. The electromagnet was then turned off and the temperature was recorded for an extra 5 minutes.

3.4 Results

3.4.1 Radio frequency heating

For RF heating experiment the phantom was filled with a gelled saline solution and was allowed enough time for stabilization to achieve equilibrium with the ambient temperature before the temperature recording was carried out. After a baseline temperature was logged

for 16 minutes, the MRI scan time recorded was 16:45 minutes for RF heating with temperatures logging every 1 second. After temperature rise logging ended another period of logging commenced for another 16 minutes to stabilize. No processing of the data was carried out as no temperature rise was detected.

Table 3.1: Material Properties.

| Material | ρ ($\Omega.m$) | ρ_d (kg/m^3) | c ($J/kg.^{\circ}C$) |
|--|--|--|---|
| Inconel (Alloy 625) | 1.29E-06 | 8440 | 410 |
| Stainless steel (Alloy20) | 1.08E-06 | 8000 | 500 |
| Stainless steel (Alloy 304) | 7.20E-07 | 8000 | 500 |
| Monel (Alloy K-500) | 6.15E-07 | 8440 | 419 |
| Titanium (grade2) | 5.20E-07 | 4510 | 523 |
| Bronze (Alloy 642) | 1.88E-07 | 7890 | 380 |
| Phosphor Bronze (Alloy 510) | 8.70E-08 | 8860 | 380 |
| Brass (Alloy 360) | 6.60E-08 | 8490 | 380 |
| Aluminum (Alloy 2024) | 5.80E-08 | 2780 | 875 |
| Aluminum (Alloy 6061) | 4.00E-08 | 2700 | 896 |
| Beryllium Copper (17510) | 3.80E-08 | 8830 | 418 |
| Copper (Alloy 145) | 1.90E-08 | 8940 | 385 |

3.4.2 Gradient heating

The total magnetic field distribution is plotted in Fig. 3.6 to 3.9 for the d/δ ratio of 3.55. The results of the FEA studies are shown in Fig. 3.10 with the scale factor plotted versus the d/δ ratio. The theoretical value for the scale factor calculated from equation (3.5) is also plotted for comparison. It can be seen that the FEA case corresponding to the theory matches it exactly. Changing the field orientation from parallel to the cylinder axis to perpendicular to the axis resulted in the scale factor being exactly doubled at each d/δ ratio. The effect of having a finite cylinder rather than the infinite model showed only a small departure in the scale factor. A typical observed heating curve is shown in Fig. 3.11 for aluminum 2024 and Inconel. It can be seen that the heating profile is approximately linear so the assumption for equation 7 is valid. The results of the tests are shown in Table 3.2 with the temperature rise over 300 seconds tabulated.

The theoretical temperature rise for each material was calculated based on its properties in Table 3.1 and equations (3.3) and (3.7) with the scale factor determined from equation (3.5) multiplied by 2 as suggested by our earlier FEA results. A 3D FEA study was also completed which employed a model of the actual coil used in the experiments. This was to assess any the effects of a finite coil as compared to the infinite coils used in the earlier FEA studies.

The experimental, theoretical and FEA temperature rises are plotted in Fig. 3.12. The FEA and experiment show a good match especially for lower values of the d/δ ratio

3.5 Discussion

The FEA studies in this work showed a surprising result in that the theoretically determined scale factor for cylinders simply doubled when the magnetic field was oriented perpendicular to the cylinder axis. This was particularly surprising since the total magnetic field distributions (Fig. 3.6 and 3.8) are very different. The experimental results confirmed this relationship especially when the FEA study was adapted to model the actual experimental coil.

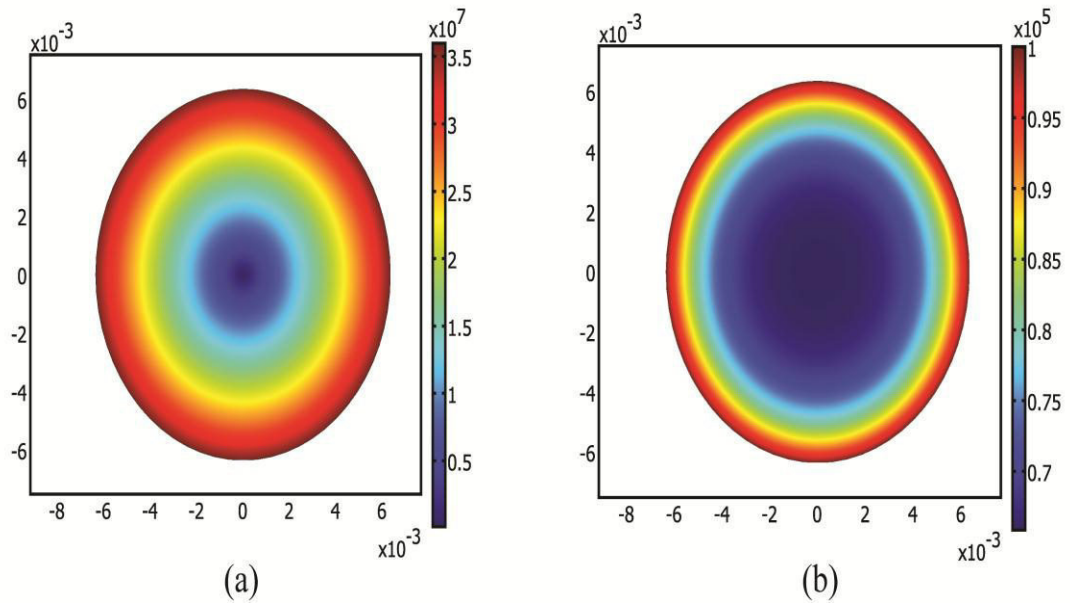


Fig 3.6: The a) current density (A/m^2) and b) magnetic field (A/m) for a 2D finite element analysis model with the magnetic field applied parallel to the cylinder's axis.

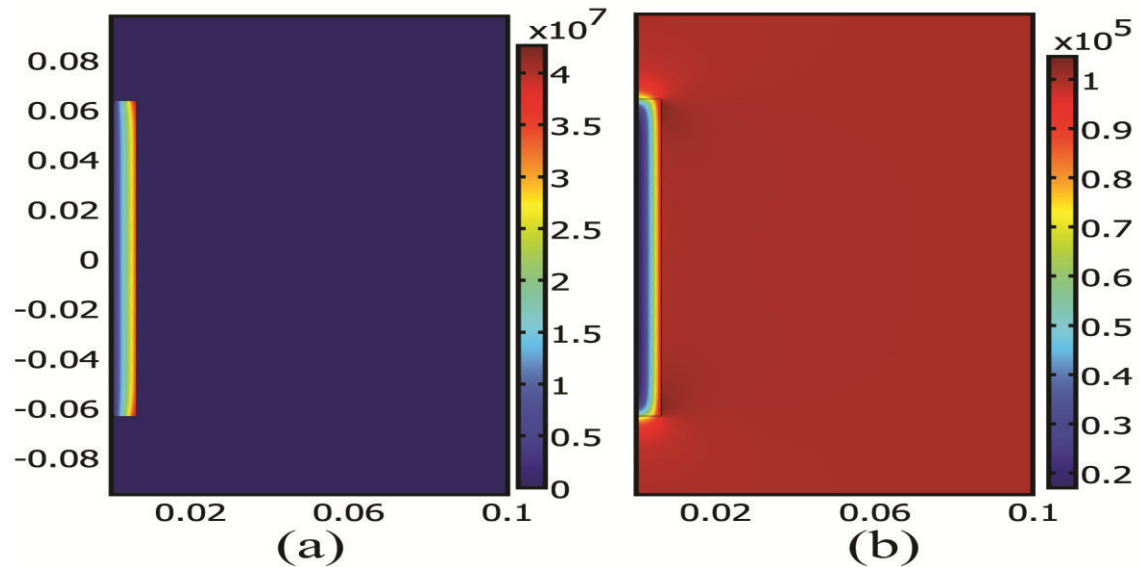


Fig. 3.7: The a) current density (A/m^2) and b) magnetic field (A/m) for a 2D axisymmetric finite element analysis model with the magnetic field applied parallel to the cylinder's axis with a cylinder of finite length.

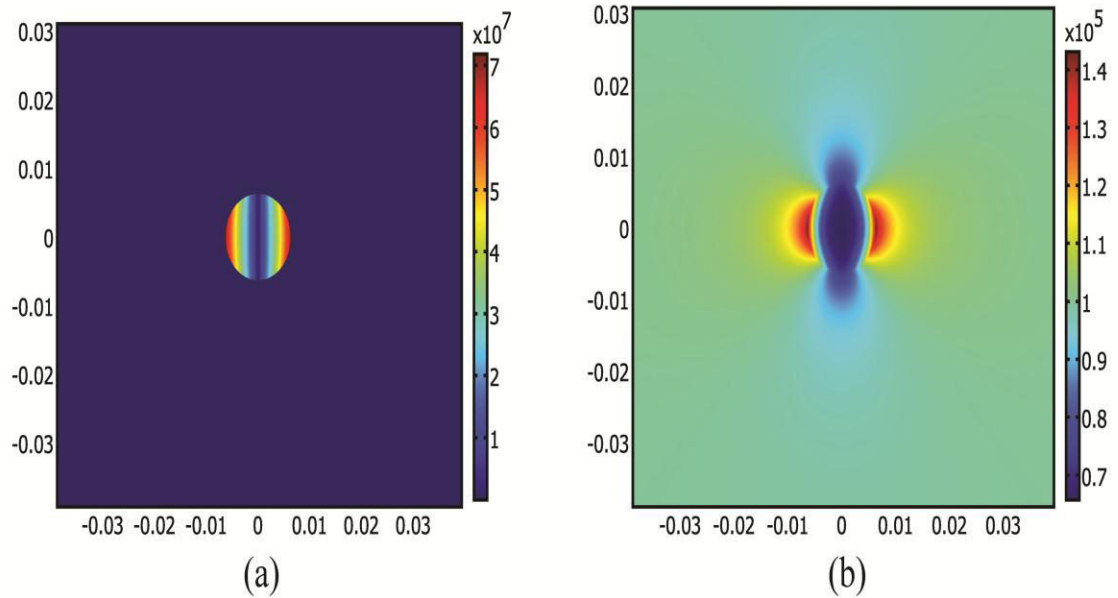
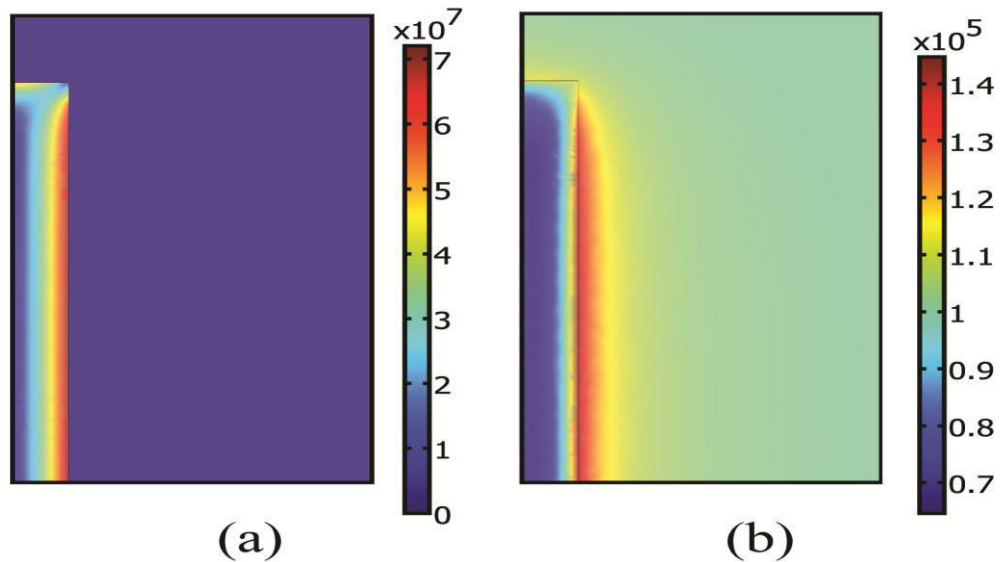


Fig. 3.8: The a) current density (A/m²) and b) magnetic field (A/m) for a 2D finite element analysis model with the magnetic field applied perpendicular to the cylinder's axis.



2 Fig. 3.9: The a) current density (A/m²) and b) magnetic field (A/m) for a 3D finite element analysis quarter-model with the magnetic field applied perpendicular to the cylinder's axis with a cylinder of finite length.

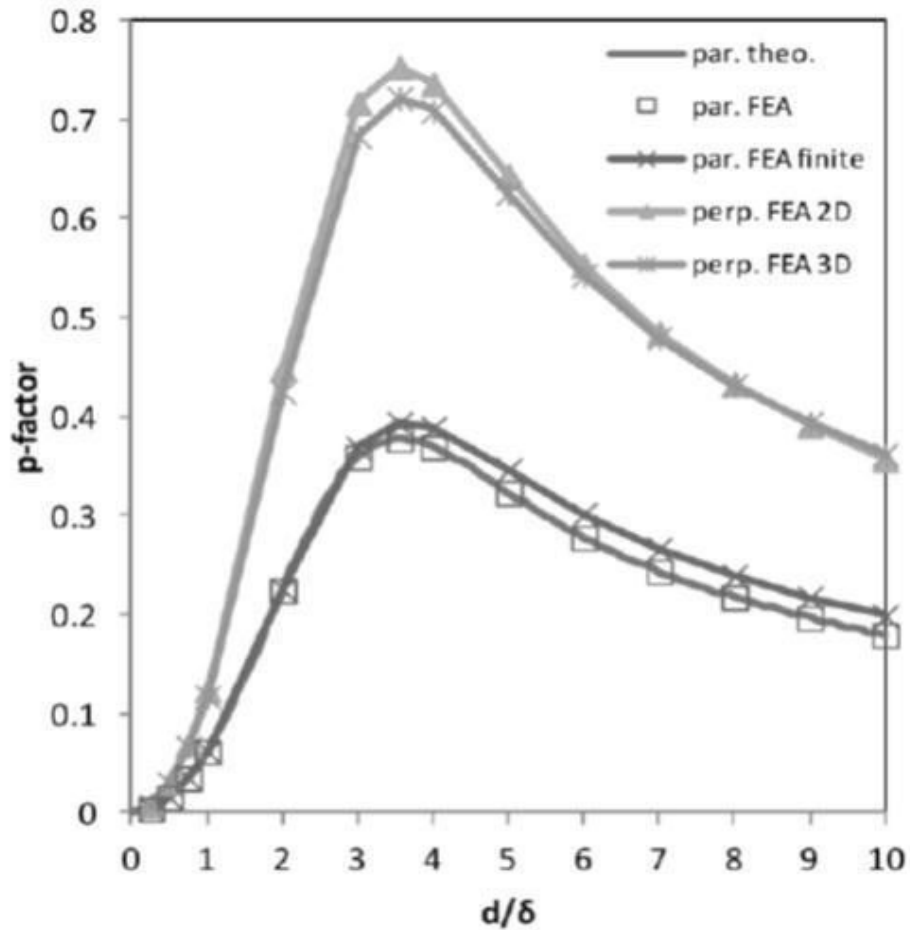


Fig. 3.10: scale factor determined using FEA models for parallel and perpendicular field orientation

The effect of a finite cylinder on the heating due to the magnetic field was not appreciable provided the cylinder was long enough for the skin effect at the ends of the cylinder not to interact. It was observed in Fig. 3.12 that the effect of a finite coil caused the temperature to drop relative to the theoretical value. Therefore employing the theoretical equations and accounting for the orientation of the field, will result in a conservative estimate where the coil dimensions are finite relative to the cylinder.

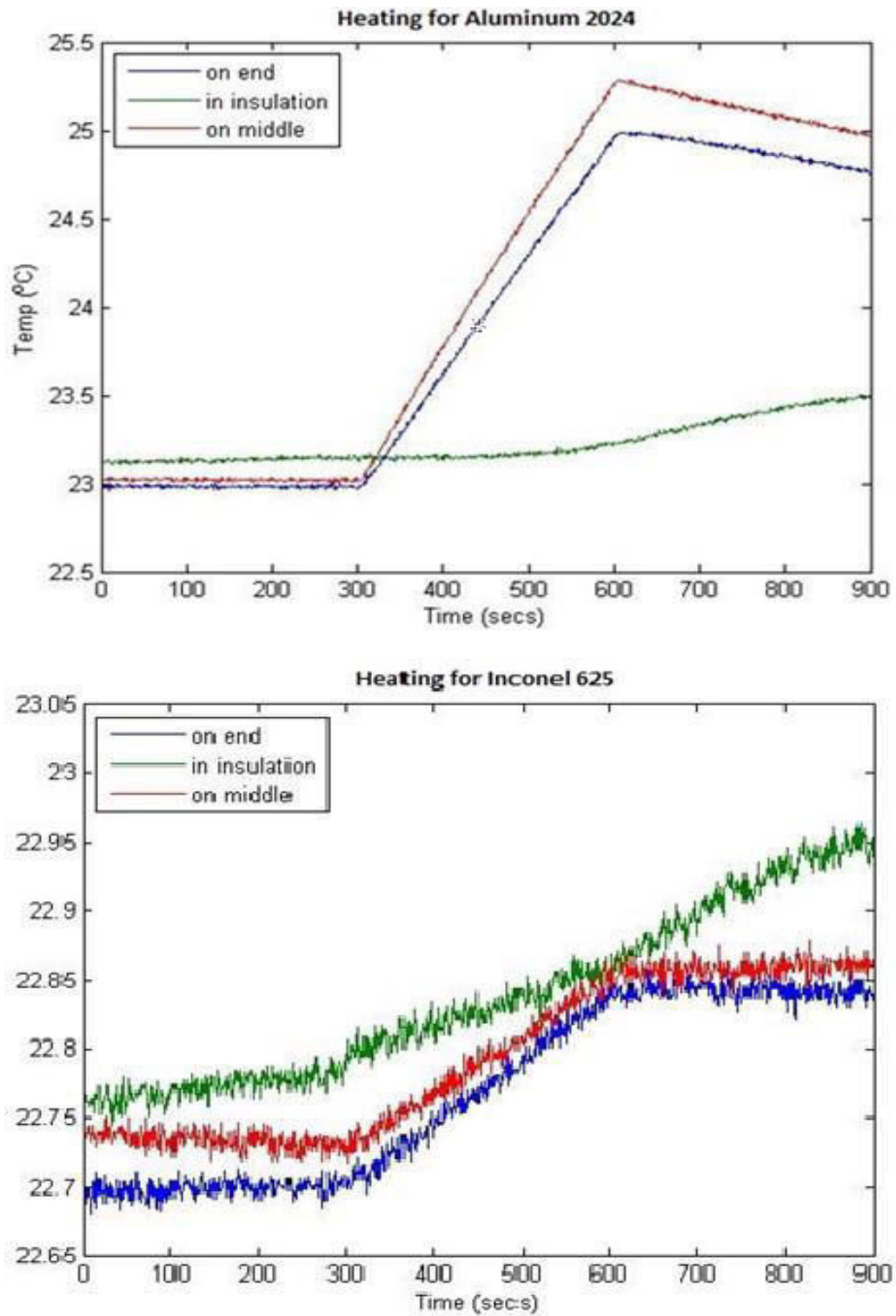


Fig. 3.11: characteristic experimental heating profile for Aluminum 2024 and Inconel 625

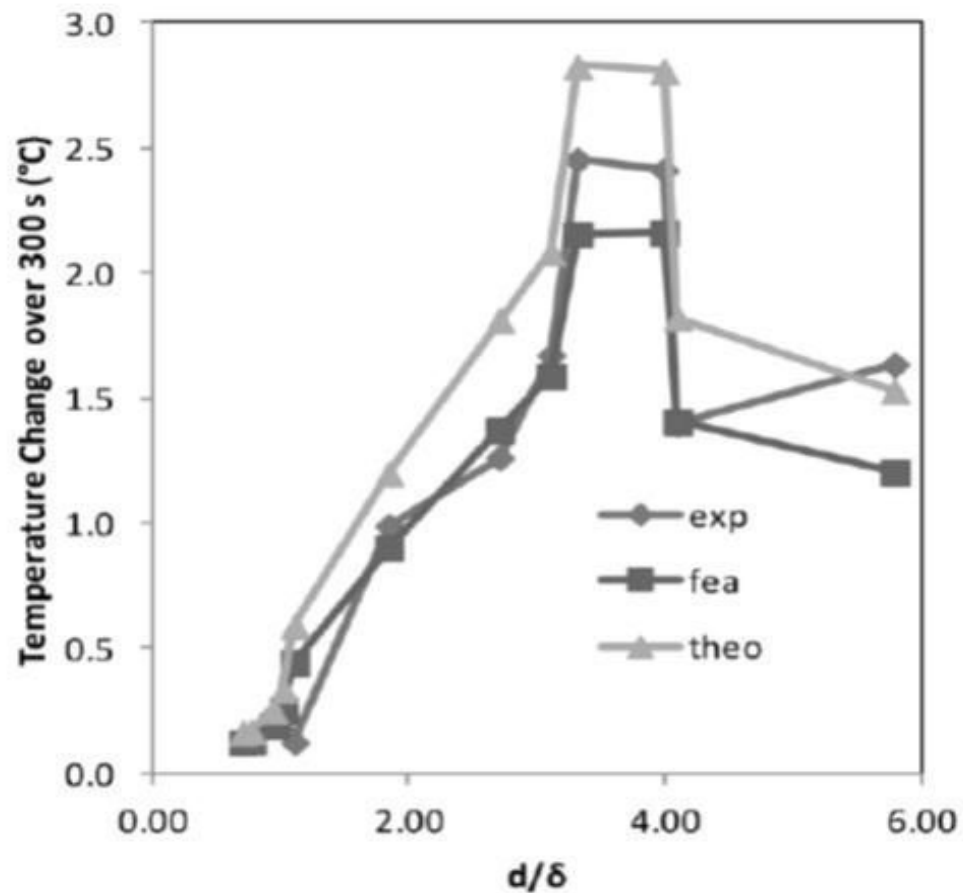


Fig. 3.12: comparison of the temperature change as determined by experiment, FEA and theoretical modeling

3.6 Summary

RF heating experiment did not show any remarkable temperature rise in the sample material as the volume of the samples was quite small and its length did not resonate with the scanner wave length. For gradient field induced heating the maximum rise in temperature was 2.45 Celsius (in Al 2024 sample) which has to be simulated in an extreme position in the scanner to achieve this rise in temperature and a minimum of 0.12 Celsius (in Inconel). The maximum temperature changes occurred at the middle position of the insulated test sample, whereas the minimum temperature changes occurred at the tip of the insulated sample due to heat losses as observed in the experiment. From the results

it can be concluded that the rise in temperature was not of significance due to the low volume of material used and rate of heat dissipation occurring in the samples which makes it safe for the actuator to operate safely inside the scanner bore.

Table 3.2: Measured Temperature Rise.

| Material | d/δ | ΔT at 300s |
|--|------------------------------|--------------------------------------|
| Inconel (Alloy 625) | 0.70 | 0.12 |
| Stainless steel (Alloy20) | 0.77 | 0.15 |
| Stainless steel (Alloy 304) | 0.94 | 0.24 |
| Monel (Alloy K-500) | 1.02 | 0.27 |
| Titanium (grade2) | 1.11 | 0.12 |
| Bronze (Alloy 642) | 1.84 | 0.99 |
| Phosphor Bronze (Alloy 510) | 2.71 | 1.26 |
| Brass (Alloy 360) | 3.11 | 1.67 |
| Aluminum (Alloy 2024) | 3.31 | 2.45 |
| Aluminum (Alloy 6061) | 3.99 | 2.41 |
| Beryllium Copper (17510) | 4.09 | 1.40 |
| Copper (Alloy 145) | 5.79 | 1.64 |

Finally, the research developed an accurate yet simple model for gradient-induced component heating that would benefit designers of new devices at the design stage. It would be assumed that the designers selected the dimensions of the components such that they do not become waveguides and absorb RF energy. Therefore the dominant heating effect would be through the gradient switching. The designer would use this information to decide on the material for a particular component.

Chapter 4

Design of Two Degree of Freedom MR-Compatible Actuator

4.1 Introduction

To establish appropriate actuator performance targets, research on needle insertion in skin and soft tissues presented in [3-6] was considered for force, speed and torque values. Testing done in [3] simulated the needle forces using 18 gauge needle inserted in a soft material phantom from polyvinylchloride (PVC). Tests were done at different insertion and rotational speeds and resulted in a maximum insertion force of almost 2.5 N and torque of 0.17 N.mm with an average speed of 5 mm/s. Using these results as the basis for a common needle-guided intervention we targeted an actuator with a 80 mm range, linear speed up to 9.8 mm/s, rotary speed of 11.5 rpm, output thrust up to 13N and a torque exceeding 22 N.mm.

The concept and design parameters of the novel piezoworm motor are presented in the following sections and will be discussed in terms of principle of motion for the piezoworm actuation method, design of the actuator, and the theoretical equation of force and torque involved in the design process.

4.2 Principle of motion

The proposed actuator design is shown in Fig. 4.1a as a CAD model and in Fig. 4.1b as the final product. Motion is based on the piezoworm configuration (will be explained in detail in the next section) which employs two piezostacks for clamping on the shaft and a third piezostack to provide the extension while the shaft is clamped and though the linear motion generated. The same set of clamps is used for both linear and rotary motion but to produce the rotary motion a fourth piezostack was added which rotates a plate around its own axis and is attached to the front clamp refer to Fig. 4.3a. By using the same set of clamps for both linear and rotary motion the overall size of the actuator is reduced and by using separate extending actuators for each degree-of-freedom the motions can be undertaken separately or jointly to achieve the required motion (linear/rotary). Utilizing a shaft as the moving member, similar to [68], minimizes the size (and its MRI signature) for the device. In future refinements of this design the device will act directly on the needle during the intervention but at this time it was planned to use a shaft for the testing of the prototype.

The clamp arrangement is based on the complementary clamp concept developed in [114]. Clamps are designed to grip on the shaft and this configuration reduces the number of actions involved in creating a single step motion compared to the conventional piezoworm [44]. This is because both clamps are derived simultaneously from one signal amplifier to reduce the number of driving components for linear and rotary motion. Another important benefit of using complementary clamps is that if the power is suddenly lost the shaft will automatically be secured safely in place.

4.2.1 Principle of Linear motion

The principle of linear motion is based on the piezoworm principle where three piezostacks are arranged to move a shaft linearly. Fig. 4.2a shows a schematic of the arrangement of the piezostacks. The two vertical stacks are used to clamp on and release the shaft in an opposite manner, and the third horizontal one extends while the horizontal

stacks are de-energized providing step advancement for the shaft (which in this case is 9 μm).

As illustrated in Fig. 4.2a one step can be achieved by four actuations of the appropriate piezostacks, and the direction of motion can be reversed by changing the actuation sequence. One clamp is designed to grip the shaft when the piezostack is energized and is designated the normally unclamped (NU) clamp, refer to Fig. 4.4. The other clamp is designated as normally clamped (NC) and grips the shaft when the piezostack is de-energized, refer to Fig. 4.5.

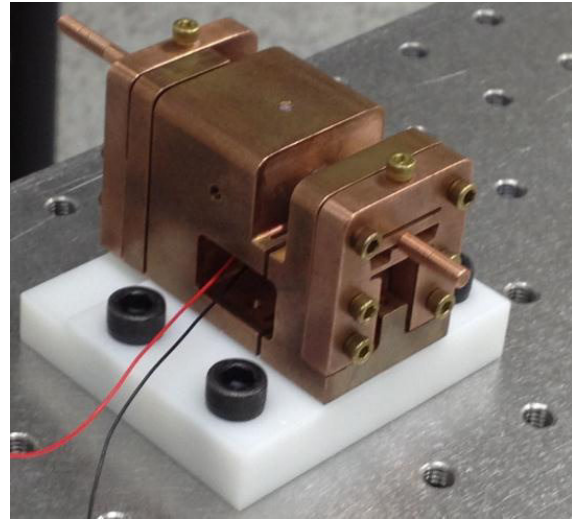
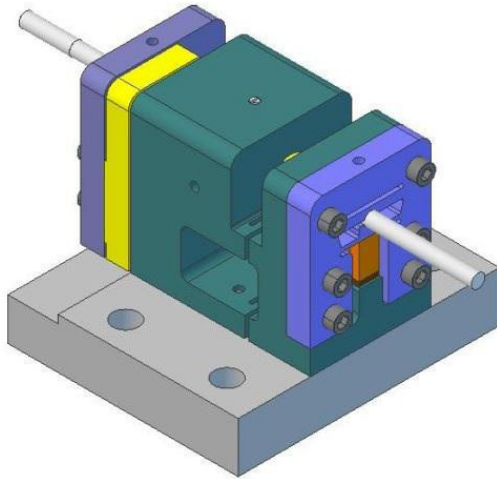


Fig.4.1: (a) Actuator CAD model

(b) Manufactured prototype

The advantage of this arrangement is that in a conventional piezoworm complete steps are done in six successive actuation operations but in the case of a complementary piezoworm only four actuation operations are required (see Fig. 4.2). This is because both clamps are driven from one signal amplifier, so one clamp opens and the other closes during the same time frame. Repeating the same steps can result of linear motion up to centimeters in range and only limited by the length of the shaft. To prevent the piezoelectric stack from experiencing shear stresses and pulling forces [44] clamps flexures were designed to

encapsulate the stacks to eliminate direct contact with the shaft though eliminating shear stresses. The piezostacks are preloaded by set screws to keep them always in compression to prevent damage from tensile forces when the actuation is repeated with high frequency [44]. The design was optimized for maximum force output. Fig. 4.3a shows an exploded view of the actuator with the four piezostacks employed. The clamp arrangement is based on the complementary clamp concept to the actuator size compact and delay circuits can be used to increase the force during the transition of the clamps [114].

4.2.2 Principle of Rotary motion

The principle of rotary motion is also based on the piezoworm principle where three piezostacks are arranged to create the rotary motion of the shaft, Fig. 4.2b shows a schematic of the arrangement of the piezostacks, the two perpendicular stacks in the figure are used to clamp on and release the shaft in an opposite manner, and the third one extends while the horizontal stacks are de-energized providing rotational step for the shaft (which in this case is 0.085 deg). As illustrated in Fig. 4.2b one step can be achieved by four consecutive actions, and the direction of motion can be reversed by changing the actuation sequence. Repeating the same steps can result with unlimited rotary motion in either direction.

In this design (as shown in Fig. 4.3a) to achieve the rotary motion the NC clamp has been mounted on a plate that has the ability to rotate about its own axis and the axis of the shaft. Another piezostack drives the rotary motion against a flexure machined in the rotary plate which springs the plate to its original position when this piezostack is de-energized. The piezostack is also preloaded with a setscrew to prevent the damage of the stack against pulling forces. The speed of the linear and rotary motion can be controlled by both the amplitude and the frequency of the controlling voltage waveforms. The direction of motion is dictated by the sequence of the actuation operations.

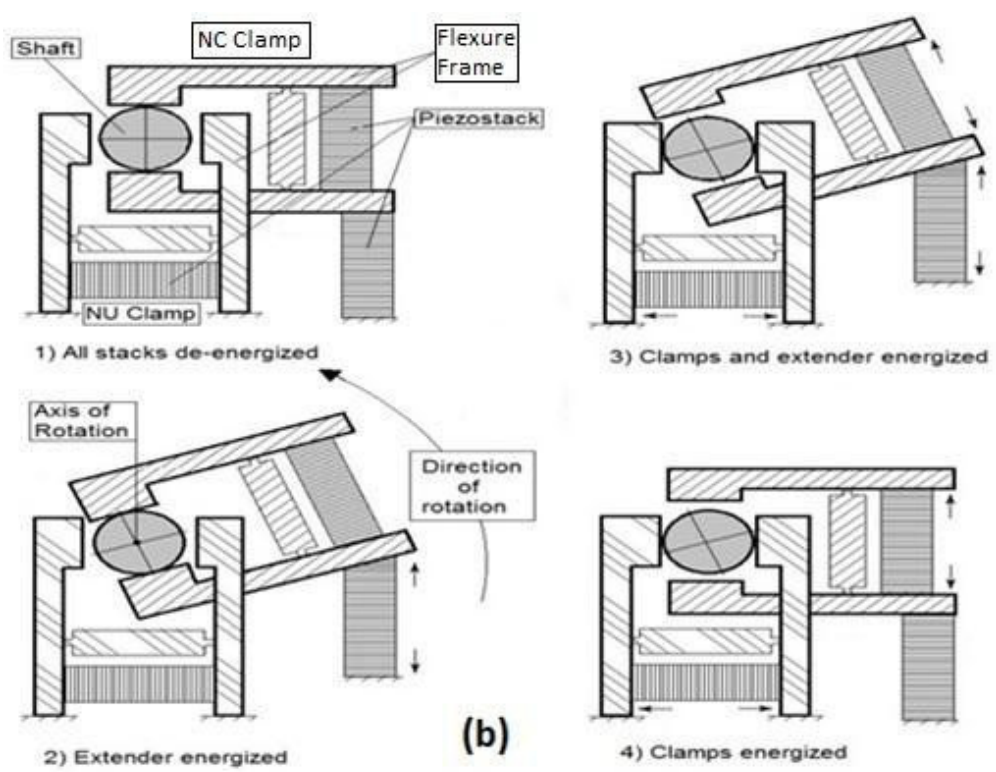
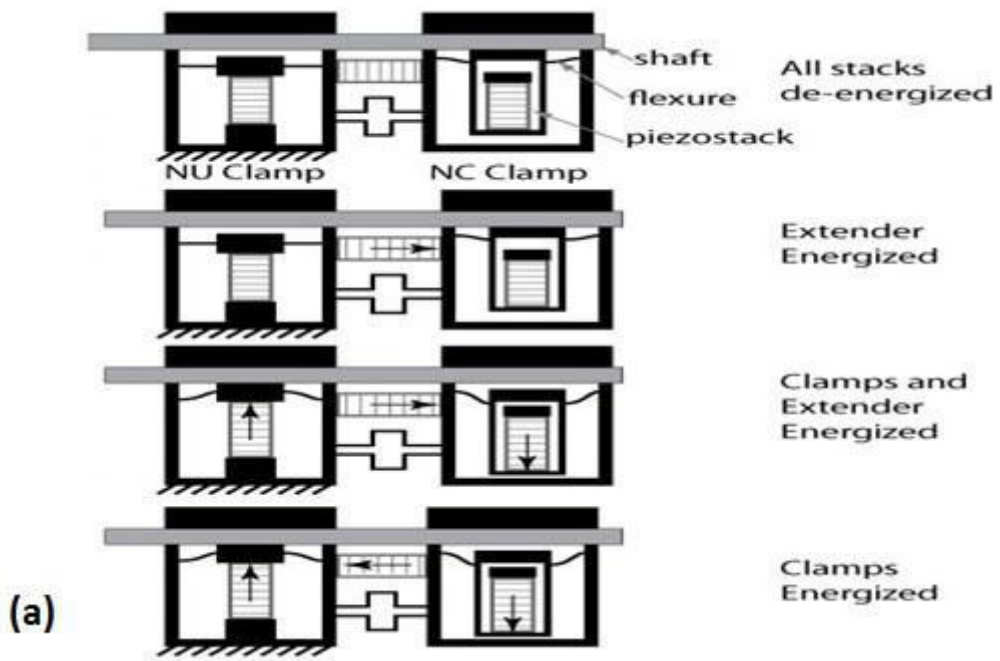


Fig. 4.2: (a) [top] Actuator linear step sequence (b) [bottom] Actuator rotary step sequence.

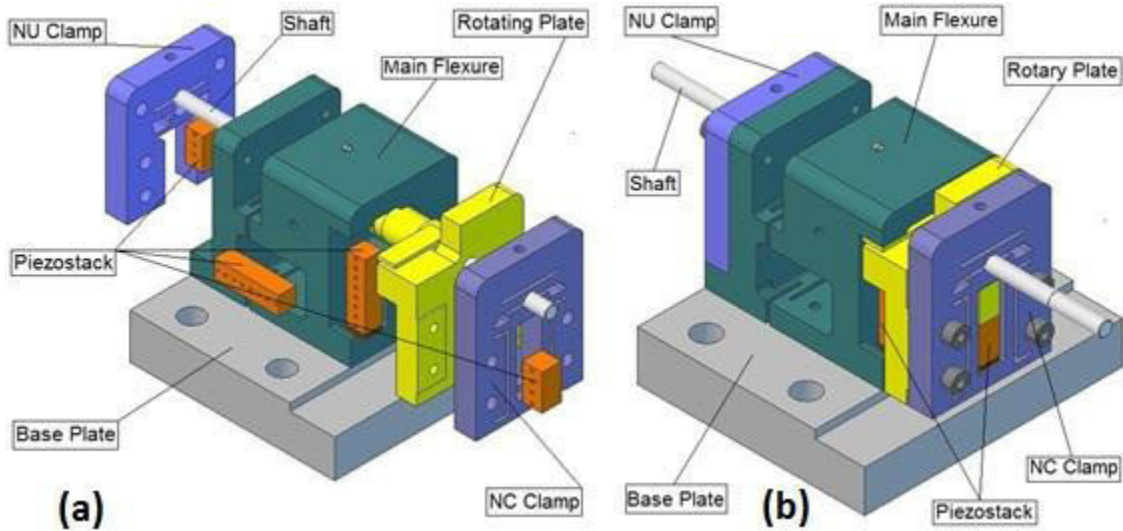


Fig.4.3: (a) Actuator model Exploded view (b) Actuator model showing different component

The novelty of this design is the combination of linear and rotary motion using the inchworm principle, and by using the same set of clamps for both linear and rotary motion thereby reducing the overall size of the actuator. Furthermore, by using separate extending actuator for each degree-of-freedom the motions can be undertaken separately or jointly to achieve the required motion.

4.3 Actuator Design

The availability of space inside the scanner is the main concern second to MR-compatibility of the actuator material. Furthermore, the available space also depends on orientation of the actuator in the MR scanner bore as well as the part of the body being imaged. Also, compensating between several performances objectives such as reasonable torque and thrust, long travel range and material high stiffness is very challenging but essential to undertake for designing an actuator that performs in the MR environment. All of these variable lead to the design of a very compact actuator with a minimum distortion signature.

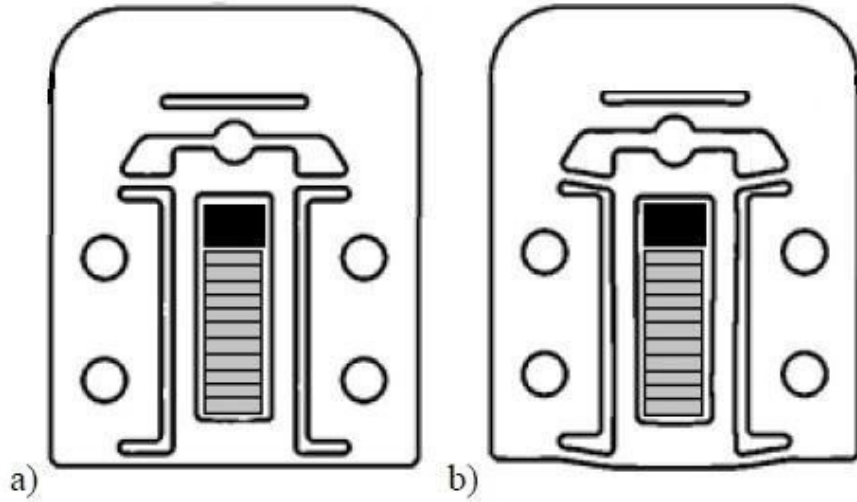


Fig.4.4: NC Clamp (a) de-energized (b) energized

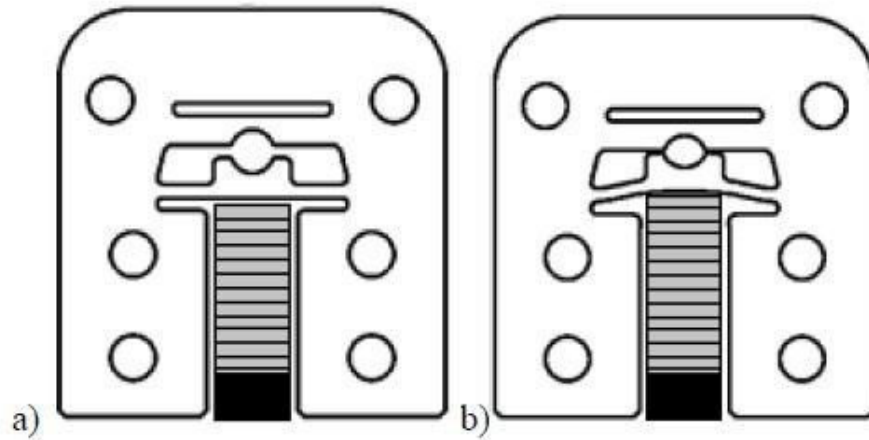


Fig. 4.5: NU Clamp (a) de-energized (b) energized

The available space inside the MRI scanner require the actuator design to strike a balance between several competing objectives which is minimizing size and image distortion producing high force output and this can be translated in selecting a material with high strength and stiffness. Also the range of travel for the proposed actuator is limited only by the available space inside the scanner. The availability of space depends on orientation of

the actuator in the MR scanner bore which makes the pusher configuration of the developed actuator perfectly suitable for performing in the restricted space available.

Selecting suitable material for the MR-compatible actuator is a challenging task as various parameters come into play such as susceptibility, resistivity, strength, and stiffness of material as discussed in [117]. The principal material property affecting image distortion is the material susceptibility. It also dictates the magnitudes of the forces and torques acting on the actuator. The material selection criterion for the proposed device was based on minimizing the susceptibility and maximizing the stiffness and strength. Hardened beryllium copper (UNS C17510) was chosen as an optimal material for this task as it strikes a balance between high stiffness and low susceptibility when compared to other engineering material tested in [117]. Though beryllium copper is expected to show some rise in temperature as presented in [8] this can be compensated by insulating the interface between the medical tool and the actuator for maximum patient safety.

4.3.1 Extension frame design

Maximizing the speeds (linear and rotary) while minimizing the size of the actuator is critical for manoeuvring tools inside the limited space inside the MRI scanner and decreasing the duration of the medical procedure. The critical factors in the speed of the actuator are the displacement range of the extender frame shown in Fig. 4.6 and its resonant frequency. To maximize the speed the flexure must be designed for maximum piezostack expansion but it must have enough mass and stiffness to keep the resonant frequency larger than the amplifier operating frequency. The constrained expansion of the piezostack, Δ , is given by equation (4.1) where k_p is the piezostack stiffness k_f is the flexure stiffness and Δ_o is the free expansion of the piezostack.

$$\Delta = \frac{k_p}{k_p + k_f} \Delta_o \quad (4.1)$$

Piezostack from Physik Instrumente (PI) P-885.51, was selected which is 5 mm by 5 mm in cross section and has a length of 18mm. Its nominal displacement is 15 μm at 100 V and has a stiffness of 50 N/ μm . The length and thickness of the flexure were set to 6 mm, 1.5 mm respectively to give a resonant frequency of 1574 Hz. The total effective stiffness of the flexures was 16.1 N/ μm . When considering the frame stiffness, the frame will have an expansion of 11 μm based on calculation presented in [114]. The maximum speed of the motor is expected to be about 9.8 mm/s based on a driving frequency of 800 Hz.

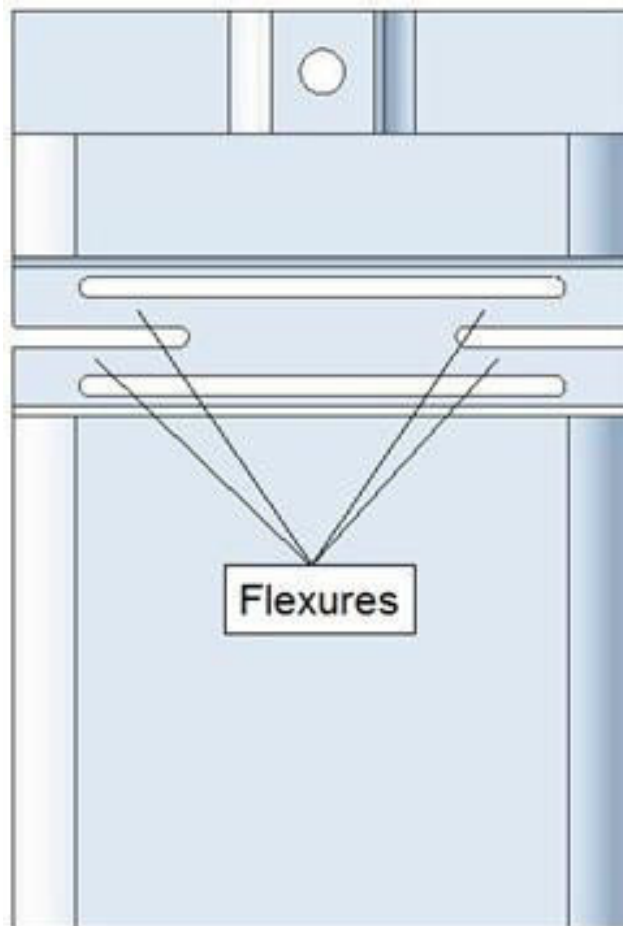


Fig. 4.6: Extension Frame

4.3.2 Rotation frame design

Similar to the extension frame, the rotational speed is affected by the displacement range of the piezostack and the resonant frequency. But this frame (Fig. 4.7) has an additional factor which is the distance away from the center of rotation.

With a fixed piezostack displacement, increasing the arm of rotation will result of larger torque and lower speed. On the contrary, decreasing the arm will result in higher speed and lower torque. The arm length was selected to be 11.75 mm to optimize for maximum speed at the targeted torque. The rotating plate flexure width is 6 mm and its length and thickness were set to 6.5 mm and 0.8 mm respectively to give a resonant frequency of 5928 Hz. The stiffness of the flexure is 1.6 N/ μ m. Based on equation (4.1), the frame will have an expansion of 12 μ m. The maximum speed of the motor is expected to be about 11.5 rpm and torque of at least 22 N.mm based on a driving frequency of 800 Hz.

4.3.3 Clamp Design

The clamp configurations are shown in Fig. 4.4 and 4.5 in both their energized and de-energized states. The piezostack shown in gray pushes against the black tab which is rigidly fixed to the supporting frame. The displacements shown are exaggerated for clarity as the actual displacements are in micrometers.

In [115], it was thought that ideally both clamps should be the same shape and size to perform a fully complementary action, so as to achieve the same dynamic performance and to facilitate simultaneous manufacturing using electro-discharge machining. However, the way in which each clamp develops its clamping force is different. In the NU clamp, the piezostack pushes up to grip the shaft so the flexure in this case is simply to guide and protect the piezostack. The NU flexure stiffness should be minimized so as to not impede the piezostack motion and will in turn increase its clamping force. The lower bound on the flexure stiffness is governed by the maximum bending stress.

The NC clamp grips the shaft when it is de-energized so the clamp force is developed by the displacement of its flexure. Now, the flexure stiffness must be maximized in order to get the most clamping force.

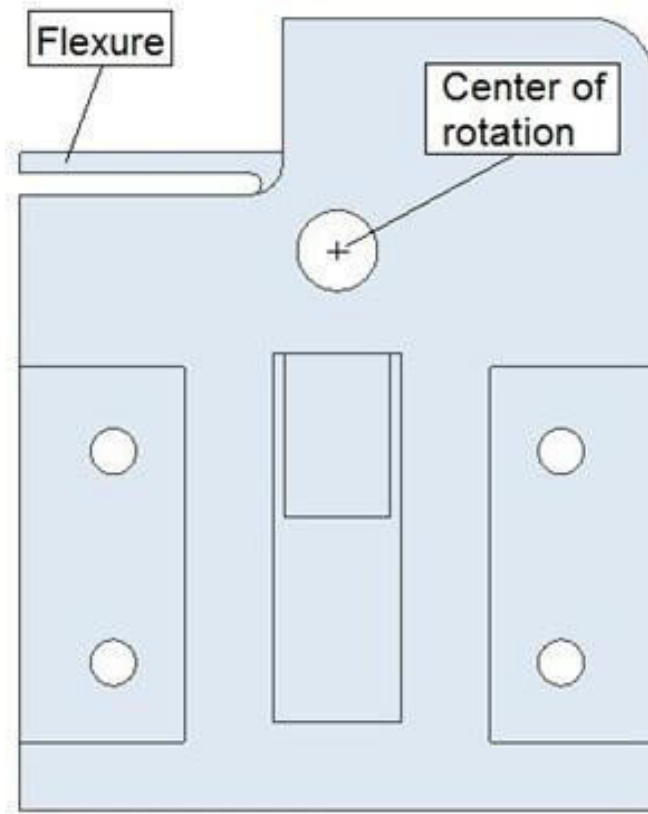


Fig. 4.7: Rotational Frame

However, if the flexure is too stiff the piezostack will not be able to fully disengage the clamp. Bending stress is also a consideration here as well. Both clamps use the same ceramic material piezostack element from PI, P-885.11. The piezostacks have a cross section of 5 mm by 5mm and a length of 9 mm. Their nominal displacement is $6.5 \mu\text{m}$ at 100 V with a stiffness of $100 \text{ N}/\mu\text{m}$.

These piezostacks were selected for this application as they offer high stiffness in small size package, and sufficient nominal displacement. The flexure width and thickness were set at 6 mm and 1 mm respectively. The length of the flexures was varied to achieve the desired stiffness for each type of clamp. The NU flexure has a length of 4 mm which gives a stiffness of $19.5 \text{ N}/\mu\text{m}$, and the NC flexure is 5 mm long with a stiffness of $10.6 \text{ N}/\mu\text{m}$.

The predicted clamp forces are 16 N for the NU and 13 N for the NC clamp based on 0.23

friction coefficient. The resonant frequency is 18243 Hz for the NU clamp and 7370 Hz for the NC clamp which is well above the maximum drive frequency of 800 Hz.

4.4 Theoretical torque and force

The concept of the torque and force generation in the proposed piezoworm is through friction, radius of the shaft, and the applied perpendicular piezostack force. The equations for the torque and force can be expressed as follows [69].

$$T_a = \mu_f N r \quad (4.2)$$

$$F_a = \mu_f N \quad (4.3)$$

Where μ_f is the frictional coefficient from experiment, N is the normal load between the stator and the shaft, r is radius of the shaft.

N can be calculated from the following equation as discussed in [54].

$$N = \Delta_0 k_p \left(\frac{k_p}{k_p + k_f} \right) \quad (4.4)$$

Where Δ_0 the nominal extension of the piezostack, K_p is the piezostack stiffness, K_f is the flexure stiffness and can be calculated as follows [116].

$$k_f = \frac{Ew(t/L)^3}{1+2C(1+\nu)(t/L)^2} \quad (4.5)$$

Where E Young's modulus of elasticity is, w is width of the flexure, t is the thickness of the flexure, L is its length, ν is poisson's ratio, and C is the shear stress correction factor, and in this case equals to 1.5 as given in solid mechanics texts [116].

The average linear speed [$\mu\text{m/s}$] is a function of the displacement of the piezostack per step and the frequency for the step to occur which can be equated as follows.

$$v_{L_{av}} = \Delta \cdot f \quad (4.6)$$

Where Δ the displacement of the extender piezostack is each step, and can be calculated from the following equation [54].

$$\Delta = \Delta_0 \left(\frac{k_p}{k_p + k_f} \right) \quad (4.7)$$

The average angular speed [rad/s] is a function of the displacement of the piezostack per step, the radius of the shaft, and the frequency for the step to occur which can be equated as follows.

$$\omega_{av} = \frac{\Delta}{r} \cdot f \quad (4.8)$$

4.5 Summary & Conclusion

A novel two degree of freedom piezoworm actuator concept was developed specifically to be MR-compatible. Rotational and linear motions can be actuated simultaneously or separately according to the demands of the medical procedure. The structural elements are made from beryllium copper and complementary clamps configuration is integrated to minimize the number of drive channels and to act as a brake in case of a malfunction. The design calculations showed that the performance targets should be achieved in the compact envelope. Analysis was carried out to optimize the selection of the piezostacks and flexures depending on the functional requirements. Prototype construction and experimental evaluation was conducted and discussed in the following chapter. The device is targeting a maximum speed of 9.8 mm/s, a force thrust of 13 N and 11.5 rpm of rotational speed and 22 N.mm of torque.

Chapter 5

MR-Compatibility and Performance Tests

5.1 Introduction

For the optimal performance of the prototype machining tolerances of $2.5\mu\text{m}$ has to be realized for all sliding surfaces. Thus a very precise fabrication method for the prototype components and perfect alignment of the assembled parts are essential for the overall static and dynamic performance of the prototype.

MR-compatibility of the device dictates the magnetic properties of the materials involved in the construction of the device, namely low susceptibility material property has to be employed for minimum image distortion. Therefore, the main components of the prototype were machined from hardened beryllium copper alloy C17510 for achieving these close tolerances, minimizing image distortion and reducing the wear on sliding surfaces. The clamps flexures were manufactured using wire EDM process to realize the complex geometry needed for these mechanisms to function properly.

In this chapter a description of the prototype fabrication is highlighted in the following section including the material used for each component. Experimental results assessment and validation of the system performance while varying the frequency of the driving voltage is discussed in terms of linear/rotary speeds, experiments to verify the load and

torque capacities of the device were also conducted. Furthermore, the MR-compatible experiments results of the prototype in terms of image distortion are presented under application of various MR sequences.

5.2 Manufacturing of prototype

The manufacturing of the components was planned to accommodate the existing manufacturing techniques adapted by local manufactures to keep the expenses within the budget of the project as this a proof of concept for a linear/rotary piezoworm actuator.

It was decided that the limit for a higher tolerances for the sliding parts was $12\mu\text{m}$. These surfaces include the clamping holes for the NU and NC clamps. This number was calculated to accommodate for the straightness value of the shaft, flatness, and perpendicularity of the assembled components. To compensate for tolerance degradation alignment fine tuning methods were devised to accommodate for any manufacturing deficiency such as shaft straightness. One of these methods is designing an extra flexure for the sliding surface adjustable by means of a set screw to assure surface contact between the shaft and the clamping surface as shown in Fig. 5.1. Another method for fine adjustment of any misalignment is making a slightly bigger fastener holes between the main flexure and the complementary clamps for the final adjustments of misalignments.

All the non-sliding and fixed components namely main flexure, NC, and NU clamps were designed to a flatness value of $1\mu\text{m}$ and perpendicularity value of $1\mu\text{m}$ to allow for successful alignment of the $10\mu\text{m}$ straightness over the shaft entire length, and $1\mu\text{m}$ roundness of the sliding shaft. To ensure the machining precision within the compact size of the clamps, the flexures were machined using an electro-discharge machining (EDM).

The rotary plate main function is to facilitate the rotation of the shaft or linearly passing through its center in case of separate rotary and linear motion, or both together in a helical motion of the shaft when moving linear and rotary motion simultaneously. The hole in the center of the rotating plate shaft was made large enough for shaft to pass the shaft freely inside without any interference with the shaft enclosure as shown in Fig. 5.2.

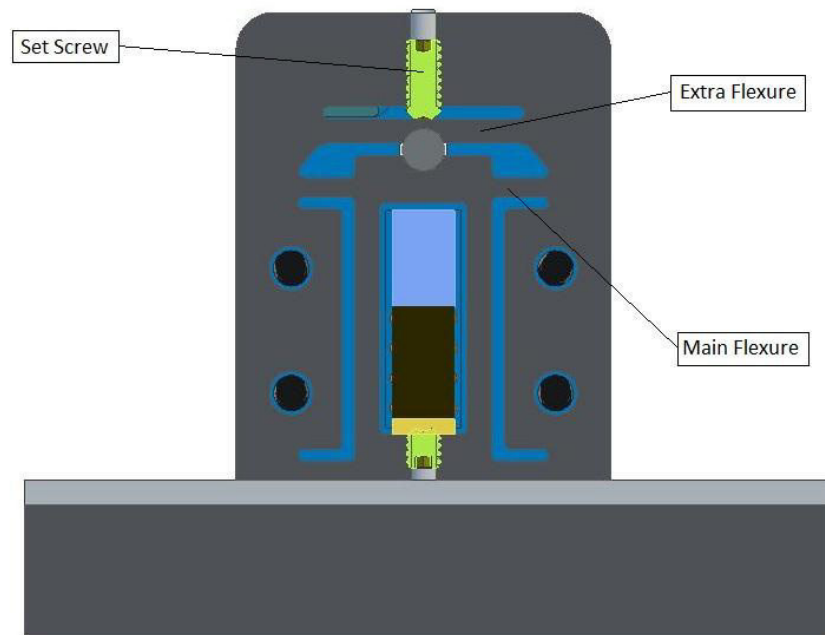


Fig. 5.1: Fine adjustment of the component misalignment using set screw & flexure

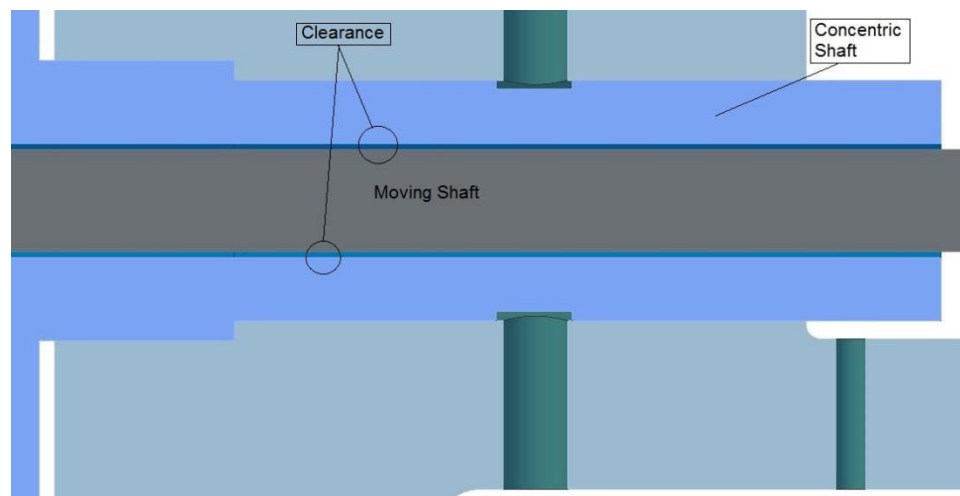


Fig. 5.2: Clearance between the moving shaft & the rotary plate concentric rotating shaft

The rotating plate shaft which is the center of rotation of the platform has a size tolerance value of $-9\mu\text{m}$ (refer to appendix A). Location fit between the plate and the main flexure body and was used for locating the plate in place and can be easily assembled, as fine

adjustment methods of 4 set screws are used for allowing the proper over all alignment of the system as shown in Fig. 5.3.

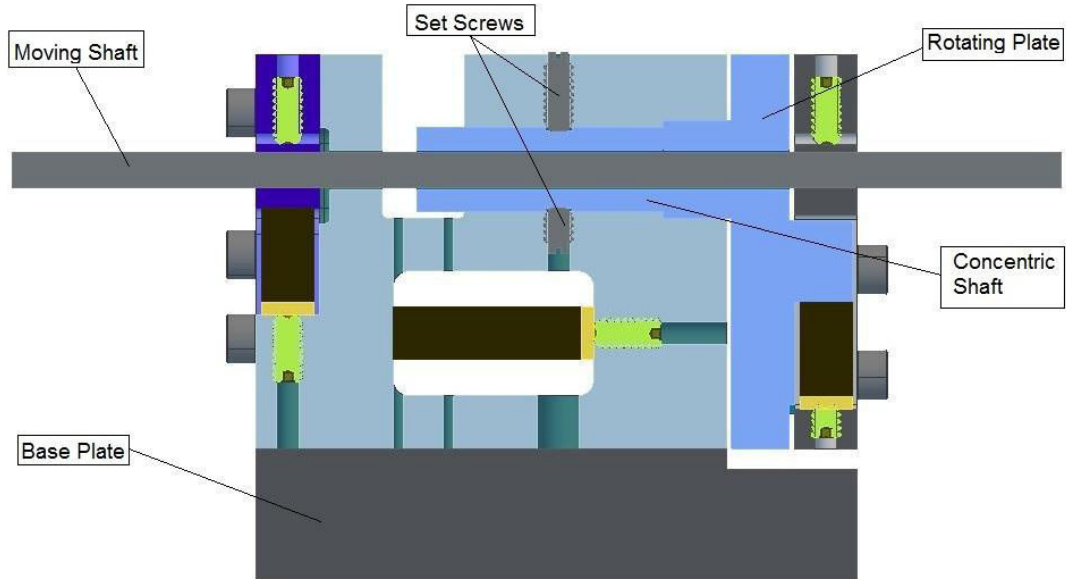


Fig. 5.3: Fine adjustment of the component misalignment using set screw

The shaft is the only sliding component in the system. It can slide linearly or rotary according to sequence of control of the complementary clamps and extender. The shaft is fabricated from the same beryllium copper alloy used for the fixed parts. Table 5.1 shows some properties of the copper alloy C17510 used in the actuator components [92-96].

Table 5.1: Mechanical, Electrical and Magnetic properties of Beryllium Copper [C17510] with heat treatment [TH04]

| Property | Value |
|--|------------------------|
| Modulus of elasticity [E] | 124 [GPa] |
| Poisson's Ratio [γ] | 0.285 |
| Yield Strength [S_y] | 741 [MPa] |
| Ultimate Tensile Strength [S_{ut}] | 845 [MPa] |
| Electrical resistivity [ρ] | 3.80E-8 [Ω .m] |
| Magnetic Susceptibility [χ] | 4 [ppm] |

All fasteners used are made from brass and so are the set screws except the four plastic ones used in locating the shaft of the rotating plate. The prototype was fitted with a plastic base for easy mounting inside and outside the MRI machine. Brass and plastic materials were chosen as they are MR-compatible and they possess enough strength for their functional purpose in the. An overview of the fabricated prototype is shown in Fig. 5.4 and some properties of brass are presented in Table 5.2 [92-96].

Table 5.2: Mechanical, Electrical and Magnetic properties of Brass C3600

| Property | Value |
|--|------------------------|
| Modulus of elasticity [E] | 106 [GPa] |
| Poisson's Ratio [γ] | 0.324 |
| Yield Strength [S_y] | 172 [MPa] |
| Ultimate Tensile Strength [S_{ut}] | 393 [MPa] |
| Electrical resistivity [ρ] | 6.60E-8 [Ω .m] |
| Magnetic Susceptibility [χ] | 112 [ppm] |

5.3 Assessment of Flexures components

The flexure mechanism of the NC clamp is responsible for the generation of force capacity, and torque capacity of the system. The main parameter for the system load capacity is the friction between the contacted surfaces, and normal force generated on those surfaces. In other words the load capacity (force/torque) is directly proportional the value of friction coefficient and applied normal forces, but for the torque capacity, in addition to the mentioned parameters, the arm length plays an important role in increasing this capacity but dramatically decreasing the component compactness and the rotary speed.

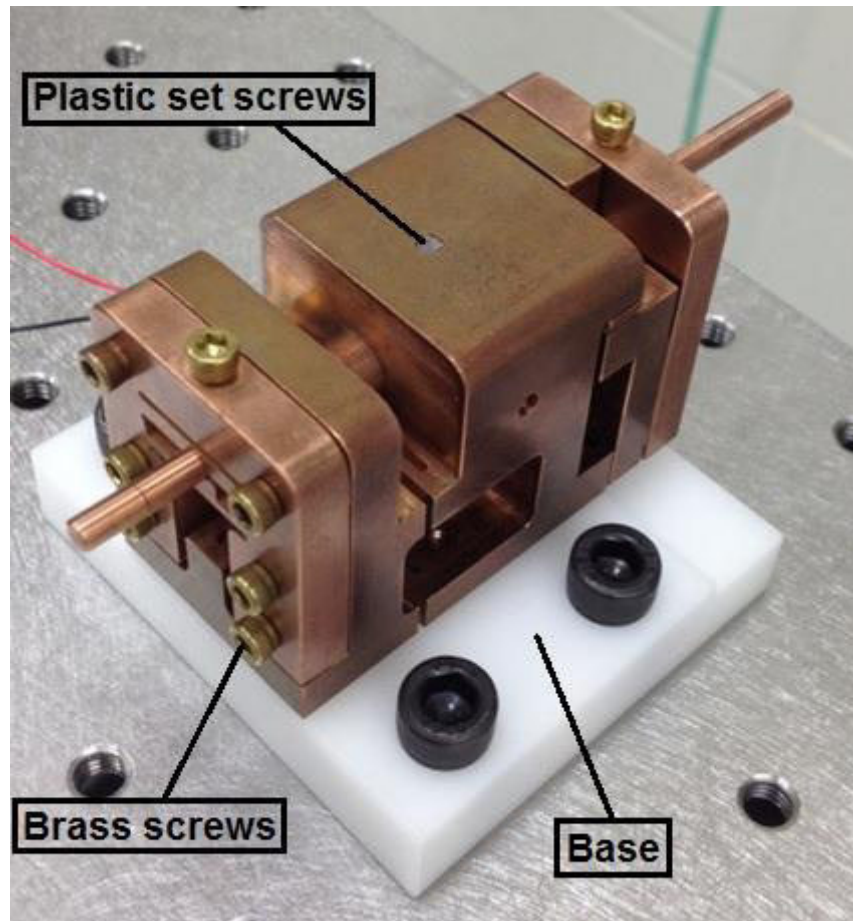


Fig. 5.4: Picture of the fabricated prototype showing copper alloy parts and plastic base

The flexure mechanism of the extender main purpose is to produce the step response for the prototype. The larger the deflection of the flexure, the bigger the step at the applied voltage of 100 V. Intermediate partial steps can be obtained by varying the applied voltage from 0 to 100 which gives in this case resolution between 20 nm to 12 μm theoretically. Preload was applied to the piezostack embedded inside the extender and laser interferometer measurement of the actual maximum step was acquired at 100 V of applied signal as shown in Fig 5.5a and b. The figure show the value of two step responses of the extender actuated at 100 V but at 2 different frequencies. Then the extender step is repeated several hundred or thousand times (limited only by the amplifier driving frequency and the resonance frequency of the system) in conjunction with clamping action

of the NC/NU clamps the speed of the prototype can be explored. The design configuration of the prototype allowed for rigid attachment of the clamps to the main body of the extender to increase the natural frequency of the prototype and hence to increase the driving frequency. The prototype linear and rotary speed performance will be discussed in the next section.

5.4 Linear and Rotary Performance Tests & Results

The prototype is capable of performing linear and rotary motion either in an independent or combined manner according to the procedure requirement. First, tests in this section were carried out to test the prototype linear performance in term of load capacity and speed, then similar tests were performed on the rotary motion and torque capacity, and finally the combined motion was quantified as will be discussed.

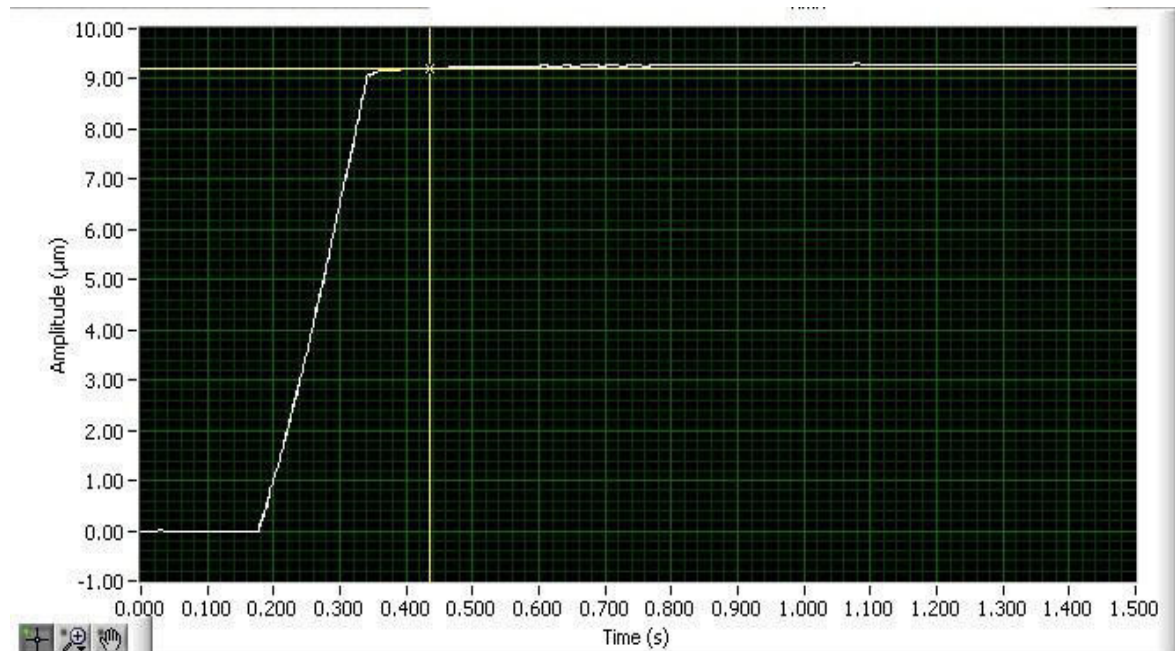


Fig. 5.5a: Step response of the prototype at frequency 1 Hz

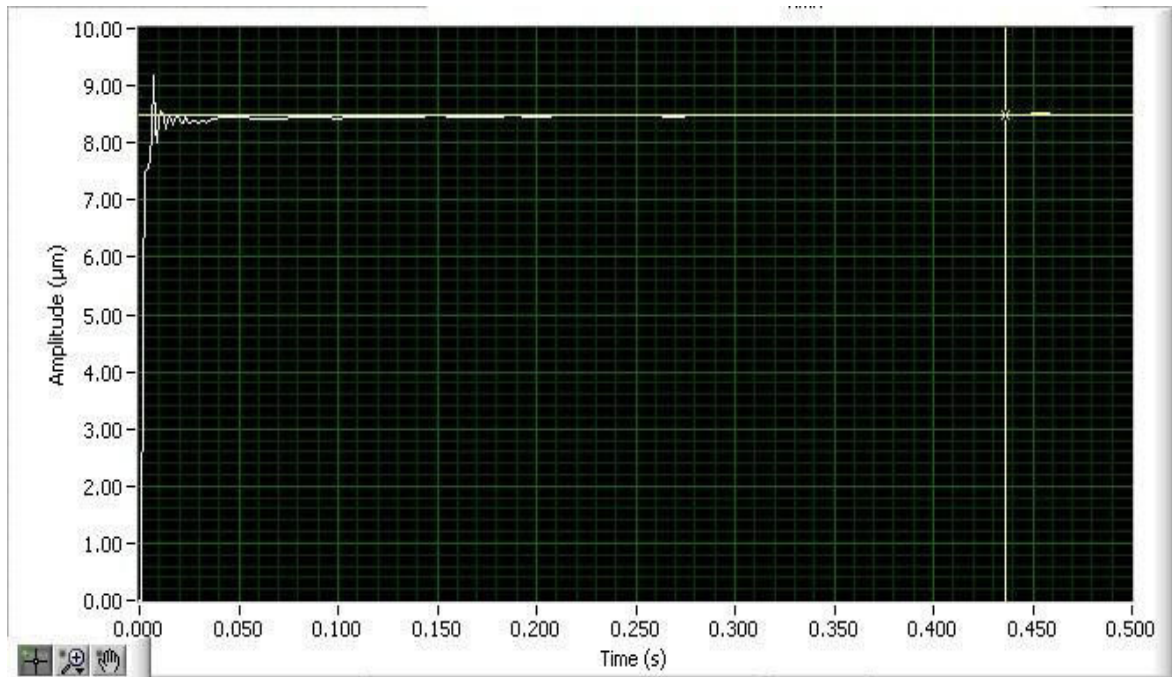


Fig. 5.5b: Step response of the prototype at frequency 800 Hz

5.4.1 Experimental Setup

The experimental setup schematic is shown in Fig.5.6a and the actual setup is shown in Fig. 5.6b and c. At one end of the shaft a rotary encoder is mounted (OMRON, E6C3-CWZ3XH with a resolution of 0.1 deg) to measure the rotary motion when mounted alone and on the other end a linear laser interferometer encoder is attached (RENISHAW, RLE 10 with a resolution of 20 nm), for measuring the linear motion when mounted alone. A PC running LabVIEW [118] on real time operating system generates the 10 V control signals needed to control the prototype. The system supplied the control signals to the amplifier [119] (PI E501) to produce an output of 100V supply at 2 Amps to drive the prototype. Amplified voltage is fed to the piezostacks of the extender and the clamps to generate linear or rotary motion according to the control sequence. The linear position x and rotary angle position θ were measured by means of the linear and rotary encoders as shown in the schematic of Fig. 5.7. The raw analog signals from the two encoders are conditioned internally to a digital quadrature phase signal suitable for the interfaced hardware of the real time system PC.

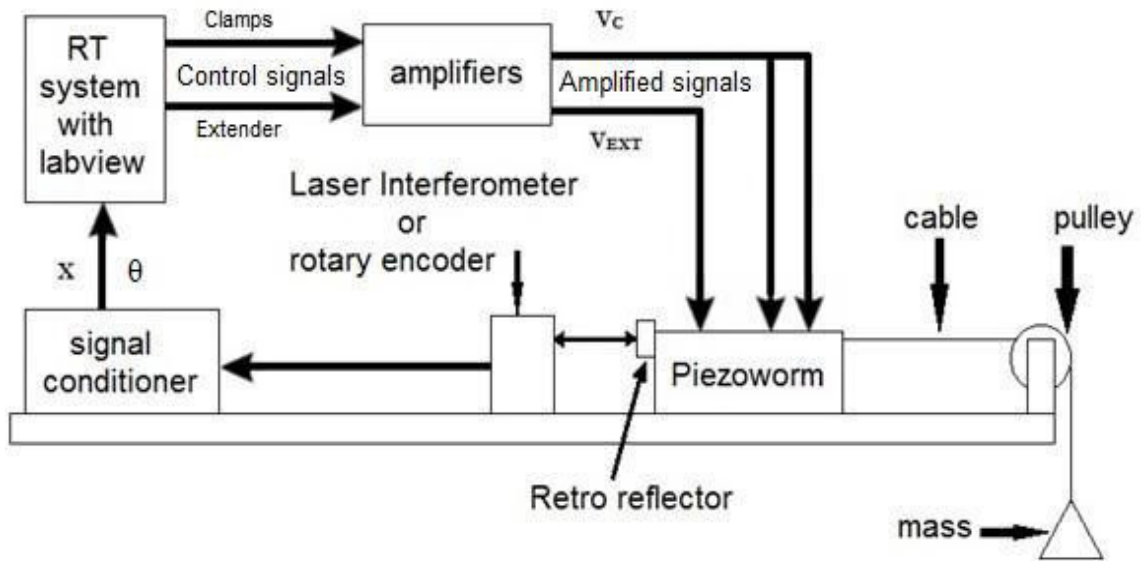


Fig. 5.6: (a) Schematic of experimental setup for force and torque capacity

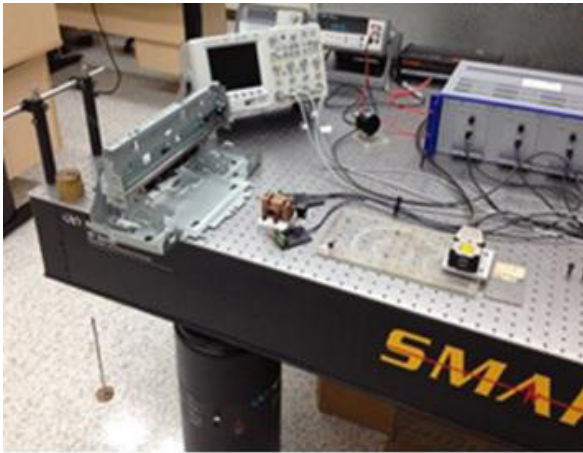
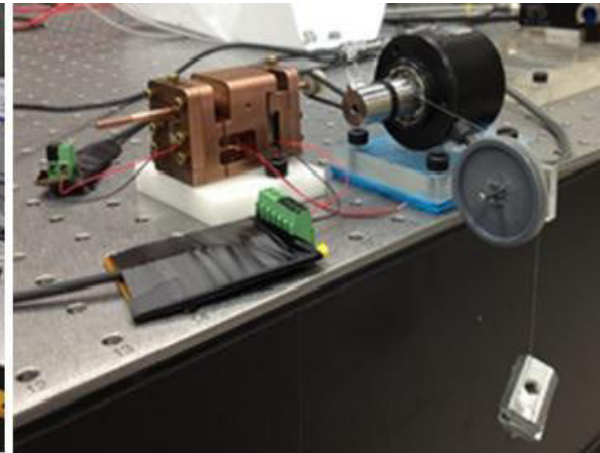


Fig. 5.6: (b) Setup for testing the force capacity



(c) Setup for torque capacity

These signals were acquired and recorded in the PC for further processing. A mass attached to the shaft via a cable around a pulley was used to apply a load to the piezoworm to measure force capacity and torque accordingly. The effects of operating frequency, force and torque loading and their effect on the speed were investigated.

5.4.2 Static Performance

In order to validate the theoretical equations for the force and torque capacities produced by the actuator the friction coefficient value of beryllium copper on beryllium copper has to be determined in order to compare to the designed values. The friction coefficient of beryllium copper on beryllium copper can be obtained either from the literature or by conducting experiments. Experimentally it was obtained by placing a piece of beryllium copper on top of the other piece and increasing the inclination angle until the piece slides. The friction coefficient was found to be 0.23, but the accuracy of this process questionable and also if we consider the dynamic friction this will not be valid. The other option was to search the literature for the value of the average coefficient of friction, but the specific coefficient of friction for C17510 was not available for the specific machining conditions of the shaft and clamps. To simplify the complex problem of measuring the coefficient of friction (static and dynamic) the experimental value was used to obtain the theoretical value of load and torque capacities, now comparison between the experimental versus theoretical values can be carried out.

In order to get the maximum load for torque capacity static performance tests were conducted. The setup shown in Fig. 5.6b was used to obtain the value of the maximum load for the system by accumulating weight until slip occurs. As for the maximum torque capacity the setup in Fig. 5.6c was used and the same technique of weight accumulation was performed to reach the maximum torque for the system. The value for the maximum load was 6 N, and the maximum torque was 10.7 N.mm. Table 5.3 shows the comparison between experimental and theoretical values for force and torque.

Table 5.3: Values of experimental versus theoretical force and torque

| Property | Design Value | Experimental Value |
|------------------------|--------------|--------------------|
| Force capacity | 13 N | 6 N |
| Torque capacity | 22 N | 10.7 N.mm |

5.4.3 Dynamic Performance

Modal analysis was conducted using finite element methods (FEA) to specify the natural frequencies of the NU, NC clamps and Extender. The Clamps and extender has been designed to be higher than the natural frequency of the driver amplifier coupled with capacitance of the used piezostack. The maximum configured frequency for the amplifier was around 800 Hz, the calculated frequency for the NU clamp was 1200 Hz, NC clamp was 7000 Hz, and the extender was 1200 Hz which is all above the lowest driver frequency. As these values suggest that the system is safe from reaching the resonance frequency, but during the experiment resonance frequency conditions were reached as high and vibration of the actuator was noticed, the values presented in Fig. 5.8 to 5.15 shows a noticeable effect of the resonance condition on the prototype performance.

5.4.3.1 Linear Dynamic Performance

The speed of the piezoworm is dependent on the step size and the driving frequency. The step size is a function of the piezoworm parameters however the step rate is limited by the amplifier frequency bandwidth of 800 Hz. In this test, a trapezoidal waveform with the duration of the rising and falling portions of the waveform limited to 25% of the signal period was used. The common clamp signal is shifted by 90° relative to the extender signal so that the clamp signal has reached its extreme before the extender begins to move. Both signals range from 0 V to 100 V. The results are shown in Fig. 5.8. The maximum speed of the motor is 5.4 mm/s is less than the predicted value of 9.8 mm/s most likely due to slipping that is occurring between the moving surfaces. The predicted value assumed perfect friction surface contact between the clamp and the shaft with no slippage. The same test was repeated for the reverse direction and the results obtained are shown in Fig. 5.10. The average values for these two tests are presented in Fig. 5.9, and 5.11 respectively. The same waveform as the previous test was used at an operating frequency of 600 Hz. The results in Fig. 5.12 show that the speed decreases roughly linearly with force to a maximum load of about 6 N. This was lower than the 13 N predicted also due to friction coefficient and slippage but this should be expected since

the timing of clamping and releasing for the NU/NC clamps is the same so lower force capacities are produced. This result is promising because if we dedicate an amplifier channel to each clamp the force will be increased and the actuator could be used for inserting the needle through variable tissue structure and the extra force can be utilized.

5.4.3.2 Rotary Dynamic Performance

A trapezoidal waveform was used with the duration of the rising and falling portions of the waveform limited to 25% of the signal period. The common clamp signal follows the extender one and is shifted by 90° relative to the extender signal so that the clamp signal has reached its extreme before the extender begins to move. The results are shown in Fig. 5.13. The maximum rotary speed of the actuator is around 10.5 rpm which is less than the predicted value of 11.5 rpm most likely due to some slipping that is occurring. The average value for the tests represented in Fig. 5.14. The same load pulling test was repeated to predict the torque capacity of the actuator with a trapezoidal waveform was used with the duration of the rising and falling portions of the waveform limited to 25% of the signal period. The same waveform as the previous test was used at an operating frequency of 600 Hz. The results in Fig. 5.15 show that the speed decreases roughly linearly with force to a maximum load of about 10.7 N.mm.

5.4.3.3 Combined Linear and Rotary Dynamic Performance

A qualitative testing was conducted to validate the performance of the simultaneous combined rotary and linear motion. A trapezoidal waveform was used with the duration of the rising and falling portions of the waveform limited to 25% of the signal period and repeated twice. The common clamp signal follows the extender one and is shifted by 90° relative to the extender signal so that the clamp signal has reached its extreme before the extender begins to move and was also repeated twice. The result was a combined rotary and linear speed of the actuator in both forward and reverses directions. The waveform previously explained test was used at an operating frequency of 700 Hz to obtain the speeds mentioned before but no recording of data was maintained as the setup does not allow the measurement of both linear and rotary measurement at the same time.

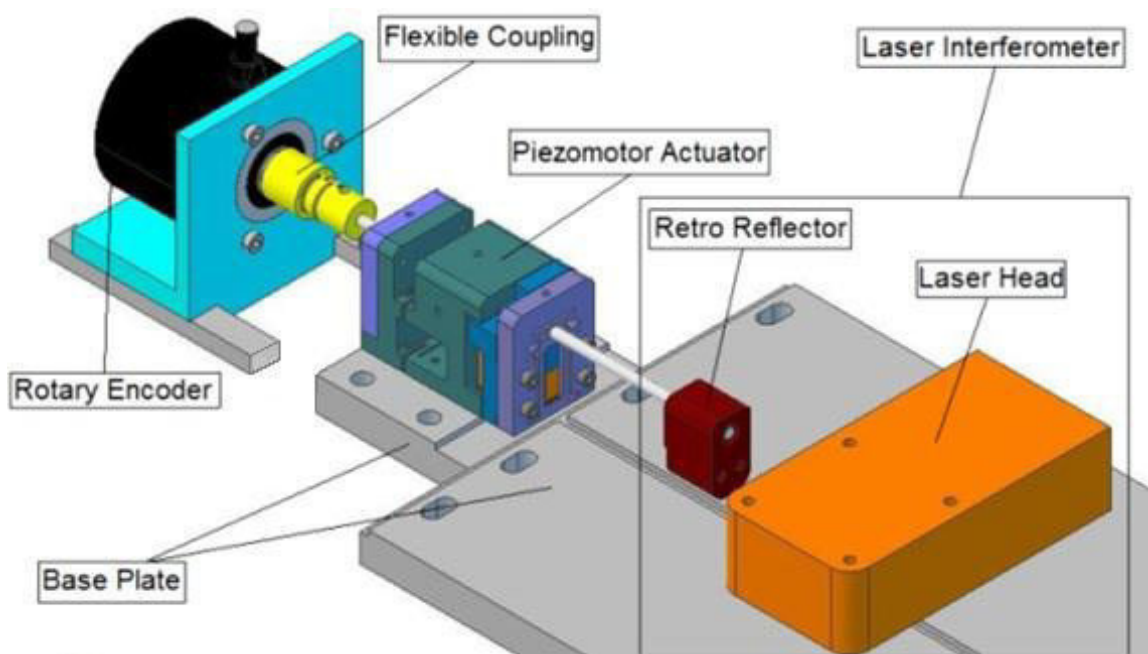
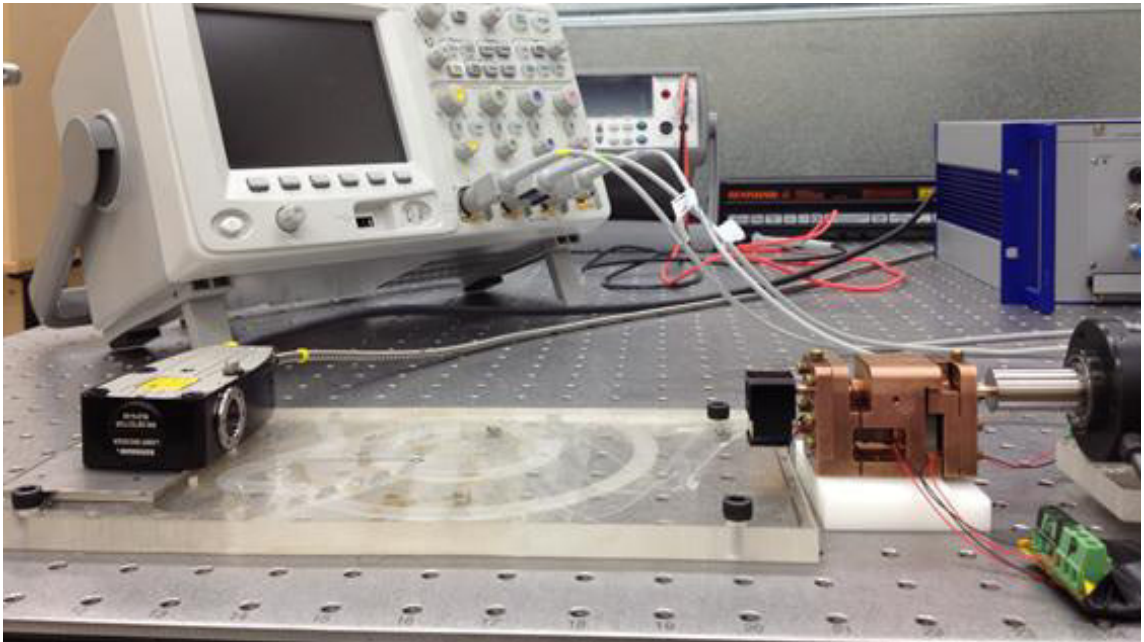


Fig.5.7: Experimental setup for testing linear or rotary motion

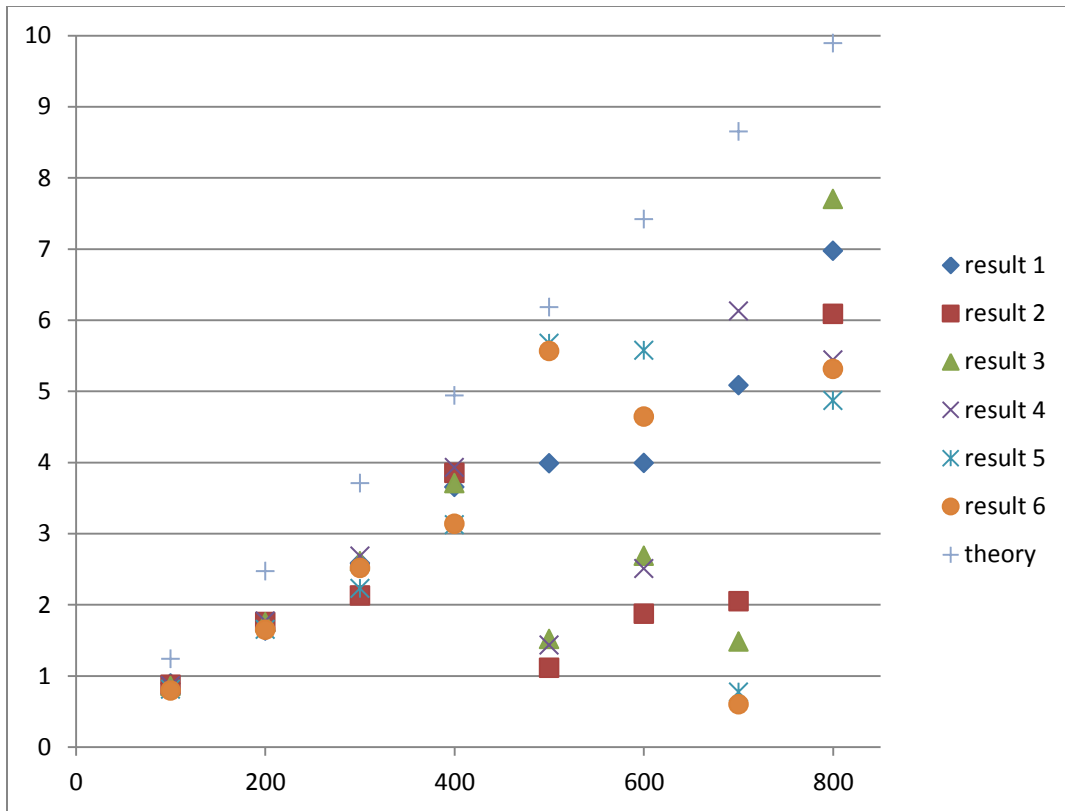


Fig. 5.8: No load speed vs. Frequency (theory and experiment forward motion)

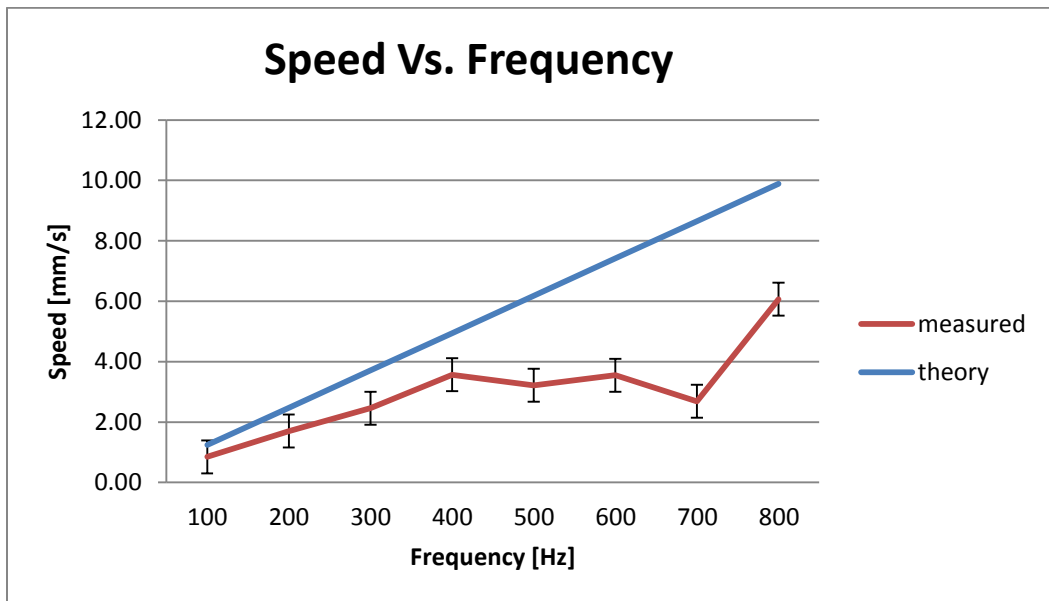


Fig. 5.9: No load speed vs. Frequency (theory and average forward motion)

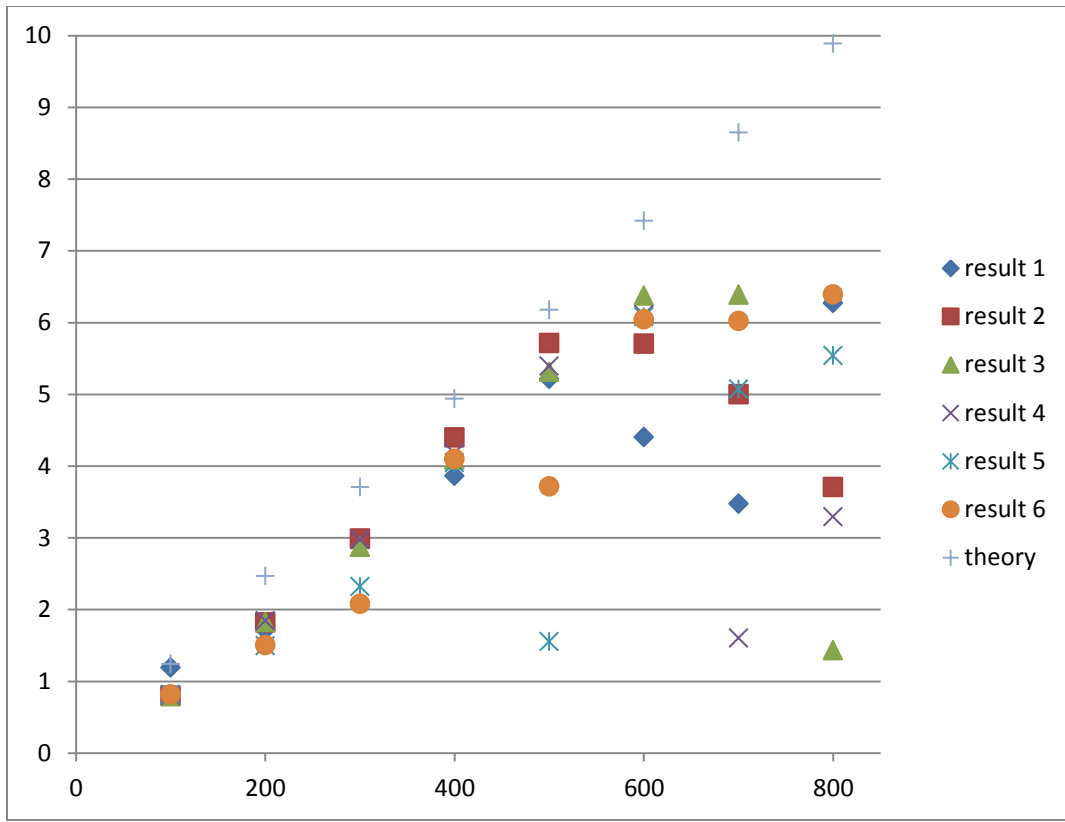


Fig. 5.10: No load speed vs. Frequency (theory and experiment reverse motion)

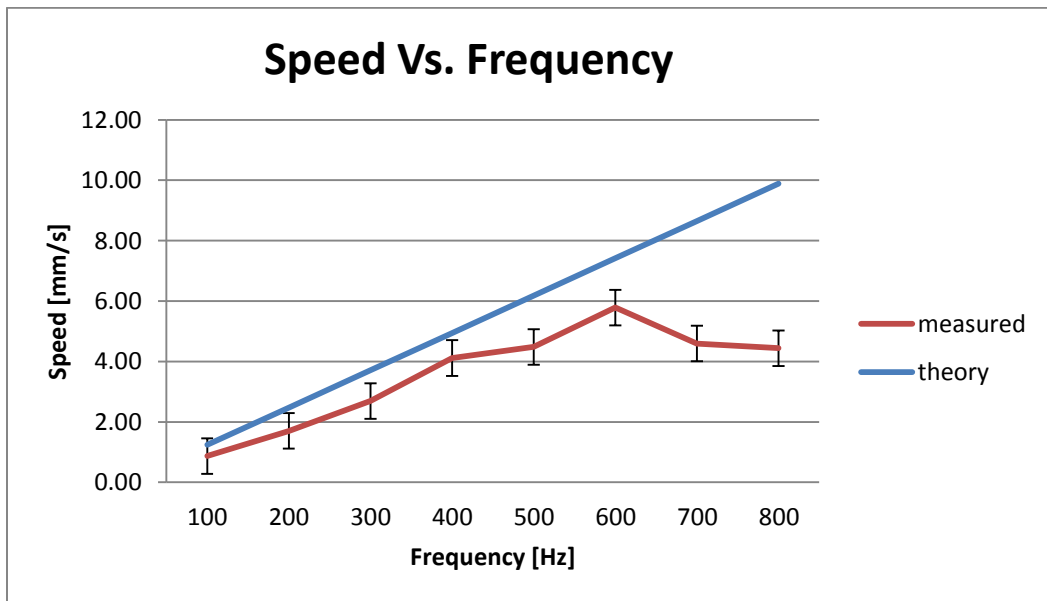


Fig. 5.11: No load speed vs. Frequency (theory and average reverse motion)

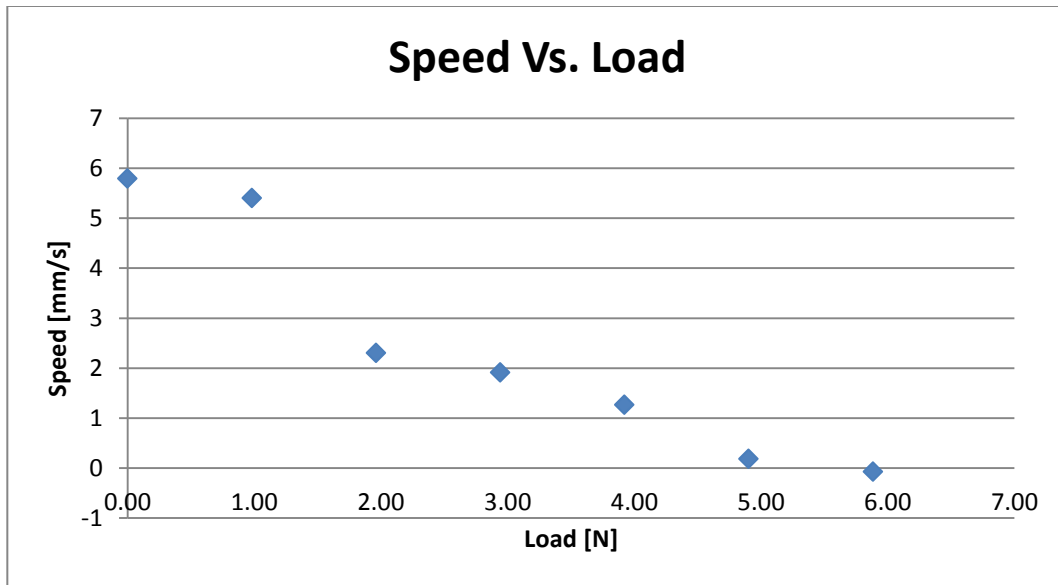


Fig. 5.12: Speed vs. load at frequency 600 Hz.

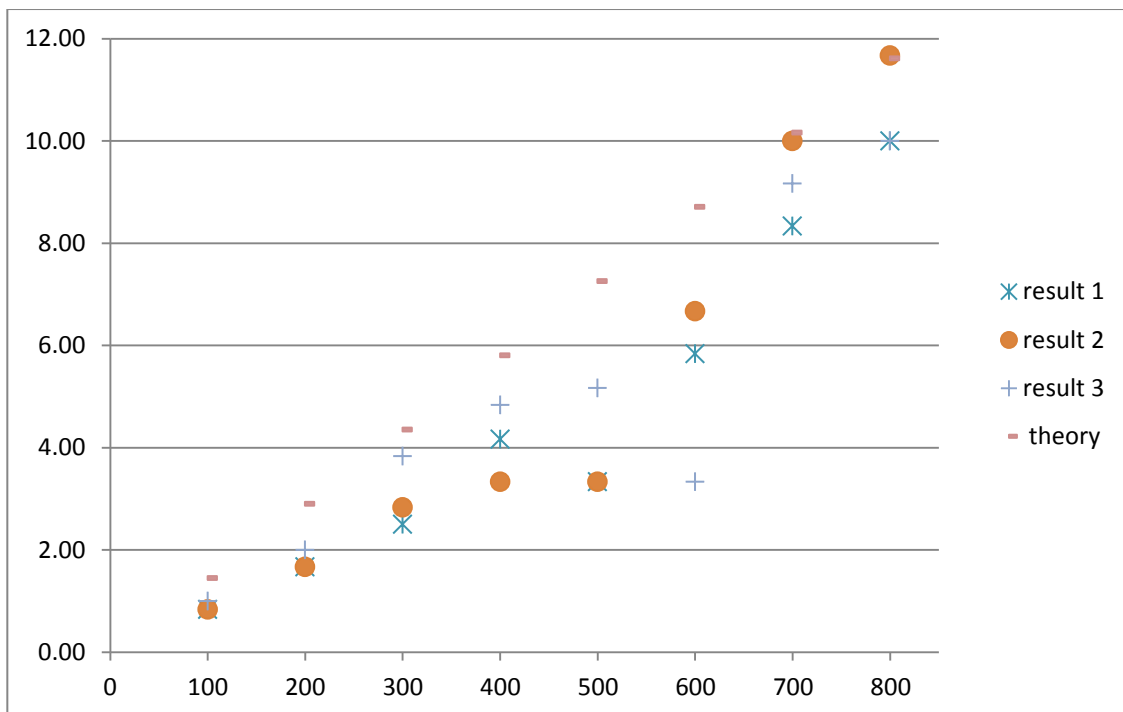


Fig. 5.13: No load rotary speed vs. Frequency (theory and experimental)

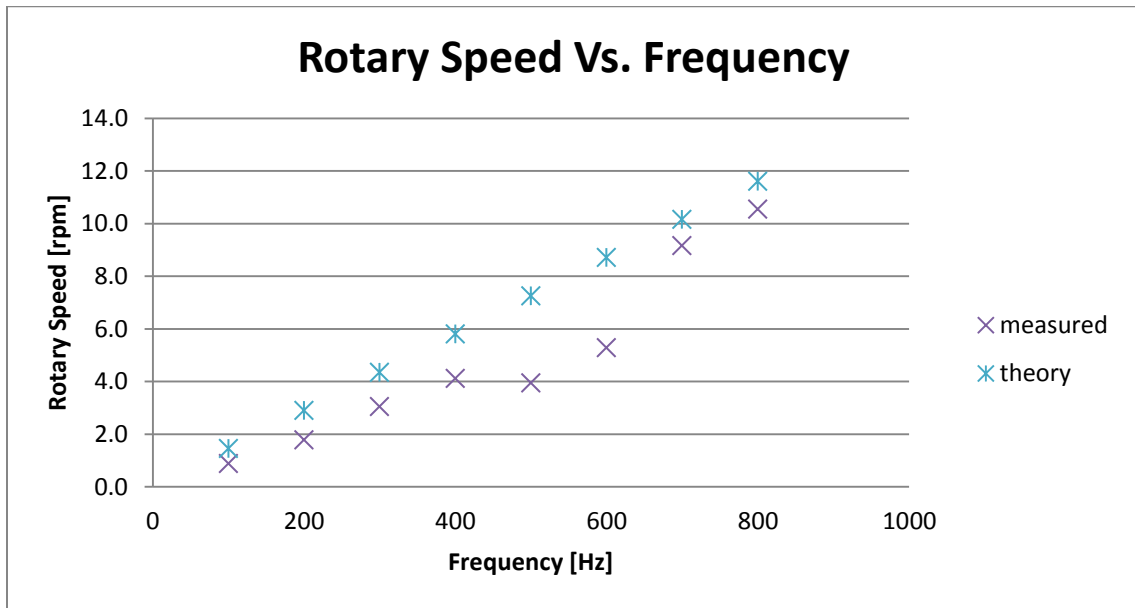


Fig. 5.14: No load rotary speed vs. Frequency (theory and average)

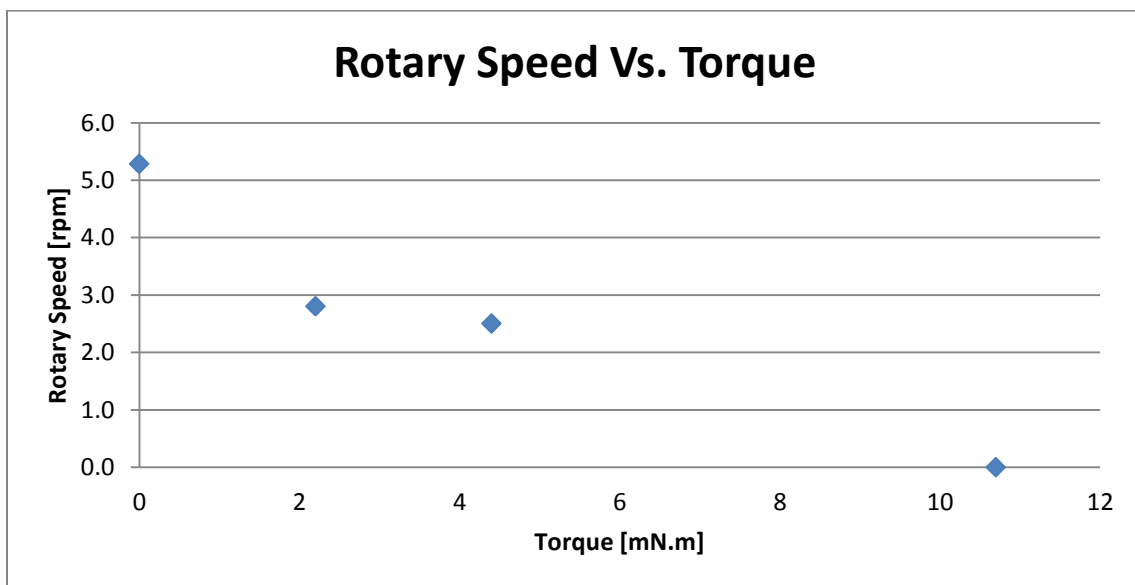


Fig. 5.15: Speed vs. Torque at frequency 600 Hz.

5.5 MR-Compatibility Tests & Results

The final step in validating the performance of the MR-Compatible actuator is to test it in this MR environment. Passive and active tests were conducted as presented in the following section.

5.5.1 Experimental Setup and methods

The experimental setup using a phantom and the linear-rotary actuator for the image distortion quality experiment which was performed in 3T MRI system (Siemens Tim Trio, software version VB17A). The actuator was placed in the middle of the phantom which in turn was placed in the isocenter of the magnet. The actuator was tested according to the GE and a TSE scan sequence presented in Table 5.4.

Table 5.4: Scan Sequences

| Sequence ID | G1 | T1 | T2 |
|------------------------|-----------|-----------|-----------|
| Sequence Type | GE | TSE | TSE |
| TR (ms) | 1250 | 1500 | 1500 |
| TE (ms) | 4.38 | 16 | 15 |
| Flip angle (deg) | 50 | 180 | 180 |
| Field of view (mm) | 400 x 400 | 400 x 400 | 400 x 400 |
| Matrix size (px) | 256 x 192 | 256 x 224 | 256 x 224 |
| Section thickness (mm) | 3 | 3 | 15 |
| Bandwidth (Hz/Px) | 400 | 300 | 781 |
| Imaging plane | Coronal | Coronal | Coronal |
| No. of slices | 20 | 20 | 20 |
| Imaging time (mm:ss) | 4:02 | 0:51 | 0:51 |

The second TSE scan was used when the actuator was active and was chosen as a worst case scan sequence in terms of image distortion. Tables 5.5 and 5.6 show the images for each set of tests at three slices of the phantom: top, middle and bottom. The sequences G1 and T1 were run first without the actuator present in order to get a baseline image. Then

the sequences were run with the actuator on the top of the phantom to see the maximum distortion due to the actuator. The actuator was then put in a more clinically-relevant position which was at the side of the phantom (bottom of the images) and the G1 and T1 sequences were run. The final test was with the extension piezostack excited sinusoidally during image acquisition. A variety of combinations of piezostack excitation frequencies and TSE sequence bandwidths were tried and the worst case was the excitation of 500 Hz with the T2 sequence.

Table 5.5: Tests with G1 Sequence

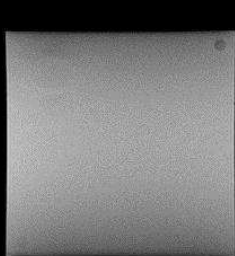
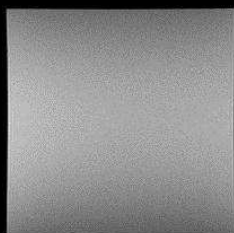
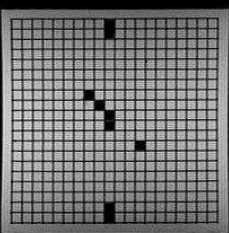
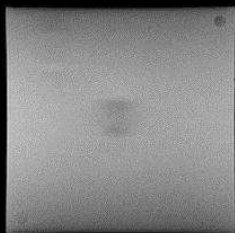

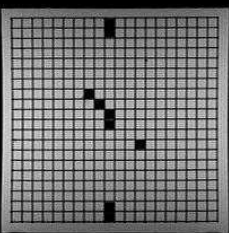
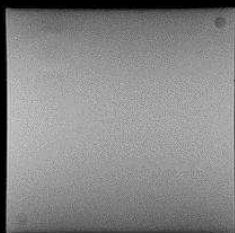
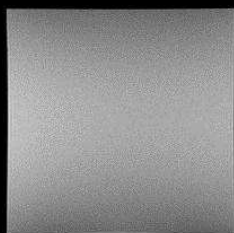
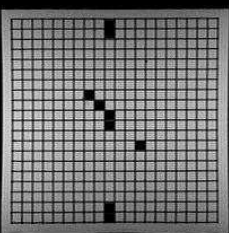
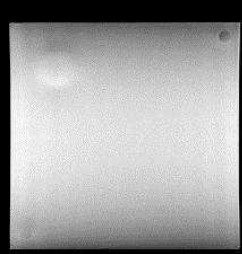
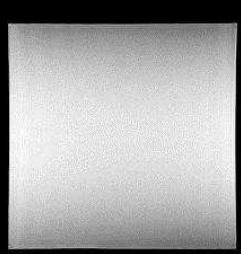
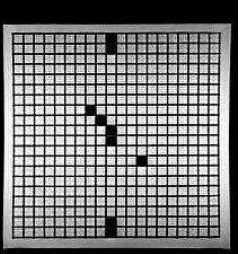
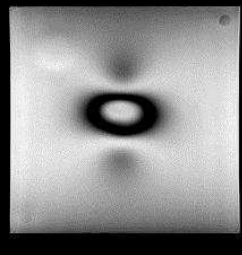
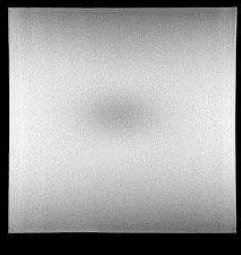
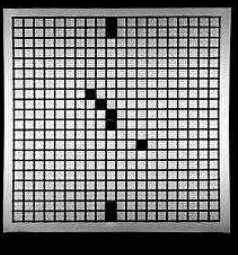
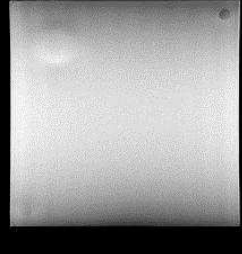
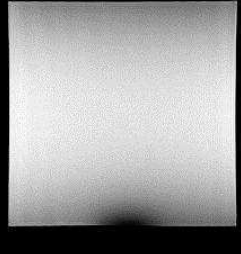
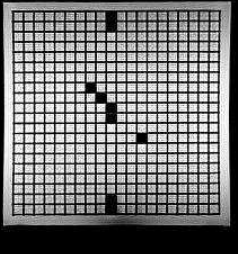
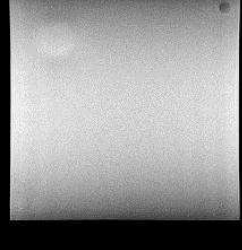

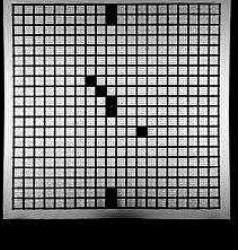
| Actuator Position | Phantom Slice Location | | |
|-----------------------------|---|--|---|
| | Top | Middle | Bottom |
| no actuator |  |  |  |
| actuator on top of phantom |  |  |  |
| actuator at side of phantom |  |  |  |

Table 5.6: Tests with T1 and T2 Sequences

| Actuator Position | Phantom Slice Location | | |
|--|---|--|---|
| | Top | Middle | Bottom |
| no actuator T1 |  |  |  |
| actuator on top of phantom T1 |  |  |  |
| actuator at side of phantom T1 |  |  |  |
| actuator at side of phantom-active T2 |  |  |  |

5.6 Results and Discussion

The images for the GE sequence show the actuator is essentially invisible with only a minor effect with the actuator on top of the phantom. The TSE scan was more sensitive to the actuator's presence as some dropout can be seen in a small area around the actuator. Note that unlike the previous tests on the metallic cylinders, the actuator does not distort

the image as can be seen when viewing the grid. This would be important in positioning accuracy of the needle. The actuator did not show an increase in the dropout region when the piezostack was being excited. The actuator design has shown good promise and in the future work, it will be assessed for performance while running in the MRI.

5. 7 Summary & Conclusion

An MRI compatible actuator based on inchworm principle was designed and manufactured. The actuator is capable rotary and linear motion combined and independent. Force and torque characteristics of the motor were shown in the experiment with the simulation results. The actuator achieved designed parameters of linear speed 5.4 mm/s, rotary speed 10.5 rpm, Force 5.8 N, and torques 10.7 N.mm. MRI compatibility tests, showed no interaction between the actuator and magnetic field when tested passively, but showed an acceptable image quality when tested actively due to wiring noise which can be eliminated by proper filtering. This device can be used for needle medical procedure under MRI guidance for improvement of insertion accuracy.

Chapter 6

Summary and Future Work

6.1 Summary

Research for developing MR-compatible actuators is an emerging trend in image guided interventions and minimally invasive surgery procedures due to its benefits in post-surgery recovery and overall patient health. Many attempts were made to reach the goal of compactness in size and a high load capacity actuator to work deep inside the scanner bore but unfortunately methods of actuation attempted such as pneumatic, hydraulic, manual, and etc. lacks enough stiffness, compactness, and safety to achieve this goal. This work focuses on designing and testing a MR-compatible actuator for medical intervention with high precision in MRI environment. In addition, this work concentrates on designing a two degree of freedom actuator for needle procedures and integrating all components to be employed safely inside this challenging environment.

While most of the previous work the research was concentrated on either single degree of freedom [16-21] or low load and low torque capacity actuators [69-72]. The benefit of the current design is the compactness and the employment of magnetically inert material, which makes the actuator highly maneuverable and with minimum image distortion in this restricted space of the scanner bore. There were several challenges encountered in this

work, for example the issue of material MR-compatibility versus its mechanical properties such as strength, hardness and stiffness which was addressed by conducting MR-compatibility testing of the proposed materials. Also, proper alignment of the actuator components was a major factor in improving the performance of the device, so the design accommodated fine tuning components to rectify any misalignment might occur within a small range manufacturing tolerances. The development of MR-compatible actuator was carried out in the following highlighted steps:

- Testing of MR-compatible material for image distortion – In this step the research of quantitative comparison of engineering materials in the MRI was conducted, and a comparison to theoretical behavior was made in order to provide a rough estimate of the expected MRI performance before the expensive and time-consuming steps of construction and testing the device. The specific focus of this testing was on the effects in the MRI due to the material susceptibility alone, namely the force and the image artifacts. Experiments were performed on slender cylinders of twelve common metals as they can be easily modeled in the theoretical analysis. The result of this step was categorizing the MR-compatible material according to their image distortion effect, induced magnetic force and torque vs. their mechanical properties.
- Testing MR-compatible material for induced heat – An analytical technique was developed and validated to estimate the heating of metallic rods by MRI gradient fields which aid in developing of MR-compatible devices before testing in MRI environment. Heat induced due to material resistivity, permittivity, and the depth of penetration of the AC signal from the surface of the component was presented for 12 engineering materials samples. Results from this step were the estimation of orientation and geometry parameters of the slender cylinder for minimum induced heat in the magnetic environment.

- Development of the actuator concept and stress analysis – Four piezoelectric actuators stacks were employed in this piezoworm configuration to produce linear and rotary motions. The NU clamp and NC clamp were intentionally created asymmetric in design to provide different clamping forces for the maximum load capacity and torque at all instances.

Choosing a material that has minimum interaction with magnetic field was considered (all components were manufactured from beryllium copper), but the tradeoff between stiffness, strength and size compactness was realized by configuring the appropriate geometry parameters for the clamps and extender.

In this step, the stiffness of the clamps and the extender were estimated. The stiffness of the complementary clamps was based on the maximum load capacity of the actuator and extender stiffness was based on the maximum possible extension while keeping sufficient preload on the piezostack. Preload was considered in the calculations to prevent permanent deformation of the flexures while keeping all operational stresses below the yield stress but the main calculation criteria was fatigue limits for beryllium copper.

The design of the flexure was optimized using FEA for compactness in size and maximum fatigue endurance. The aim of this analysis was to reduce size of the actuator for optimal maneuverability inside the scanner bore.

- Actuator fabrication, and performance assessment – High accuracy was a foremost objective in the fabrication process. To achieve this goal EDM machining techniques were used in fabricating the extender and the clamps flexures. The sliding shaft was manufactured using centerless grinding techniques to achieve maximum roundness and straightness. For maximum alignment the supporting clamps were machined to a very close tolerance to the

shaft diameter and adjusting set screws designed for fine tune any slack in the fit. The developed device have an infinite linear motion and rotary motion, the linear motion only restricted by the shaft length which in this case is 80 mm with resolution accuracy of 20 nm. The actuator have a load capacity of 6 N, and has a torque capacity of 10.7 N.mm, , linear speed of 5.4 mm/s, rotary speed of 10.5 rpm compared to the design values of load capacity of 13 N, and has a torque capacity of 22 N.mm, , linear speed of 9.8 mm/s, rotary speed of 11.5 rpm. The overall dimensions of the finished stage were 57.5 mm (length) × 30 mm (width) × 37.5 mm (height).

6.2 Future Work

The future work will be aimed towards testing the performance MR-compatible actuator in from a passive and active point of view inside the MRI environment. Active testing will include using filtering techniques to filter out interference generated from power equipment and connecting cables on the image quality of the scanner. Further performance testing of the actuator such as load, torque capacity, speeds will be conducting inside the MR environment then compared to the performance results outside the magnetic environment.

The other goal is to develop a closed-loop system to accurately track surgical tools as a part of an image guided system, and in order to realize the required accuracy nonlinear parameters such as friction in the contacting surfaces of the shaft and the clamps, hysteresis in piezoelectric stacks has to be addressed. The friction is considered to be non-linear in nature as it changes along the length of the travel of the shaft due to manufacturing tolerances and the dynamic effect on the clamps motion.

This high precision positioning system of the shaft and hence the surgical tools can be achieved by utilizing the MRI signal to serve as feedback of the closed-loop system, this can be also investigated.

In the current work the use of the shaft as the moving component was to simulate the needle used in the medical procedure and as was mentioned before this was a proof of concept prototype. In future work the actual actuator will be optimized for minimum size and maximum force output and speed. Furthermore, forces will be reanalyzed to accommodate for the hollow structure of the needle and proper mounting components.

The resonance frequency issue of the actuator will be visited and experimental resonance frequency measures will be conducted to obtain the exact resonance frequency. The rotating plate mechanism will be modified on the idea of torsional torque instead of linear flexing mechanism for higher rigidity and hence higher resonance frequency for the whole system which will increase the dynamic performance at the maximum working frequency of the signal amplifier.

Finally, integrating the actuator to an MR-compatible manipulator will be considered for remote manipulation of the device deep inside the scanner bore.

References

- [1] S. P. Dimaio, S. Pieper, K. Chinzei, N. Hata, S. J. Haker, D. F. Kacher, G. Fichtinger, C. M. Tempany, and R. Kikinis, "Robot-assisted needle placement in open MRI: System architecture, integration and validation," *Computer Aided Surgery* vol. 12, no. 1, 2007: 15-24.
- [2] N. V. Tsekos, A. Khanicheh, E. Christoforou, and C. Mavroidis, "Magnetic resonance-compatible robotic and mechatronics systems for image-guided interventions and rehabilitation: a review study," *Annual Rev. Biomed. Eng.*, vol. 9, 2007: 14.1-14.37.
- [3] T. K. Podder, D. P. Clark, D. Fuller, J. Sherman, W. S. Ng, L. Liao, D. J. Rubens, J. G. Strang, E. M. Messing, Y. D. Zhang, and Y. Yu, "Effects of velocity modulation during surgical needle insertion", *Proceedings of the 2005 IEEE Engineering in Medicine and Biology 27th Annual Conference*, Shanghai, China, 2005: 5766-5770.
- [4] N. Abolhassani¹, R. Patel, and F. Ayazi, "Effects of different insertion methods on reducing needle deflection," *Proceedings of the 29th Annual International Conference of the IEEE EMBS*, Lyon, France, 2007: 491-494.
- [5] N. Abolhassani, R. Patel, M. Moallem, "Needle insertion into soft tissue: A survey," *Medical Engineering & Physics* vol. 29, 2007: 413-431.
- [6] N. Abolhassani, R. Patel, F. Ayazi, "Needle control along desired tracks in robotic prostate brachytherapy," *IEEE International Conference on Systems Man and Cybernetics*, 2007: 3361-3366.
- [7] N. Yu, R. Riener, "Review on MR-compatible robotic systems," *IEEE/RAS-EMBS International Conference on Biomedical Robotics and Biomechatronics*, 2006:661-665.
- [8] H. Graf, G. Steidle, and F. Schick, "Heating of metallic implants and instruments induced by gradient switching in a 1.5-tesla whole-body unit," *Journal of Magnetic Resonance Imaging*, vol. 26, 2007: 1328-1333.
- [9] M. K. Konings, L. W. Bartels, H. F. M. Smits, and C. J. G. Bakker, "Heating around intravascular guidewires by resonating RF waves", *Journal of Magnetic Resonance Imaging*, vol. 12, 2000: 79-85.
- [10] R. Buchli, P. Boesiger, D. Meier, "Heating effects of metallic implants by MRI examinations," *Magnetic Resonance in Medicine*, vol. 7, 1988: 255-261.
- [11] J. F. Schenck, "Invited safety of strong, static magnetic fields," *Journal of Magnetic Resonance Imaging*, vol. 12, 2000: 2-19.
- [12] K. Chinzei, R. Kikinis, and F.A. Jolesz, "MR compatibility of mechatronic devices: design criteria," *Int. Conf. Med Image Computer Assist. Interv.* , 1999: 1020-1031.
- [13] (2012, October) U. S. FDA, "A primer on medical device interactions with magnetic resonance imaging systems," 1997. [Online]. Available: <http://www.fda.gov/MedicalDevices/DeviceRegulationandGuidance/GuidanceDocuments/ucm107721.htm>.

- [14] Nikolaos V. Tsekos, Alpay Özcan, and Eftychios Christoforou, "A Prototype Manipulator for Magnetic Resonance-Guided Interventions inside Standard Cylindrical Magnetic Resonance Imaging Scanners," *Biomechanical Engineering*, vol. 127 no. 6, 2005: 972–980.
- [15] J. F. Schenck, "The role of magnetic susceptibility in magnetic resonance imaging: MRI magnetic compatibility of the first and second kinds," *Med. Phys.*, vol. 23, 2005: 815–850.
- [16] Kim D, Kobayashi E, Dohi T, Sakuma I, "A new, compact MR-compatible surgical manipulator for minimally invasive liver surgery", *Medical Image Computing and Computer-Assisted Intervention — MICCAI 2002. Lecture Notes in Computer Science*, Vol. 2488, 2002: 99-106.
- [17] Roger Gassert, Roland Moser, Etienne Burdet, and Hannes Bleuler, "MRI/fMRI-Compatible Robotic System with Force Feedback for Interaction With Human Motion", *IEEE/ASME Transactions on Mechatronics*, vol. 11, no. 2, 2006: 216 - 224.
- [18] Moser R, Gassert R, Burdet E, Sacher L, Woodtli HR, et al, "An MR compatible robot technology" *Proc. IEEE Int. Conf. Robotics Automation*, 2003: 670–675.
- [19] Dan Stoianovici, Alexandru Patriciu, Dumitru Mazilu and Louis Kavoussi, "A New Type of Motor: Pneumatic Step Motor", *IEEE/ASME Trans. On mechatronics*, vol. 12, no. 1, 2007: 98 - 106.
- [20] Dan Stoianovici, Danny Song, Doru Petrisor, Daniel Ursu, Dumitru Mazilu, Michael Mutener, Michael Schar & Alexandru Patriciu, "MRI Stealth robot for prostate interventions", *Minimally Invasive Therapy*, vol. 16, no. 4, 2007: 241–248.
- [21] (2012, October) The James Buchanan Brady Urological Institute. [Online], Available: <http://urobotics.urology.jhu.edu/projects/MrBot/index.php>.
- [22] Elhawary H, Zivanovic A, Rea M, Tse ZT, McRobbie D, Young I, Paley M, Davies B, Lampérth M "A MR compatible mechatronic system to facilitate magic angle experiments in vivo", *Medical Image Computing and Computer-Assisted Intervention – MICCAI 2007. Lecture Notes in Computer Science*, Vol. 4792, 2007: 604-611.
- [23] Zion Tsz Ho Tse, Haytham Elhawary, Aleksandar Zivanovic, Marc Rea, Martyn Paley, Graeme Bydder, Brian L. Davies, Ian Young, and Michael U. Lampérth, "A 3-DOF MR-Compatible Device for Magic Angle Related In Vivo experiments", *IEEE/ASME Transactions on Mechatronics*, vol. 13, no. 3, : 316 - 324.
- [24] Chinzei K, Miller K, "MRI guided surgical robot" *Australian Conf. Robotics Automation*, 2001: 50–55.
- [25] Koseki Y et al, "Endoscope manipulator for trans-nasal neurosurgery, optimized for and compatible to vertical field open MRI", *Proc. Med. Image Comput. Comput.-Assisted Intervention*, 2002: 114–121.
- [26] E. Hempel, H. Fischer, L. Gumb, T. Hohn, H. Krause, U. Voges, H. Breitwieser, B. Gutmann, J. Durke, M. Bock, and A. Melzer, "An MRI-compatible surgical robot for precise radiological interventions," *Computer Aided Surgery*, vol. 8, 2003: 180–191.

- [27] Kenji Uchino, "Piezoelectric ultrasonic motors: overview", *Smart Materials and Structures*. vol.7, no 3, 1998: 273–285.
- [28] (2012, October) Shinsei corporation. [Online]. Available: http://www.shinsei-motor.com/English/techno/ultrasonic_motor.html.
- [29] H. Elhawary, A. Zivanovic, M. Rea, B. Davies, C. Besant, D. McRobbie, N. de Souza, I. Young, and M. Lampérth, "The Feasibility of MR-Image Guided Prostate Biopsy Using Piezoceramic Motors Inside or Near to the Magnet Isocentre", *Proceedings of the 9th international conference on Medical Image Computing and Computer-Assisted Intervention*, vol. Part I, 2006: 519-26.
- [30] H. Elhawary, A. R Zivanovic, M. Rea, B. Davies, C. Besant, D. Mcrobbie, N. M. Desouza, I. Young, and M. U. Lampe´rth, "A Modular Approach to MRI-Compatible Robotics", *Engineering in Medicine and Biology Magazine, IEEE*, vol. 27 , no. 3, 2008: 35 - 41.
- [31] A. Krieger, R. C. Susil, C. Ménard, J. A. Coleman, G. Fichtinger, and Ergin Atalar, and L. L. Whitcomb, "Design of a Novel MRI Compatible Manipulator for Image Guided Prostate Interventions", *IEEE Transactions on Biomedical Engineering*, vol. 52, no. 2, 2005: 306 – 313.
- [32] R. Gassert, A. Yamamoto, D. Chapuis, L. Dovat, H. Bleuler, E. Burdet, "Actuation methods for applications in MR environments", *Concepts in Magnetic Resonance Part B: Magnetic Resonance Engineering*, vol. 29B, no. 4, 2006: 191–209.
- [33] Yamamoto A, Ichiyanagi K, Higuchi T, Imamizu H, Gassert R, Ingold M, Sache L and Blueler H., "Evaluation of MR compatibility of electrostatic linear motor." *Proc. IEEE International Conference on Robotics and Automation, (ICRA)*: 3658–3663.
- [34] Niino T, Egawa S, Higuchi T. 1995. "Dual excitation multiphase electrostatic drive." *Proc. IEEE Industry Applications Society Annual Meeting (IAS)*: 1318–1325.
- [35] Vogan J., et al, "Manipulation in MRI devices using electrostrictive polymer actuators: with an application to reconfigurable imaging coils", *Proc. IEEE Int. Conf. Robotics Automation*, 2004: 2498–504.
- [36] F. Carpi, A. Khanicheh, C. Mavroidis, and D. De Rossi, "MRI Compatibility of Silicone-Made Contractile Dielectric Elastomer Actuators", *IEEE/ASME Transactions on Mechatronics*, vol. 13, no. 3, 2008: 370-374.
- [37] T. Hemsel, J. Wallaschek, "Survey of the present state of the art of piezoelectric linear motors", *Ultrasonics*, vol. 38 , 2000: 37–40.
- [38] C. Borda, D. Arsene, M. Marinescu, A. Moraru, L. Butu, G. Arsene, "Study of the Present State of Ultrasonic Linear Motors", *SISOM 2008 and Session of the Commission of Acoustics*, 2008: 399-403.
- [39] T. Pandell and E. Garcia, "Design of a Piezoelectric Caterpillar Motor," *proceeding of 1996 ASME International Mechanical Engineering Congress and Exposition ARE*, vol. 52, 1996: 627-648.
- [40] Rainer Gloss, Harry Marth, "Adjusting Device with Piezo Drive," *US Patent 5 424 597*, Jun. 13, 1995.

- [41] Safari, Ahmad; Akdogan, E. Koray (Eds.), "Piezoelectric and Acoustic Materials for Transducer Applications", 2008 Springer Science+Business Media, LLC, ISBN: 978-0-387-76538-9, chapter2.
- [42] (2012, October) PI (Physik Instrumente) GmbH & Co. KG. [Online]. Available: http://www.physikinstrumente.com/en/pdf_extra/2009_PI_Piezo_University_Designing_with_Piezo_Actuators_Tutorial.pdf.
- [43] (2012, October) PI (Physik Instrumente) GmbH & Co. KG. [Online]. Available: <http://www.physikinstrumente.com/en/products/primages.php?sortnr=100810&picview=1#gallery>.
- [44] Bi Zhang and Zhenqi Zhu, "Developing a Linear Piezomotor with Nanometer Resolution and High Stiffness", IEEE/ASME Trans. On Mechatronics, vol. 2, no. 1, 1997: 22 - 29.
- [45] J. Li, R. Sedaghati, J. Dargahi and D. Waechter, "Design and development of a new piezoelectric linear Inchworm actuator", Mechatronics, vol. 15, 2005 : 651–681.
- [46] Murata T. Drive Apparatus and Motor Unit. Patent #4,947,077, 1990.
- [47] Park J, Keller S, Carman GP, Hahn HT, "Development of a compact is placement accumulation actuator device for both large force and large displacement", Sensors Actuators, vol. 90, 2001:191–202.
- [48] T. Galantea, J. Frankb, J. Bernardb, W Chen", G. A. Lesieutre', and G. H. Koopmannb , "Design, Modeling, and Performance of a High Force Piezoelectric Inchworm Motor", Smart Structures and Materials 1998: Smart Structures and Integrated Systems, 1998: 756-767.
- [49] K. Hsu, and A. Biatter, "Transducer", US. Patent: 3,292,019, 1966.
- [50] L. Locher, "Micrometric linear actuator", US. Patent: 3,296,467, 1967.
- [51] A.D. Brisbane, "Position control device", US. Patent: 3,377,489, 1968.
- [52] .V. Galutva, "Device for precision displacement of a solid body", US. Patent. 3,684, 904 1972.
- [53] W. May Jr., "Piezoelectric Electromechanical Translation Apparatus," US Patent 3 902 084, Aug. 26, 1975.
- [54] P. Tenzer and R. Ben Mrad, "A Systematic Procedure for the Design Piezoelectric Inchworm Precision Positioners," IEEE/ASME Transactions on Mechatronics, vol. 9, no. 2, 2004: 427-435.
- [55] Quanfang Chen, Da-Jeng Yao, Chang-Jin Kim and Carman, G.P., "Mesoscale actuator device with micro interlocking mechanism," Proceedings, The Eleventh Annual International Workshop on Micro Electro Mechanical Systems, 1998: 384-389.
- [56] J. Park, G. P. Carman and H. T. Hahn, " Design and Testing of a Mesoscale Piezoelectric Inchworm Actuator with Microridges", Journal of Intelligent Material Systems and Structures, vol. 11, 2000: 671 - 684.
- [57] P.E. Tenzer, R. Ben Mrad, "On amplification in inchworm precision positioners", Mechatronics, vol. 14, 2004: 515–531.
- [58] K. Kwon, N. Cho, W. Jang, "The Design and Characterization of a Piezo-Driven Inchworm Linear Motor with a Reduction-Lever Mechanism", JSME International

Journal Series C Mechanical Systems, Machine Elements and Manufacturing, vol. 47, no. 3, 2004: 803-811.

- [59] K. Ohnishi, M. Umeda, M. Kurosawa, and S. Ueha, "Rotary Inchworm-Type Piezoelectric Actuator", *Electrical Engineering in Japan*, vol. 110, no. 3, 1990: 107-109.
- [60] T. Morita, R. Yoshida, Y. Okamoto, M. K. Kurosawa, and T. Higuchi, "A Smooth Impact Rotation Motor Using a Multi-Layered Torsional Piezoelectric Actuator", *IEEE transactions on ultrasonics, ferroelectrics, and frequency control*, vol. 46, no. 6, 1999: 1439-1445.
- [61] J. Oliver, R. Neurogaonkar, J. Nelson and C. Bertolini, "Rotary Piezoelectric Motor for Vehicle Applications," US Patent 5 780 956, Jul. 14, 1998.
- [62] T. Fujimoto, "Piezo-electric actuator and stepping device ", US. Patent. 4, 714,855 1987.S.
- [63] D. Khanh, G. Ephraim, "Development of a rotary inchworm piezoelectric motor", *Proc. SPIE 2443, Smart Structures and Materials 1995: Smart Structures and Integrated Systems*, vol. 2443, 1995: 782-788.
- [64] J. Liu, Z. Yang, P. Zeng, Z. Fan, "Study on precision piezoelectric rotary step motors with inner anchor/loosen and outer drive", *Front. Electr. Electron. Eng. China*, vol. 3, no. 3, 2008: 364–369.
- [65] Gursan, Selcuk, Stepanenko, Yury, Dost, Sadik, Piezoelectric Rotary Positioner, WIPO Patent Application WO 98/018169, 1998.
- [66] K. Mori, "Piezoelectric Rotary Actuator," US Patent 4 468 583, Aug. 28, 1984.
- [67] Sang-Chae Kim, and Soo Hyun Kim, "Precise rotary motor by inchworm motion using dual wrap belts", *Review of Scientific Instruments*, vol. 70, no. 5, 1999: 2546-2550.
- [68] C.W. Staufenberg, Jr., and R.J. Hubbell, "Piezoelectric electromechanical translation apparatus", US. Patent. 4, 622, 483, 1986.
- [69] T. Mashimo, S. Toyama, and H. Matsuda, "Development of Rotary-Linear Piezoelectric Actuator for MRI Compatible Manipulator," *IEEE/RSJ International Conference on Intelligent Robots and Systems*, 2008: 113 – 118.
- [70] T. Mashimo, and S. Toyama, "Rotary-Linear Piezoelectric Actuator Using a Single Stator", *IEEE Transactions on Ultrasonics, Ferroelectrics, and Frequency Control*, vol. 56, no. 1, 2009: 114-120.
- [71] T. Mashimo, and S. Toyama, " Rotary-Linear Piezoelectric Microactuator With a Cubic Stator of Side Length 3.5 mm", *IEEE Transactions on Ultrasonics, Ferroelectrics, and Frequency Control*, vol. 57, no. 8, 2010: 1825 – 1830.
- [72] H. Su, W. Shang, G. A. Cole, K. Harrington, G. S. Fischer, "Haptic System Design for MRI-Guided Needle Based Prostate Brachytherapy", *IEEE Haptics Symposium*, 2010: 483-488.
- [73] G. Schaefers, "Testing MR safety and compatibility," *Engineering in Medicine and Biology Magazine, IEEE*, vol. 27, no. 3, 2008: 23 –27.

- [74] N. Yu, R. Gassert, and R. Riener, "Mutual interferences and design principles for mechatronic devices in magnetic resonance imaging." *International journal of computer assisted radiology and surgery*, vol. 6, no. 4, 2011: 473–488.
- [75] U.-X. Tan, B. Yang, R. Gullapalli, and J. Desai, "Design and development of a 3-axis MRI-compatible force sensor," in *Robotics and Automation (ICRA), 2010 IEEE International Conference on*, 2010: 2586–2591.
- [76] A. Goldenberg, J. Trachtenberg, W. Kucharczyk, Y. Yi, M. Haider, L. Ma, R. Weersink, and C. Raoufi, "Robotic system for closed bore MRI-guided prostatic interventions," *Mechatronics, IEEE/ASME Transactions on*, vol. 13, no. 3, 2008: 374–379.
- [77] G. Fischer, I. Iordachita, C. Csoma, J. Tokuda, S. DiMaio, C. Tempany, N. Hata, and G. Fichtinger, "MRI-compatible pneumatic robot for transperineal prostate needle placement," *Mechatronics, IEEE/ASME Transactions on*, vol. 13, no. 3, 2008: 295–305.
- [78] N. Yu, C. Hollnagel, A. Blickenstorfer, S. Kollias, and R. Riener, "Comparison of MRI-compatible mechatronic systems with hydrodynamic and pneumatic actuation," *Mechatronics, IEEE/ASME Transactions on*, vol. 13, no. 3, 2008: 268–277.
- [79] Y. Wang, G. Cole, H. Su, J. Pilitsis, and G. Fischer, "MRI compatibility evaluation of a piezoelectric actuator system for a neural interventional robot," in *Engineering in Medicine and Biology Society, 2009. EMBC 2009. Annual International Conference of the IEEE*, Sept. 2009: 6072–6075.
- [80] G. J. Adams, U. Baltazar, C. Karmonik, C. Bordelon, P. H. Lin, R. L. Bush, A. B. Lumsden, and J. D. Morrisett, "Comparison of 15 different stents in superficial femoral arteries by high resolution MRI ex vivo and in vivo," *Journal of Magnetic Resonance Imaging*, vol. 22, no. 1, 2005 : 125–135.
- [81] Z. T. H. Tse, H. Elhawary, C. A. F. Montesinos, M. Rea, I. Young, and M. Lamperth, "Testing MR image artifacts generated by engineering materials," *Concepts in Magnetic Resonance Part B: Magnetic Resonance Engineering*, vol. 39B, no. 2, 2011 : 109–117.
- [82] R. Salomir, B. D. de Senneville, and C. T. Moonen, "A fast calculation method for magnetic field inhomogeneity due to an arbitrary distribution of bulk susceptibility," *Concepts in Magnetic Resonance Part B: Magnetic Resonance Engineering*, vol. 19B, no. 12003: 26–34.
- [83] K. Koch, B. Hargreaves, K. B. Pauly, W. Chen, G. Gold, and K. King, "Magnetic resonance imaging near metal implants," *Journal of Magnetic Resonance Imaging*, vol. 32, no. 4, 2010: 773–787.
- [84] K. M. Koch, X. Papademetris, D. L. Rothman, and R. A. de Graaf, "Rapid calculations of susceptibility-induced magnetostatic field perturbations for in vivo magnetic resonance," *Physics in Medicine and Biology*, vol. 51, no. 24, 2006: 6381-6402.

- [85] S. Balac and G. Caloz, "Mathematical modeling and numerical simulation of magnetic susceptibility artifacts in magnetic resonance imaging," *Computer Methods in Biomechanics and Biomedical Engineering*, vol. 3, no. 4, 2000: 335–349.
- [86] J. S. Lewin, J. L. Duerk, V. R. Jain, C. A. Petersilge, C. P. Chao, and J. R. Haaga, "Needle localization in MR-guided biopsy and aspiration: effects of field strength, sequence design, and magnetic field orientation." *American Journal of Roentgenology*, vol. 166, no. 6, 1996: 1337–1345.
- [87] B. M. Müller-Bierl, P. Martirosian, H. Graf, A. Boss, C. König, P. L. Pereira, and F. Schick, "Biopsy needle tips with markers—MR compatible needles for high-precision needle tip positioning," *Medical Physics*, vol. 35, no. 6, 2008: 2273–2278.
- [88] B. Müller-Bierl, H. Graf, U. Lauer, G. Steidle, and F. Schick, "Numerical modeling of needle tip artifacts in MR gradient echo imaging," *Medical Physics*, vol. 31, no. 3, 2004 679–687.
- [89] B. Müller-Bierl, H. Graf, G. Steidle, and F. Schick, "Compensation of magnetic field distortions from paramagnetic instruments by added diamagnetic material: Measurements and numerical simulations," *Medical Physics*, vol. 32, no. 1, 2005: 76–84.
- [90] F. G. Shellock, "Metallic surgical instruments for interventional MRI procedures: Evaluation of MR safety," *Journal of Magnetic Resonance Imaging*, vol. 13, 2001: 152–157.
- [91] M. J. G. Donald W. McRobbie, Elizabeth A. Moore and M. R. Prince, *MRI From Picture to Proton*, 2nd ed. Cambridge university press, 2006.
- [92] C. Moosbrugger and F. Cverna, Eds., *ASM Ready Reference: Electrical and Magnetic Properties of Metals*. Materials Park, Ohio: ASM International, 2000.
- [93] R. G. Budynas and K. Nisbett, *Shigley's Mechanical Engineering Design*, 8th ed. New York, NY: McGraw Hill, 2008.
- [94] F. R. Fickett, *Advances in Cryogenic Engineering Materials*, 8th ed. New York, NY: Plenum Press, vol. 38, 1992: 1191-1197.
- [95] J. Laporta, F. Parker, and R. Winter, "Magnetic properties of copper alloys," *PROC ASTM*, vol. 59, 1959: 230–261.
- [96] (2012, October) High temp metals data library. [Online]. Available: <http://www.hightempmetals.com/techdata/hitempMonelK500data.php>
- [97] Standard Test Method for Measurement of Magnetically Induced Displacement Force on Medical Devices in the Magnetic Resonance Environment, American Society for Testing and Materials (ASTM) International Std. F2052-06, 2006.
- [98] Mattei E, Calcagnini G, Censi F, Triventi M, Bartolini P. "Numerical Model for Estimating RF-Induced Heating on a Pacemaker Implant During MRI: Experimental Validation". *IEEE Transactions on Biomedical Engineering* vol. 57 no. 8, 2010: 2045-2052.

- [99] Nyenhuis JA, Park SM, Kamondetdacha R, Amjad A, Shellock FG, Rezai AR. "MRI and implanted medical devices: basic interactions with an emphasis on heating." *IEEE Transactions on Device and Materials Reliability* 2005;5:467- 480.
- [100] Park SM, Kamondetdacha R, Nyenhuis JA. "Calculation of MRI-induced heating of an implanted medical lead wire with an electric field transfer function". *Journal of Magnetic Resonance Imaging* vol. 26, 2007: 1278–1285.
- [101] Ibrahim TS, Tang L, Kangarlu A, Abraham R." Electromagnetic and modeling analyses of an implanted device at 3 and 7 Tesla." *Journal of Magnetic Resonance Imaging* vol. 26, 2007:1362–1367.
- [102] Nitz WR, Oppelt A, Renz W, Manke C, Lenhart M, Link J. "On the heating of linear conductive structures as guide wires and catheters in interventional MRI." *Journal of Magnetic Resonance Imaging* vol. 13, 2001: 105–114.
- [103] Liu CY, Farahani K, Lu DS, Duckwiler G., Oppelt A. "Safety of MRI-guided endovascular guidewire applications." *Journal of Magnetic Resonance Imaging* vol. 12, 2000: 75–78.
- [104] Shellock FG. "Radiofrequency energy-induced heating during MR procedures: a review." *Journal of Magnetic Resonance Imaging* vol. 12, 2000: 30–36.
- [105] Buechler DN, Durney CH, Christensen DA. , "Calculation of electric fields induced near metal implants by magnetic resonance imaging switched-gradient magnetic fields", *Journal Magnetic Resonance Imaging*, vol. 15, 1997: 1157–1166.
- [106] Reilly JP, Diamant AM., "Theoretical evaluation of peripheral nerve stimulation during MRI with an implanted spinal fusion stimulator", *Journal Magnetic Resonance Imaging*, vol. 15, 1997: 1145–1156.
- [107] Hartwell RC, Shellock FG., "MRI of cervical fixation devices: sensation of heating caused by vibration of metallic components", *Journal Magnetic Resonance Imaging*, vol. 7, 1997: 771–772.
- [108] Baker KB, Tkach JA, Nyenhuis JA, et al. , "Evaluation of specific absorption rate as a dosimeter of MRI-related implant heating. *Journal Magnetic Resonance Imaging*, vol. 20, 2004: 315–320.
- [109] Davies J, Simpson P. *Induction heating handbook*. New York: McGraw-Hill; 1979: 326.
- [110] Paulus JA, Richardson JS, Tucker RD, Park JB. "Evaluation of inductively heated ferromagnetic alloy implants for therapeutic interstitial hyperthermia." *IEEE Transactions on Biomedical Engineering*, vol. 43, 1996: 406-413.
- [111] Sanchez Lopez H, Poole M, Crozier S. "Eddy current simulation in thick cylinders of finite length induced by coils of arbitrary geometry." *Journal of Magnetic Resonance Imaging* vol. 207, 2010: 251-261.
- [112] Standard Test Method for Measurement of Radio Frequency Induced Heating On or Near Passive Implants during Magnetic Resonance Imaging, American Society for Testing and Materials (ASTM) International Std. F 2182 – 09, 2009.
- [113] COMSOL Multiphysics, version 3.4, COMSOL AB, 2007.
- [114] S. Salisbury, D. F. Waechter, R. Ben Mrad, S. E. Prasad, R. G. Blacow, and B. Yan, "Design considerations for complementary inchworm actuators," *IEEE/ASME Trans. on Mechatronics*, vol. 11, no. 3, 2006: 265-272.

- [115] S. Salisbury, R. Ben Mrad, D. Waechter and S. Prasad, "Design, modeling and closed loop control of a complementary clamp piezoworm actuator," IEEE/ASME Transactions on Mechatronics, vol. 14, no. 6, 2009: 724-732.
- [116] S. Salisbury, D. Waechter, R. Ben Mrad, R. Blacow, and E. Prasad, "Design Tools for Piezoelectric Actuated Inchworm Positioners," Proceedings of Smart Materials & Structures, CANSMART 2003, Montreal, Quebec, Canada, 2003: 169-175.
- [117] K. Elbannan, W. Handler, C. Wyenberg, B. Chronik and S. P. Salisbury, "Prediction of force and image artifacts under MRI for metals used in medical devices," IEEE/ASME Transactions on Mechatronics, 2012, submitted.
- [118] LABVIEW Real-Time, Version 9.0, National instruments Corp.
- [119] (2012, October) PI (Physik Instrumente) GmbH & Co. KG. [Online]. Available: http://www.physikinstrumente.com/en/pdf/E500_E501_Datasheet.pdf.

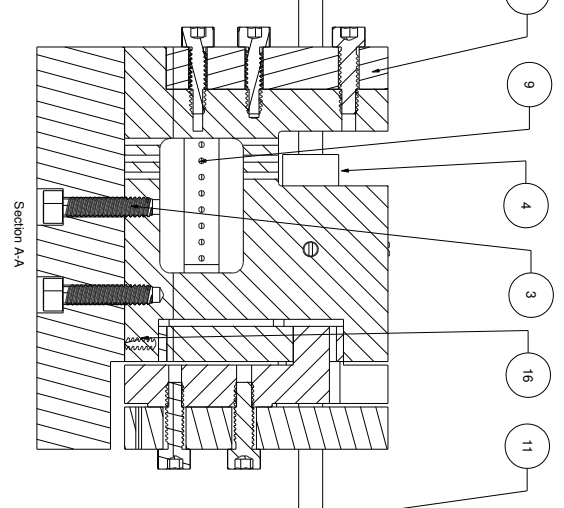
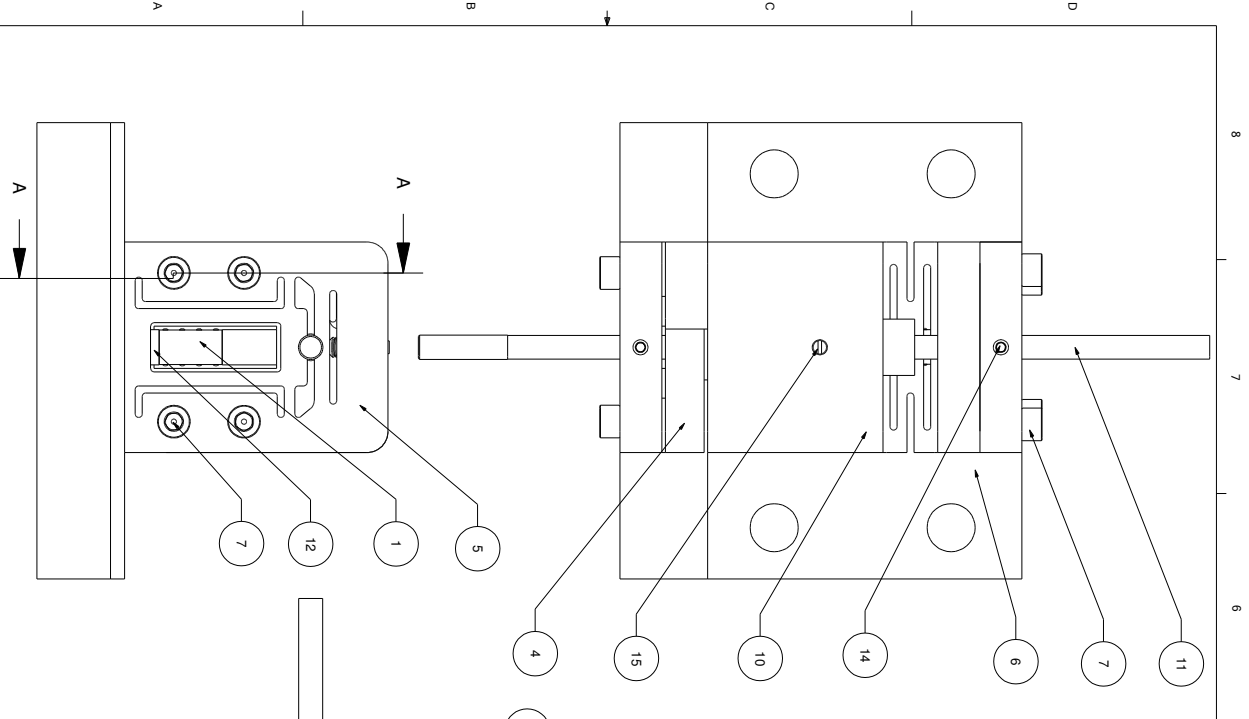
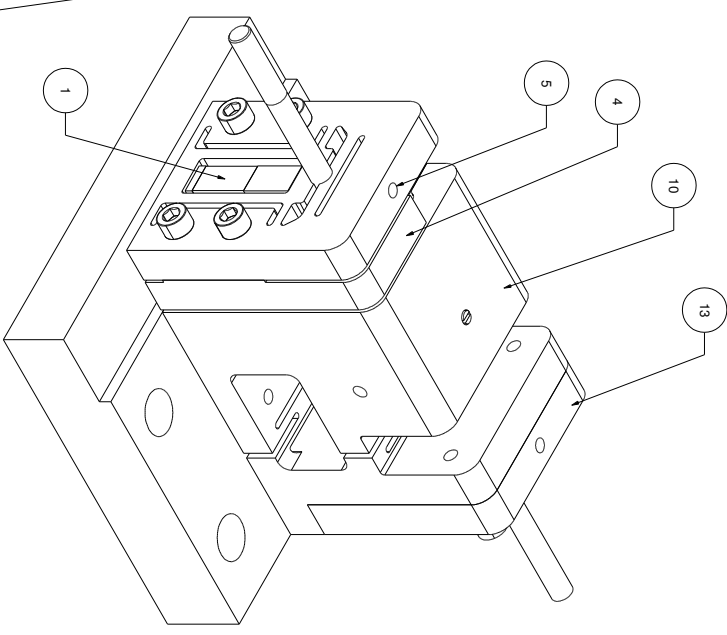
Appendix A

Drawings of Piezoworm MR-Compatible Actuator

| Item Num | Quantity | Part Num | Part Name |
|----------|----------|----------|------------------------|
| 1 | 2 | P885.10 | Small Piezo Actuator |
| 3 | 4 | 93465A11 | Large Brass Cap Screw |
| 4 | 1 | 3 | Rotating Plate |
| 5 | 1 | 4 | Complementary Clamp |
| 6 | 1 | 6 | Base Plate |
| 7 | 10 | 93465A10 | Small Brass Cap Screw |
| 9 | 2 | P885.50 | Large Piezo Actuator |
| 10 | 1 | 2 | Main Clamp |
| 11 | 1 | 7 | Shaft |
| 12 | 8 | 8 | Pressure Plate |
| 13 | 1 | 5 | Clamp |
| 14 | 4 | 92991A10 | Large Brass Set Screw |
| 15 | 3 | 95862A10 | Large Nylon Set Screw |
| 16 | 1 | 92991A10 | Medium Brass Set Screw |
| 17 | 1 | 92991A10 | Small Brass Set Screw |
| 18 | 1 | 95862A10 | Small Nylon Set Screw |

| REVISIONS | | | | |
|-----------|-----|---------------|----------|----------|
| ZONE | REV | DESCRIPTION | DATE | APPROVED |
| C | | FINAL RELEASE | 07-05-12 | |

| Item Number | Quantity | Part Number | Part Name |
|-------------|----------|-------------|------------------------|
| 1 | 2 | P885.10 | Small Piezo Actuator |
| 3 | 4 | 93465A110 | Large Brass Cap Screw |
| 4 | 1 | 3 | Rotating Plate |
| 5 | 1 | 4 | Complementary Clamp |
| 6 | 1 | 6 | Base Plate |
| 7 | 10 | 93465A108 | Small Brass Cap Screw |
| 9 | 2 | P885.50 | Large Piezo Actuator |
| 10 | 1 | 2 | Main Clamp |
| 11 | 1 | 7 | Shaft |
| 12 | 8 | 8 | Pressure Plate |
| 13 | 1 | 5 | Clamp |
| 14 | 4 | 92991A106 | Large Brass Set Screw |
| 15 | 3 | 95862A106 | Large Nylon Set Screw |
| 16 | 1 | 92991A105 | Medium Brass Set Screw |
| 17 | 1 | 92991A103 | Small Brass Set Screw |
| 18 | 1 | 95862A103 | Small Nylon Set Screw |



| | | |
|--|-----------------------------|------------------|
| MME Dept. WESTERN UNIVERSITY Khaled Elbanna keibanna@uwyo.ca | | NAME STUDENT# |
| Assembly | | TITLE: |
| DIMENSIONS ARE IN MM TOLERANCES: ANGULAR: ±1° ONE PLACE DECIMAL: ±0.1 TWO PLACE DECIMAL: ±0.01 | SIZE DWG. NO. B 1 | REV C |
| MATERIAL: Beryllium Cu H04 (C17510) FINISH: N/A | SCALE: 1.5:1 | SHEET 1 OF 11 |

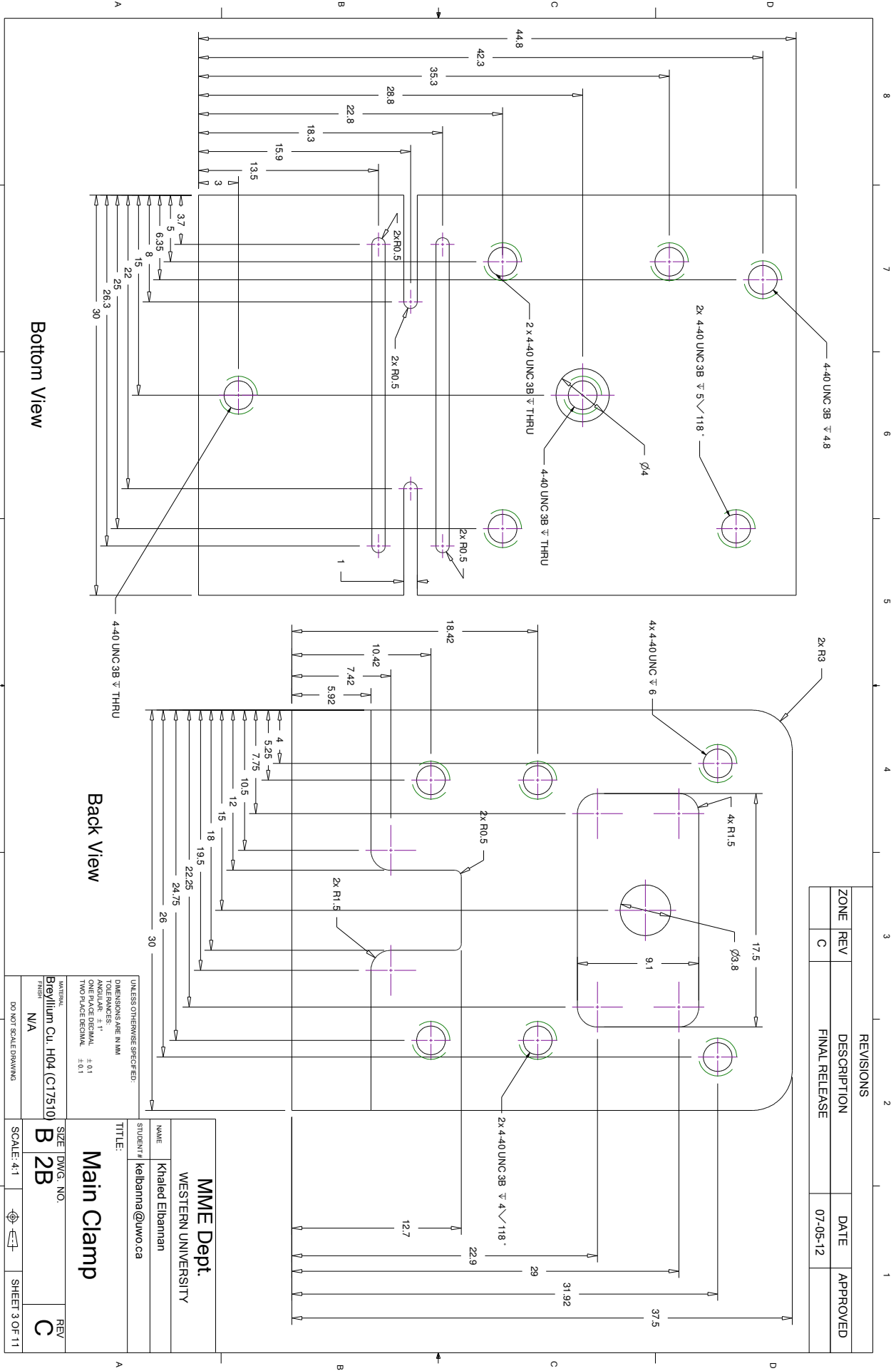
8 7 6 5 4 3 2 1

A B C D

Section A-A

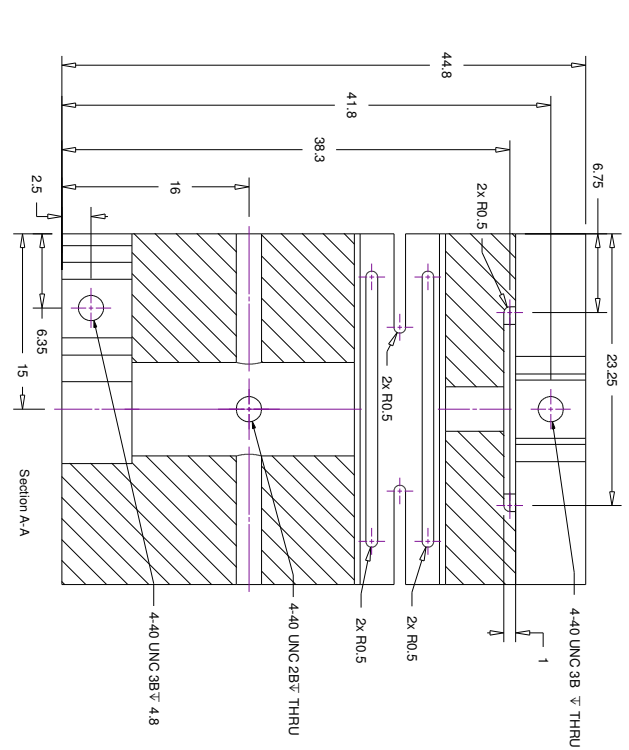
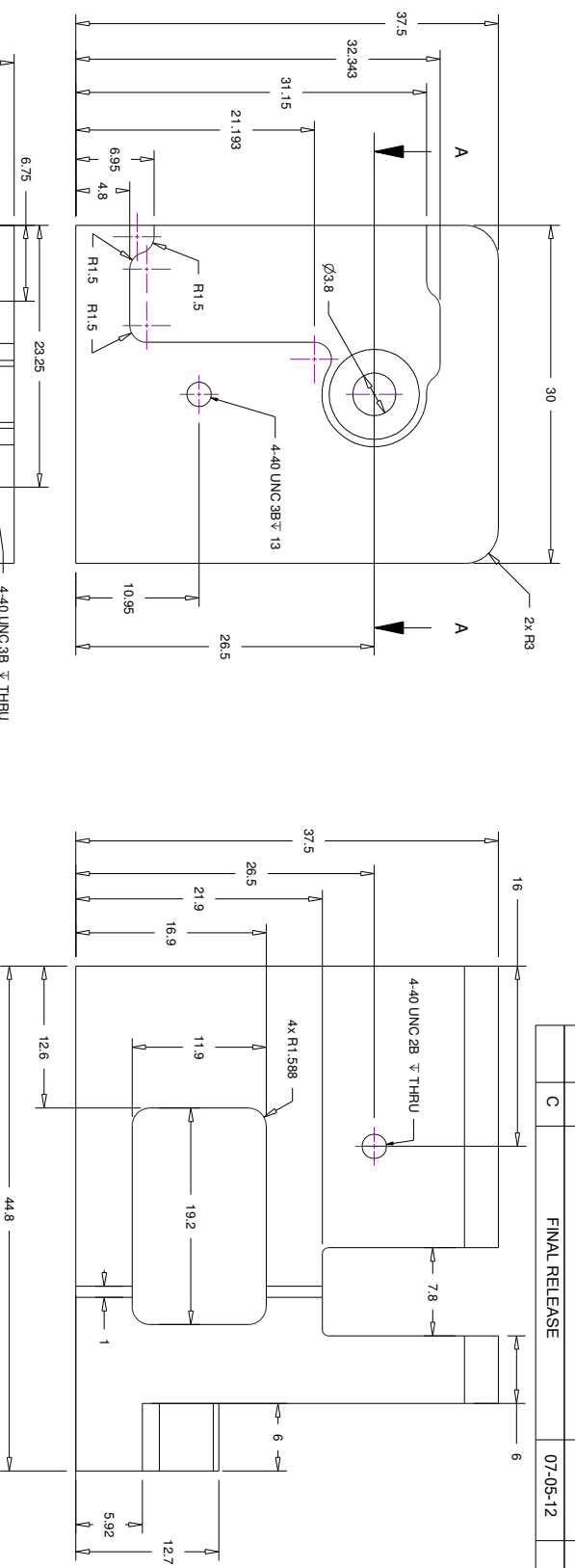
DO NOT SCALE DRAWING

| REVISIONS | | | | |
|-----------|-----|---------------|----------|----------|
| ZONE | REV | DESCRIPTION | DATE | APPROVED |
| C | | FINAL RELEASE | 07-05-12 | |



| | | | |
|--------------------------------------|--|-----------------------------|-----------------|
| MME Dept. | | NAME | Khaled Elbanna |
| WESTERN UNIVERSITY | | STUDENT# | keibanna@uwu.ca |
| TITLE: | | Main Clamp | |
| DIMENSIONS ARE IN MM | | UNLESS OTHERWISE SPECIFIED: | |
| TOLERANCES: | | ANGULAR: ±1° | |
| ONE PLACE DECIMAL: ±0.1 | | TWO PLACE DECIMAL: ±0.01 | |
| FINISH: | | N/A | |
| MATERIAL: Beryllium Cu. H04 (C17510) | | SIZE | DWG. NO. |
| SCALE: 4:1 | | B | 2B |
| SHEET 3 OF 11 | | REV | C |

| REVISIONS | | | DATE | APPROVED |
|-----------|-----|---------------|----------|----------|
| ZONE | REV | DESCRIPTION | | |
| C | | FINAL RELEASE | 07-05-12 | |

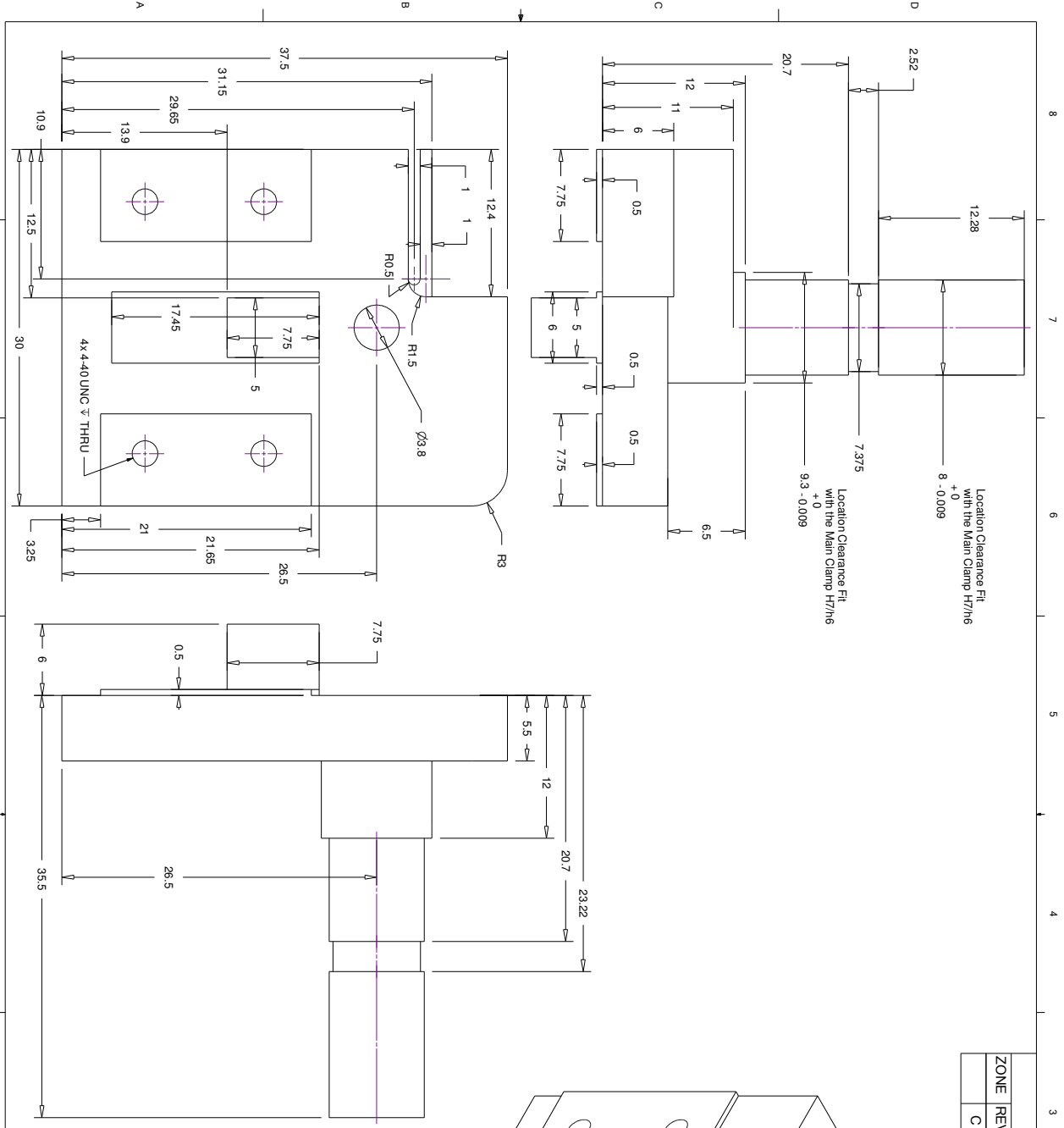
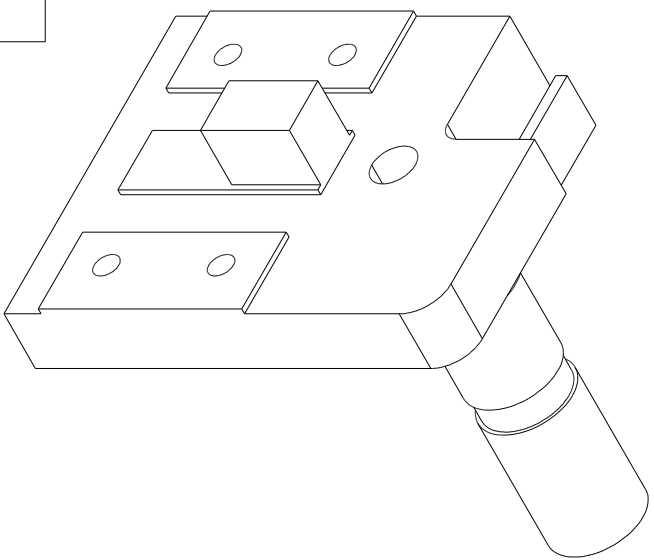


| | | |
|--|--|------------------------------|
| MME Dept. WESTERN UNIVERSITY | | NAME Khaled Elbanna |
| STUDENT# keibanna@uwyo.ca | | TITLE: Main Clamp |
| DIMENSIONS ARE IN MM TOLERANCES: ANGULAR: ±1° ONE PLACE DECIMAL: ±0.1 TWO PLACE DECIMAL: ±0.01 | | SIZE DWG. NO. B 2C |
| UNLESS OTHERWISE SPECIFIED: FINISH Brevillium Cl. H04 (C17510) | | REV C |
| DO NOT SCALE DRAWING | | SCALE: 2.5:1 |

8 7 6 5 4 3 2 1

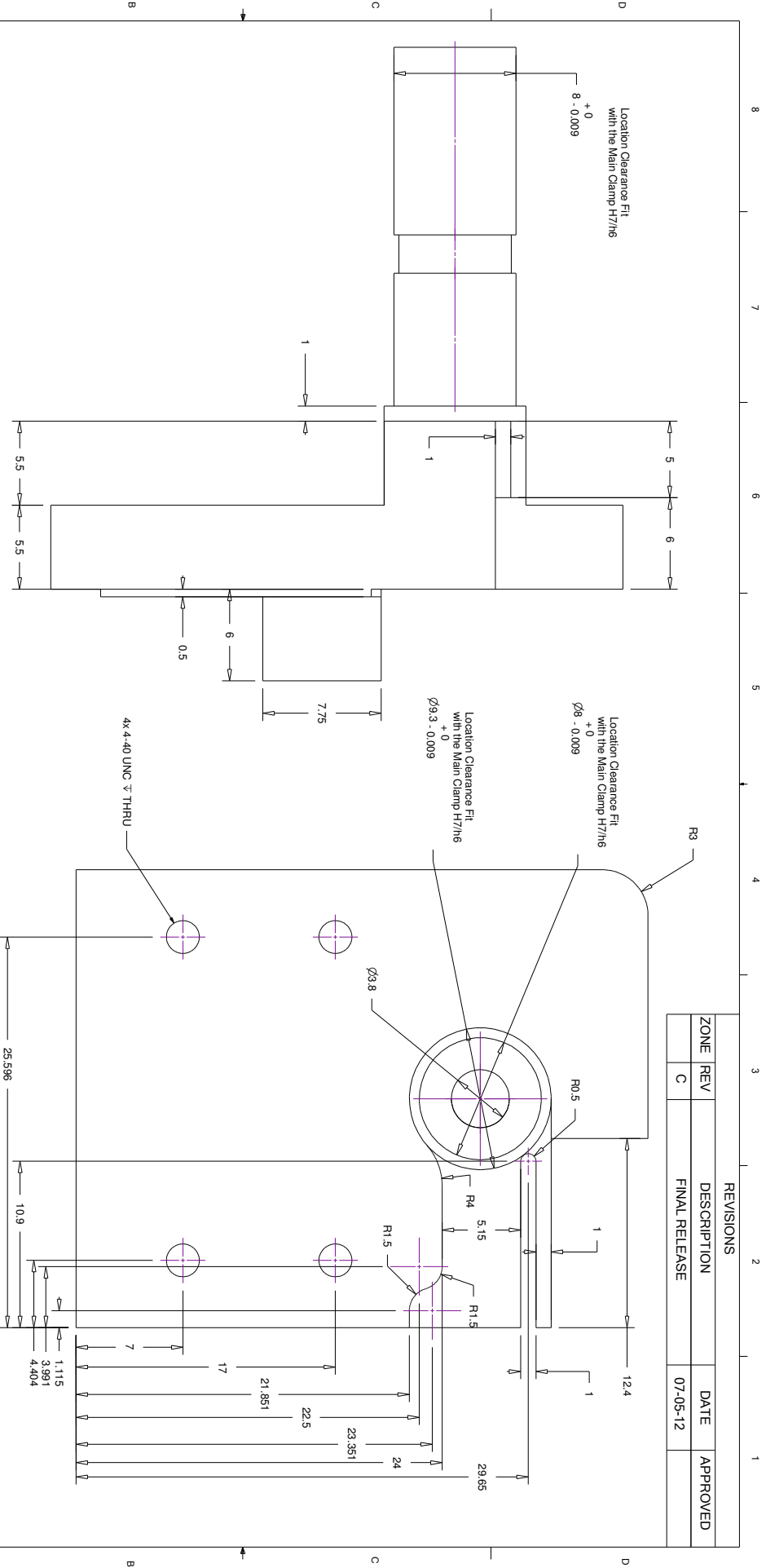
A B C D

| REVISIONS | | | | |
|-----------|-----|---------------|----------|----------|
| ZONE | REV | DESCRIPTION | DATE | APPROVED |
| C | | FINAL RELEASE | 07-05-12 | |



| | |
|--|------------------|
| MME Dept. WESTERN UNIVERSITY | |
| NAME | Khaled Elbanna |
| STUDENT# | keibanna@uwyo.ca |
| TITLE: | |
| Rotary Plate | |
| SIZE | DWG. NO. |
| B | 3A |
| SCALE: 3:1 | REV |
| | C |
| UNLESS OTHERWISE SPECIFIED: DIMENSIONS ARE IN MM TOLERANCES: ANGULAR ± 1° ONE PLACE DECIMAL ± 0.1 TWO PLACE DECIMAL ± 0.01 FINISH Brevillium Cl. H04 (C175 10) N/A | |
| DO NOT SCALE DRAWING | |

| REVISIONS | | | DATE | APPROVED |
|-----------|-----|---------------|----------|----------|
| ZONE | REV | DESCRIPTION | | |
| C | | FINAL RELEASE | 07-05-12 | |

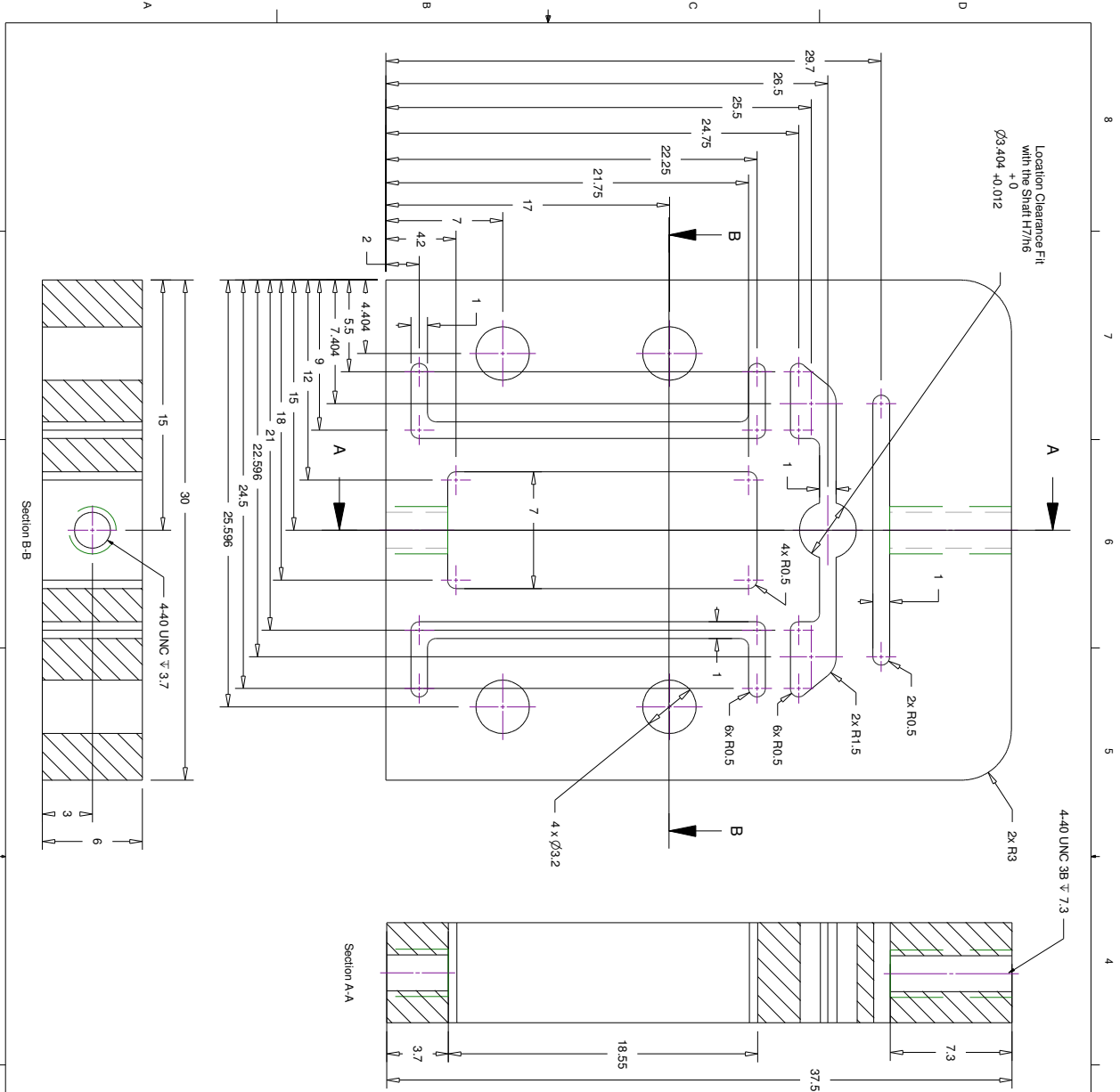
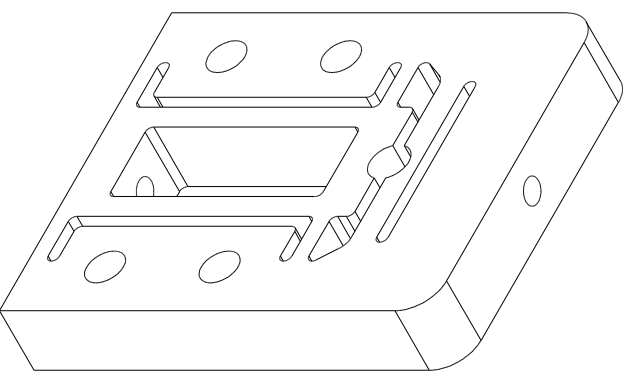


Left View

Back View

| | | | |
|--|--|--|--|
| <p>MME Dept. WESTERN UNIVERSITY</p> | | <p>NAME: Khaled Elbanna STUDENT ID: kelbanna@uwyo.ca</p> | |
| <p>TITLE: Rotary Plate</p> | | <p>UNLESS OTHERWISE SPECIFIED: DIMENSIONS ARE IN MM TOLERANCES: ANGULAR: $\pm 1^\circ$ ONE PLACE DECIMAL: ± 0.1 TWO PLACE DECIMAL: ± 0.01</p> | |
| <p>SIZE: B DWG. NO.: 3B</p> | | <p>FINISH: N/A</p> | |
| <p>SCALE: 4:1</p> | | <p>REV: C</p> | |
| <p>DO NOT SCALE DRAWING</p> | | <p>SHEET 6 OF 11</p> | |

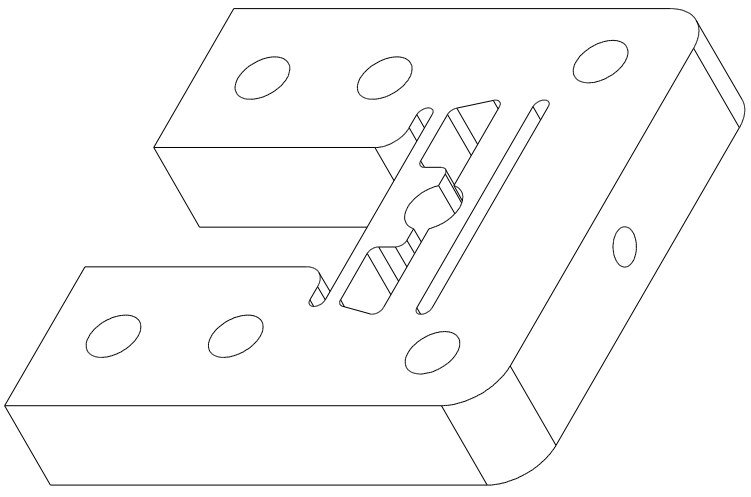
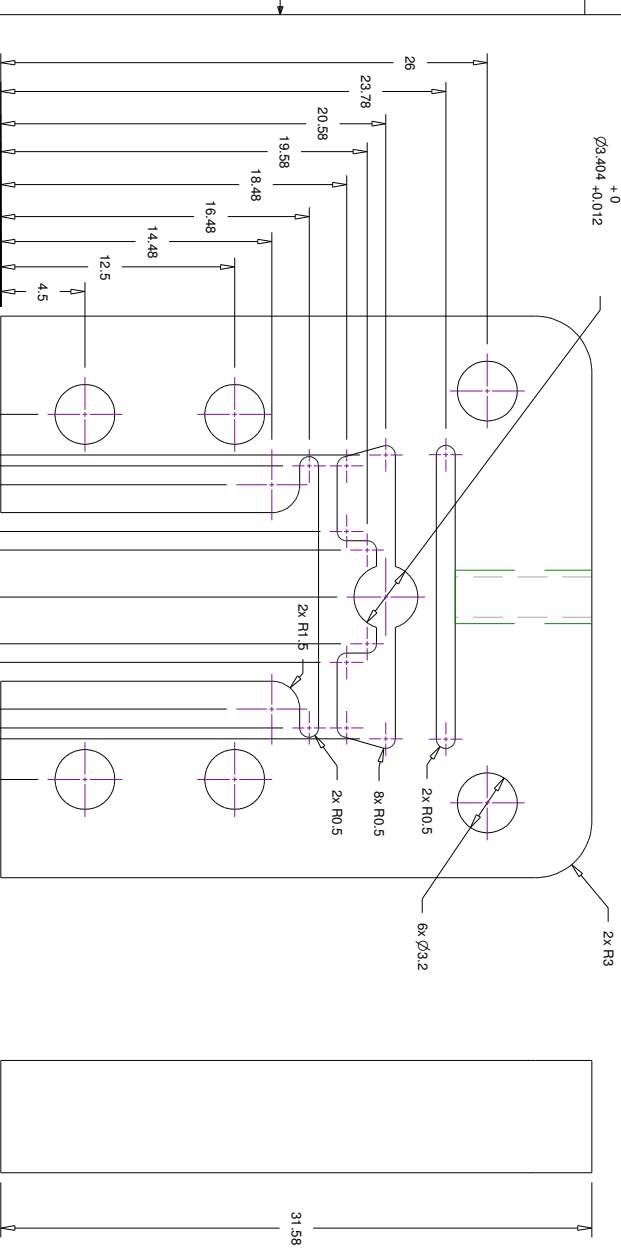
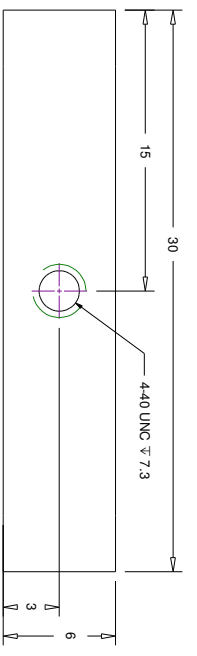
| REVISIONS | | | | |
|-----------|-----|---------------|----------|----------|
| ZONE | REV | DESCRIPTION | DATE | APPROVED |
| C | | FINAL RELEASE | 07-05-12 | |



| | |
|--|------------------|
| MME Dept. WESTERN UNIVERSITY | |
| NAME | Khaled Elbarnan |
| STUDENT# | kelbarna@uwyo.ca |
| TITLE: | |
| Comp. Clamp | |
| SIZE DWG. NO. | B 4 |
| SCALE: 4:1 | |
| REVISION | C |
| SHEET 7 OF 11 | |

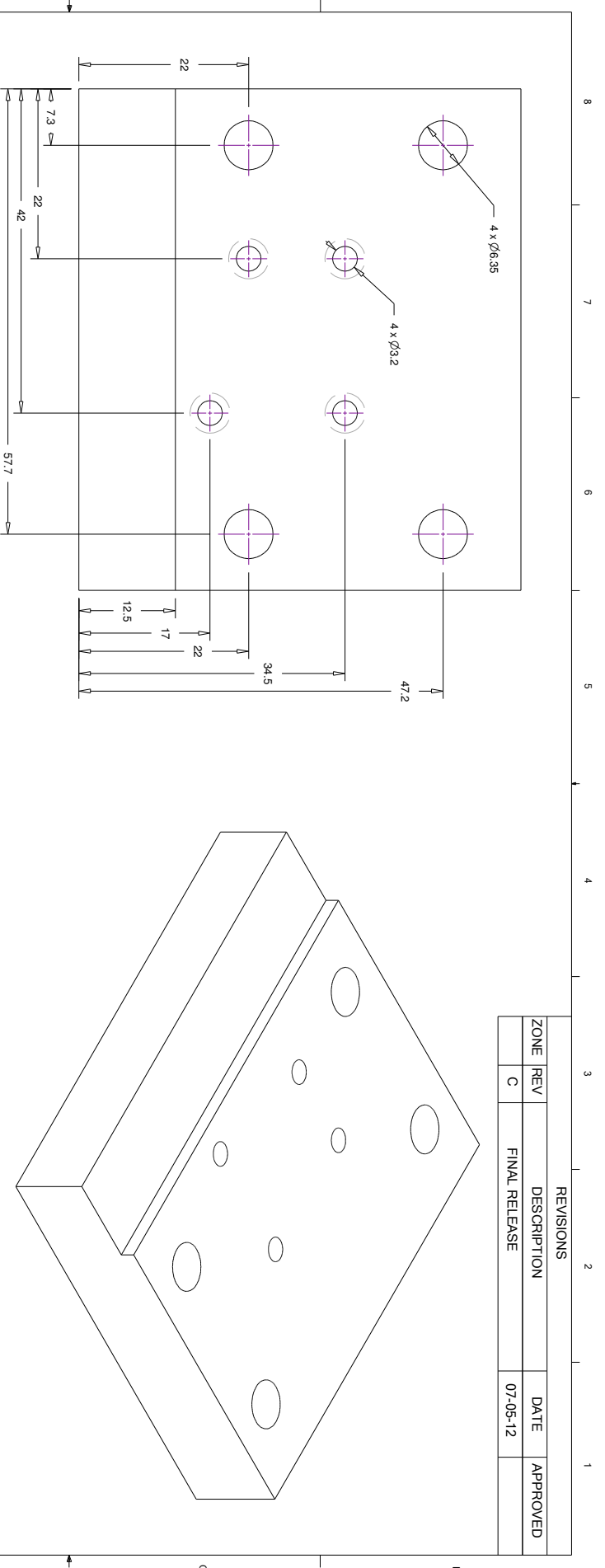
UNLESS OTHERWISE SPECIFIED:
 DIMENSIONS ARE IN MM
 TOLERANCES:
 ANGULAR ± 1°
 ONE PLACE DECIMAL ± 0.1
 TWO PLACE DECIMAL ± 0.01
 FINISH
 MATERIAL: Beryllium Cu, H04 (C17510)
 FINISH: N/A
 DO NOT SCALE DRAWING

| REVISIONS | | | | |
|-----------|-----|---------------|----------|----------|
| ZONE | REV | DESCRIPTION | DATE | APPROVED |
| C | | FINAL RELEASE | 07-05-12 | |



| | | |
|--|--------------------------|--|
| <p>MME Dept. WESTERN UNIVERSITY</p> | | <p>NAME: Khaled Elbanna STUDENT ID: keibanna@uwo.ca</p> |
| <p>TITLE: Clamp</p> | | <p>UNLESS OTHERWISE SPECIFIED: DIMENSIONS ARE IN MM TOLERANCES: ANGULAR: ± 1° ONE PLACE DECIMAL: ± 0.1 TWO PLACE DECIMAL: ± 0.01</p> |
| <p>DATE: 07-05-12</p> | <p>SCALE: 4:1</p> | <p>FINISH: N/A</p> |
| <p>SIZE: B 5</p> | <p>SIZE: B 5</p> | <p>REV: C</p> |
| <p>DO NOT SCALE DRAWING</p> | | <p>SHEET 8 OF 11</p> |

| REVISIONS | | | | |
|-----------|-----|---------------|----------|----------|
| ZONE | REV | DESCRIPTION | DATE | APPROVED |
| C | | FINAL RELEASE | 07-05-12 | |

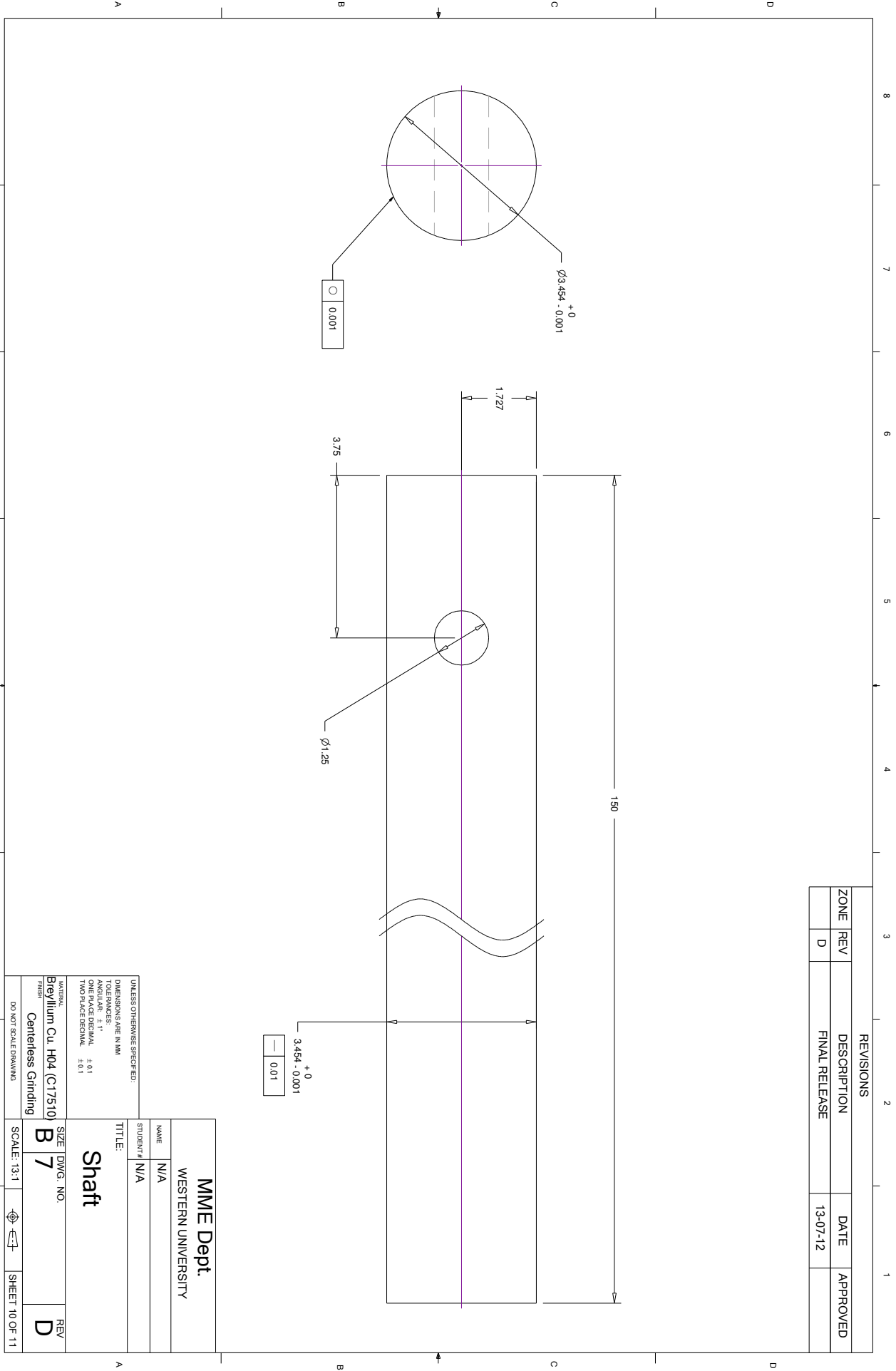


| | | | |
|---------------------------|--|-----------|------------------|
| MME Dept. | | NAME | Khaled Elbanna |
| WESTERN UNIVERSITY | | STUDENT# | kelbanna@uwyo.ca |
| TITLE: | | | |
| Base Plate | | SIZE | DWG. NO. |
| | | B | 6 |
| | | SCALE | 2:1 |
| | | MATERIAL | Derlin |
| | | FINISH | N/A |
| | | REVISIONS | |
| | | C | |

UNLESS OTHERWISE SPECIFIED:
 DIMENSIONS ARE IN MM
 TOLERANCES:
 ANGULAR: $\pm 1^\circ$
 ONE PLACE DECIMAL: ± 0.1
 TWO PLACE DECIMAL: ± 0.01

DO NOT SCALE DRAWING

| REVISIONS | | | | |
|-----------|-----|---------------|----------|----------|
| ZONE | REV | DESCRIPTION | DATE | APPROVED |
| D | | FINAL RELEASE | 13-07-12 | |



| | | | |
|---------------------------------|------------------------------|-------|-----|
| MME Dept. WESTERN UNIVERSITY | | NAME | N/A |
| STUDENT # | | N/A | |
| TITLE: | | Shaft | |
| UNLESS OTHERWISE SPECIFIED: | DIMENSIONS ARE IN MM | | |
| TOLERANCES: | ANGULAR: $\pm 1^\circ$ | | |
| ONE PLACE DECIMAL: | ± 0.1 | | |
| TWO PLACE DECIMAL: | ± 0.01 | | |
| FINISH | Breyvillium Cl. H04 (C17510) | | |
| Centerless Grinding | SCALE: 13:1 | | |
| DO NOT SCALE DRAWING | SIZE | TWGS | NO. |
| | B | 7 | |
| | REV | D | |

WESTERN
UNIVERSITY
MME Dept.
WESTERN UNIVERSITY

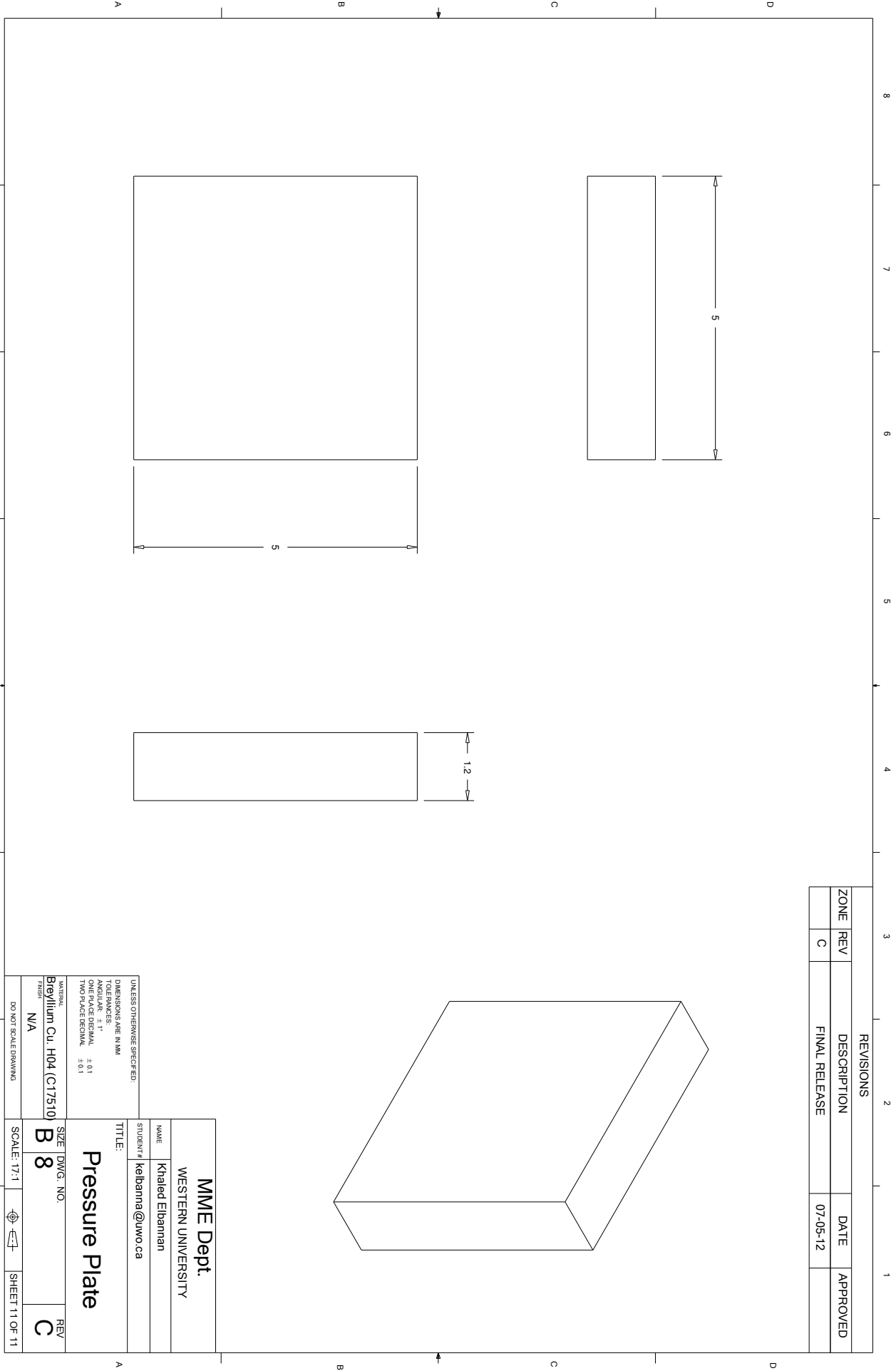
NAME: N/A
STUDENT #: N/A
TITLE: Shaft
UNLESS OTHERWISE SPECIFIED:
DIMENSIONS ARE IN MM
TOLERANCES:
ANGULAR: $\pm 1^\circ$
ONE PLACE DECIMAL: ± 0.1
TWO PLACE DECIMAL: ± 0.01
FINISH: Breyvillium Cl. H04 (C17510)

Centerless Grinding
SCALE: 13:1
DO NOT SCALE DRAWING

SIZE TWGS NO.
B 7

REV D

| REVISIONS | | | | |
|-----------|-----|---------------|----------|----------|
| ZONE | REV | DESCRIPTION | DATE | APPROVED |
| C | | FINAL RELEASE | 07-05-12 | |



| | |
|-----------------------|------------------|
| MME Dept. | |
| WESTERN UNIVERSITY | |
| NAME | Khaled Elbanna |
| STUDENT# | kelbanna@uwyo.ca |
| TITLE: | |
| Pressure Plate | |
| SIZE | TDWG. NO. |
| B | 8 |
| SCALE: 1:1 | REV |
| | C |
| SHEET 11 OF 11 | |

UNLESS OTHERWISE SPECIFIED:
 DIMENSIONS ARE IN MM
 TOLERANCES:
 ANGULAR ± 1°
 ONE PLACE DECIMAL ± 0.1
 TWO PLACE DECIMAL ± 0.01
 FINISH: N/A
 MATERIAL: Brevillum Cu, H04 (C17510)
 DO NOT SCALE DRAWING

VITA

| | |
|---|---|
| Name | Khaled Mohamed El Bannan |
| Post-secondary Education and Degrees | <p>Ain Shams University Cairo, Egypt 1985-1991 B.Sc. in Mechanical Engineering</p> <p>University of Waterloo Waterloo, Ontario, Canada 2003-2005 M. Eng. In Mechanical Engineering</p> |
| Honors and Awards | <p>Western Graduate Research Scholarships (WGRS) University of Western Ontario 2007-2012</p> <p>Ontario Graduate Scholarship in Science and Technology (OGSST) University of Western Ontario 2009 -2010</p> |
| Related Work Experience | <p>Teaching Assistant University of Western Ontario 2008-2012</p> |

Publications:

- [1] K. El Bannan, S. Salisbury, "Compact Piezoworm Actuator for MR Guided Surgical Needle Procedures", Proceedings of Smart Materials & Structures, CANSMART 2009, Montreal, Quebec, Canada, P. 237-246.
- [2] W. Handler, K. El Bannan, C. Wyenberg, B. Chronik and Shaun P. Salisbury, "Choosing materials for MR applications: A study of various metals", Proceedings of the Nineteenth Scientific Meeting and Exhibition for the International Society for Magnetic Resonance in Medicine: p 3904 (2011).
- [3] K. El Bannan, W. Handler, C. Wyenberg, B. Chronik and Shaun P. Salisbury, "Prediction of Force and Image Artifacts under MRI for Metals used in Medical Devices", IEEE/ASME Transactions on Mechatronics, 2012, accepted.

- [4] K. El Bannan, S. Salisbury, "Design of a Two Degree-of-Freedom, MRI-Compatible Actuator", 34th Annual International Conference of the Engineering in Medicine and Biology, EMBC'12 is "Engineering Innovation in Global Health", 2012, accepted.
- [5] K. El Bannan, W. Handler, B. Chronik, and Shaun P. Salisbury, "Prediction of Heating of Metallic Cylinders Induced by Switching in the Gradient Field Range", Journal of Magnetic Resonance (JMR), 2012, accepted.